MECHANICAL EVALUATION OF STRUCTURE AND FUNCTION IN FIBROUS SOFT TISSUE USING MR ELASTOGRAPHY

by

Daniel R. Smith

A dissertation submitted to the Faculty of the University of Delaware in partial fulfillment of the requirements for the degree of Doctor of Philosophy in Biomedical Engineering

Spring 2022

MECHANICAL EVALUATION OF STRUCTURE AND FUNCTION

IN FIBROUS SOFT TISSUE USING MR ELASTOGRAPHY

by

Daniel R. Smith

Approved: _____
Kristi Kiick, Ph.D.
Chair of the Department of Biomedical Engineering

Approved: _____
Levi Thompson, Ph.D.
Dean of the College of Engineering

Approved: _____
Louis F. Rossi, Ph.D.
Vice Provost for Graduate and Professional Education and
Dean of the Graduate College

I certify that I have read this dissertation and that in my opinion it meets the academic and professional standard required by the University as a dissertation for the degree of Doctor of Philosophy.

Signed: _____

Curtis Johnson, Ph.D.
Professor in charge of dissertation

I certify that I have read this dissertation and that in my opinion it meets the academic and professional standard required by the University as a dissertation for the degree of Doctor of Philosophy.

Signed: _____

Thomas Buchanan, Ph.D.
Member of dissertation committee

I certify that I have read this dissertation and that in my opinion it meets the academic and professional standard required by the University as a dissertation for the degree of Doctor of Philosophy.

Signed: _____

Fabrizio Sergi, Ph.D.
Member of dissertation committee

I certify that I have read this dissertation and that in my opinion it meets the academic and professional standard required by the University as a dissertation for the degree of Doctor of Philosophy.

Signed: _____

Jeremy Crenshaw, Ph.D.
Member of dissertation committee

ACKNOWLEDGMENTS

First and foremost, I would like to thank Dr. Curtis Johnson, my advisor, mentor and friend, for all of your guidance and support over the six years since we first met. Thank you for entrusting me with helping to start you lab and sharing your love for research and helping me truly find my own. Your support, advice, and friendship helped carry me through many of the stumbles and frustrations over the years. I would also like to thank my committee members, Dr. Jeremy Crenshaw, Dr. Fabrizio Sergi, and Dr. Thomas Buchanan, for their support and advice over the years. I would also like to thank Dr. Buchanan for his guidance and encouragement throughout my engineering journey.

Additionally, I would like to thank the many members of the Mechanical Neuroimaging Lab, both past and present, who helped me with experiments and made life in and out of the lab much more enjoyable: Dr. Lucy Hiscox, Grace McIlvain, Peyton Delgorio, Diego Caban-Rivera, Tyler Williams, Dr. Melissa DiFabio, Alexis Merritt, Charlotte Chaze, Alexa Diano, Mary Kramer, Kyra Twohy, and Olivia Bailey. I am thankful for all of your friendships and advice over the years, and I would not have become the researcher and scientist I am without you. Thank you especially to Grace and Peyton for being there throughout this journey with advice or a laugh and to Tyler and Diego for helping with all the crazy experiments and being incredible friends and roommates.

I would also like to acknowledge the contributions of those at the Center of Biomedical and Brain Imaging who helped with my MRI technical training and

making sure my experiments ran smoothly, particularly Dr. Keith Schneider, Trevor Wigal, and Ibrahim Malik.

Also, thank you to all of my BME friends who made this process so much more enjoyable and fun over the years. Thank you to Haider Chisty, Rebecca Nikonowicz, and Danielle Valcourt for bringing laughs and smiles during the good times and support and solace during the low ones. Thank you to Kyle Meadows for being one of my closest friends over the past four years, who I could count on to be there through it all.

Next, I would like to thank the Mech-E crew, both from undergrad and onward: Alex Morren, Alison Rainis, Chris Faircloth, Danielle Wagner, Kristen Danek, Garrett Davey, Matt Elizardo, Mattie Hubner, Mark Romanelli, Mike Carr, Mike Carroll, Mike Townsend, Thien-nam Dinh, and Zoe Coffing Faircloth. You all mean the world to me and I am blessed to have incredible friends around me, encouraging and inspiring me. To Joe Rainis, and Vinu Rajendran, thank you for your friendship and constant motivation over these past fifteen years, as I would not be the person I am today without you both.

Thank you to the Ocean City families, to the Lucys, the Lukens, and particularly the Byrnes: Tom, Lynn, Katie, Ryan, and Julie. Thank you for all of the friendship, love, and encouragement over the years. I would also like to thank the Brennans, Marty, Wendy, Mike, Sarah, and Emily, for being like a second family to me over all these years.

Most importantly, thank you to my family, without whom I would not be where I am or be who I am now. To my extended family, the Smiths, the Montejos, the Staffords, and the McThenias, thank you for creating such a warm and nurturing

environment for me to grow up in. To Dez, thank you for becoming an older sister to me and for your constant encouragement and advice. To Kyle, thank you for being one of my best role models and my best friend. I could never asked for a better older brother to look up to. To Meg, thank you for being my heart and greatest source of inspiration. Your love constantly pushes me to be the best version of myself. To Tim and Deirdre, my amazing parents, who I can never thank enough for their unending love and support and without whom this would never have been possible. I am incredibly lucky to have you.

Lastly, I would like to acknowledge my funding sources for this work, including the Office of Naval Research (N-00014-17-P-7001, N00014-18-P-7004, and N00014-18-1-2018), the Delaware INBRE Program through NIH/NIGMS (P20-GM103446), NIH/NIBIB (R01-EB027577), NIH/NIA (R01-AG058853), and NSF (CBET- 1911683).

DEDICATION

To my grandparents, Marion, George, Jean, and Henry, your love continues to be felt

TABLE OF CONTENTS

LIST OF TABLES xi
LIST OF FIGURES xii
ABSTRACT xvii

Chapter

1 INTRODUCTION 1

1.1 White Matter: Structure and Pathology 2
1.2 Skeletal Muscle: Structure, Function, and Pathology 6
1.3 Thesis Overview 12

2 TECHNIQUES FOR *IN-VIVO* EVALUATION OF FUNCTION AND STRUCTURE IN FIBROUS SOFT TISSUE 14

2.1 Overview 14
2.2 Electrical Stimulation Techniques 14
2.3 Ultrasound Imaging 17

2.3.1 Ultrasound Elastography 18

2.4 Magnetic Resonance Imaging 20

2.4.1 MRI Physics 20
2.4.2 Diffusion MRI 22
2.4.3 MR Elastography 24

3 MULTI-EXCITATION MR ELASTOGRAPHY OF THE BRAIN: WAVE PROPAGATION IN ANISOTROPIC WHITE MATTER 34

3.1 Introduction 34
3.2 Methods 36

3.2.1 Slow and Fast Wave Propagation in ITI Materials 36
3.2.2 Data Acquisition 38
3.2.3 Individual Wave Identification 39
3.2.4 Anisotropic Parameter Estimation 41

3.2.5 Analysis 43

3.3 Results 45

3.3.1 Shear Wave Differentiation 45
3.3.2 Slow and Fast Shear Wave Identification 47
3.3.3 Least Squares Parameter Estimation 49

3.4 Discussion 50
3.5 Conclusions 53

4 ANISOTROPIC ESTIMATION OF WHITE MATTER USING MULTIEXCITATION MR ELASTOGRAPHY AND A TRANSVERSELY ISOTROPIC NONLINEAR INVERSION ALGORITHM 55

4.1 Introduction 55
4.2 Methods 58

4.2.1 Data Acquisition 58
4.2.2 Transversely Isotropic Nonlinear Inversion 60
4.2.3 Analysis 63

4.3 Results 64

4.3.1 Anisotropic Mechanical Properties of White Matter Tracts 64
4.3.2 Measurement Repeatability 68
4.3.3 Tract Heterogeneity 70

4.4 Discussion 71
4.5 Conclusions 77

5 MULTI-MUSCLE MR ELASTOGRAPHY IN THE HUMAN FOREARM . 78

5.1 Introduction 78
5.2 Methods 81

5.2.1 Experimental Design 81
5.2.2 Data Analysis and Statistics 83

5.3 Results 86

5.3.1 Muscle Recruitment: Agonist vs. Antagonist Action 87
5.3.2 Muscle Group Analysis 88
5.3.3 Wrist Angle Analysis 89

5.3.4 Individual Muscle Analysis 90

5.4 Discussion 91
5.5 Limitations 94
5.6 Conclusions 95

6 IN-VIVO ESTIMATION OF ANISOTROPIC MECHANICAL PROPERTIES OF THE GASTROCNEMIUS DURING TENSION-BASED LOADING 97

6.1 Introduction 97
6.2 Methods 100

6.2.1 Experimental Setup 100
6.2.2 Imaging Protocol 101
6.2.3 Data Processing 103

6.3 Results 104

6.3.1 Experiment 1 – Passive Lengthening 104
6.3.2 Experiment 2 – Active Muscle Contraction 106

6.4 Discussion 107
6.5 Conclusions 112

7 CONCLUSIONS AND FUTURE DIRECTIONS 113

7.1 Conclusions 113
7.2 Future Directions of Work 115
7.3 Summary 118

REFERENCES 119

Appendix

A IRB/HUMAN SUBJECTS APPROVAL 147
B PERMISSIONS 151

LIST OF TABLES

Table 4.1: A comparison showing the mean and standard deviation of the three anisotropic parameters, μ, ϕ, and ζ, for each the seven ROIs across the entire population sample. 67

Table 4.2: This comparison shows the standard deviations of the three anisotropic parameters, μ, φ, and ζ, between the population and repeated subject data sets. 69

Table 5.1: ANOVA marginal analyses performed on the shear wave speed squared measurements collected for contraction states 86

Table 6.1: The average and standard deviations of each of the four parameters at the three different knee angles measured during Experiment 1. 105

Table 6.2: The average and standard deviations of each of the four parameters at the three different active contraction states measured during Experiment 2. 107

LIST OF FIGURES

Figure 1.1: Axons (blue) are supported by various structures, such as myelin (green sheath), oligodendrocytes (green spindle), and astrocytes (light blue). These structures serve multiple functions including protecting and stabilizing the axon as it transmits signals between axons within the brain. *Adapted from Stassart, et al. 2018* [19] 3

Figure 1.2: (A) Skeletal muscle consists of a hierarchal structure of fibers and other supportive structures. The fibers are made of (B) sarcomeres which consist of three primary protein based myofilaments, actin, myosin, and titin. *Adapted from Sciorati, et al. 2016 and Tharp, et al. 2020* [50,51]. 8

Figure 1.3: The force output from muscles is a component of (A) relative sarcomere length and (B) combined tension level for the overall muscle. *Adapted from Brughelli, et al. 2007* [59] 10

Figure 2.1 A diagram of the generalized setup and readout of electromyography. *Repurposed from Polasek, et al. 2009* [95] 16

Figure 2.2: [*Left*] The experimental method of shear wave elastography (SWE) using two actuators to acquire [*Right*] displacement images. *Adapted from Tsuchida, et al 2020 and Nakayama, et al. 2021.* [128,129] 19

Figure 2.3: Standard MRI structural scans of the brain include (A) T1-weighted anatomical scans and (B) diffusion tensor imaging (DTI) scans, which indicates general fiber direction of white matter by colorization. *Adapted from Assaf, et al. 2008* [153] 24

Figure 2.4: Shear waves are generated using actuators and shown here in a single slice of a brain, generated using a pneumatic actuator at 50 Hz vibration frequency. 25

Figure 2.5: The iterative process of NLI consists of three primary parts: the parameter estimate, creation of the FEA model utilizing subzones, and comparison to original data using the iterative objective function. *Adapted from McGarry, et al. 2012* [163] 29

Figure 3.1: Overview of multi-excitation MRE. **(A)** Positioning of pillow driver for AP excitation and paddle driver for LR excitation. **(B)** Representative wave fields from AP and LR excitations, shown as their x, y, and z components. 39

Figure 3.2: The approach used to determine voxelwise stiffness estimates from individual wave fields. **(A)** Directional filters, based on the primary and secondary directions of a specific voxel, are applied to the wave field over the entire brain, providing two (primary and secondary) filtered fields. **(B)** Slow and fast shear waves in those primary and secondary directions. **(C)** Isolated section, outlined by the white box, of the stiffness map estimated for each of the slow and fast waves, at every voxel, and the stiffness map created by compiling results from individual inversions. 43

Figure 3.3: Illustration of individual wave propagation directions. **(A)** Primary ($N1$) and secondary ($N2$) wave propagation directions for both AP and LR excitations within a single voxel. Note the spheres have different orientations between the two excitations. **(B)** Average wave direction throughout the brain along with primary and secondary wave directions for both AP and LR excitations. **(C)** Amplitudes of the primary and secondary waves and the ratio of the two for both AP and LR excitations. 45

Figure 3.4: Overview of displacement data sufficient for anisotropic inversion in white matter. **(A)** Number of slow and fast waves in each voxel for single excitations (AP or LR) and multiple excitations (AP+LR), and **(B)** white matter voxels with data meeting the minimum inversion criteria from both excitations. **(C)** Percentage of voxels across white matter and in the corpus callosum body, an individual white matter tract, that fit the criteria for each excitation. 47

Figure 3.5: Distribution of anisotropic parameters **(A)** substrate shear modulus, μ, **(B)** shear anisotropy, ϕ, and **(C)** tensile anisotropy, ζ, in the corpus callosum body for each subject and all subjects pooled together. **(D)** Relationship between ϕ and ζ in each voxel across all subjects (r = 0.38). 49

Figure 4.1: Schematic of the multi-excitation actuator design including pillow driver for anterior-posterior excitation and custom 3D printed left-right actuator, as well as a picture of the drivers inside the 20 channel head coil. The design allows the actuator to rest against the side of the subject's head and is adjustable for different head sizes. 59

Figure 4.2: The data from MRE (AP and LR wave motion) and DTI (V1) are input into the transversely isotropic, non-linear inversion algorithm (TI-NLI) to solve for the three anisotropic parameters: substrate shear modulus, μ, shear anisotropy, ϕ, and tensile anisotropy, ζ..... 63

Figure 4.3 Maps of the estimated anisotropic parameters in the human brain in a representative slice for each of the ROIs used in this study: gray matter, white matter, corpus callosum, corona radiata, superior longitudinal fasciculus, forceps minor, and forceps major. 65

Figure 4.4: (A-C) Average parameter outcomes in healthy young adults for each ROI; (D-F) representative axial, sagittal, and coronal slices of each property; (G-I) differences between individual tracts properties with significant differences denoted by * ($p < 0.05$)..... 66

Figure 4.5: (A-C) The average parameter outcomes for the single subject data set were estimated within each of the generated ROIs and presented in box plots to analyze repeatability of the data. (D-F) The variability measures (COV or standard deviation) of the single subject data set are plotted against those of the mulit-subject data set, with the single subject data set denoted by the darker color..... 68

Figure 4.6: Comparison of the anisotropic parameter estimates in the subregions of the corpus callosum: the genu, body, and splenium. Significant differences in properties between regions denoted by * ($p < 0.05$). 70

Figure 5.1: (A) Subjects are positioned head first and prone with their right arm placed in the custom MRE actuator, (C) connected to an active driver, and perform isometric contractions as cued by (B) the visual feedback system that allows the subject to visualize and maintain applied torque..... 82

Figure 5.2: The custom actuator is used to generate (A) the shear wave motion that is then used by the non-linear inversion algorithm (NLI) to creates (B) maps of shear wave speed squared..... 83

Figure 5.3: Each muscle of the thirteen muscles that are involved in wrist motion and analyzed in this study are manually segmented. A representative cross section with an region of interest defining each of the muscles is shown in the figure..... 85

Figure 5.4: (Left) This figure shows the normalized shear wave speed squared values for all muscles during their agonist and antagonist states. Averages are denoted by data set with the black lines while individual muscles use gray lines. (Right) We show the statistically significant relationships between the various activation states for the agonists and antagonists with Statistical significance is denoted by a *..... 87

Figure 5.5: This figure shows the normalized shear wave speed squared values for the extensor (left) and flexor (right) muscles during each of the contraction states. Averages are denoted by data set with the black lines while individual muscles use gray lines. Statistical significance is denoted by a *..... 88

Figure 5.6: This figure shows the average normalized shear wave speed squared for the flexors (Top) and extensor (Bottom) muscles at separated by wrist position. The average of each muscle group is shown in colored diamonds and black lines, while the individual muscle averages are in light gray..... 89

Figure 5.7: This figure is a chart depicting the Cohen's D effect size for statistical differences comparing each activation to the rest condition for each of the individual flexor and extensor muscles. Activations shown in gray were non-significant, while those shown in varying levels of green were found to show significance. 90

Figure 6.1: (A) Experiment 1 entails placing the subject's foot in a custom ankle brace to maintain a constant ankle angle while the angle of subject's knee is altered through raising or lowering the leg support. (B) Experiment 2 replaces the ankle brace with a peddle-like device which induces isometric contraction when the subject pushes against one of the two springs during plantar- or dorsiflexion, while their leg is supported at a constant knee angle. 101

Figure 6.2: Two primary muscles, **(A)** medial and lateral heads of the gastrocnemius, were investigated to determine the anisotropic material parameters. There material parameters were solved for by combining **(B)** MRE displacement fields and **(C)** fiber directions from DTI. **(D)** The anisotropic parameters solved for include substrate shear stiffness (μ), shear anisotropy (ϕ), and tensile anisotropy (ζ). 102

Figure 6.3: Results of Experiment 1, comparing the effects of increasing muscle length with knee angle on the NITI anisotropic parameters, from left to right, fiber shear stiffness, substrate shear stiffness, shear anisotropy, and tensile anisotropy. 104

Figure 6.4: This figure shows the results of Experiment 2, comparing the effects of isometric contraction on (from left to right), fiber shear stiffness, substrate shear stiffness, shear anisotropy, and tensile anisotropy. Statistically significant differences in the data set are denoted by a *. . 106

Figure 7.1: The future avenues of this anisotropic MRE research fall under one of three categories: investigation of brain or muscle tissue, or further development of the multiexcitation MRE method, each with their own set of further applications. 116

ABSTRACT

Human soft tissues are highly complex networks comprised of a variety of components that contribute to the overall functionality of the tissue, but these structures can be disrupted through injury or pathology, leading to tissue dysfunction. Magnetic resonance elastography (MRE) is a developing imaging technique that has shown promise in evaluating human soft tissues in-vivo by providing mechanical property estimates that are sensitive to structural changes in these tissues, including sensitivity to pathological changes. While MRE has proved to be an effective technique in much of human soft tissue, fibrous soft tissues, such as brain white matter and skeletal muscle, cause standard assumptions of mechanical isotropy to fail, resulting in data-model mismatches and inaccurate evaluations of tissue integrity and health. In this thesis, we propose to develop and test an MRE method to evaluate the health of fibrous soft tissues by evaluating structural and functional changes from pathology or injury.

The first part of work focuses on the assessing the viability of using a nearly incompressible, transversely isotropic (NITI) material model to accurately estimate the anisotropic material properties of human white matter. This NITI material model uses three independent material parameters to describe tissue response, but the definition of

these parameters with MRE requires more information than is typically generated. To generate the necessary data, we utilize a technique called multi-excitation MRE, which uses multiple actuators to generate unique complex waveforms throughout the brain. Through analysis of these waveforms, we show that multiexcitation MRE provides sufficient information to estimate the NITI independent material parameters throughout white matter, ensuring repeatable and reliable parameters measures. Additionally, we estimate these parameters using the recently developed transversely isotropic, nonlinear inversion algorithm (TI-NLI) and combine multiexcitation MRE wave motion data and white matter fiber directions, as defined by diffusion tensor imaging (DTI) data. Using a population of healthy young subjects, we assess the parameter's sensitivity to structural variances in white matter by quantifying the anisotropic parameters within individual white matter tracts across the population as well as the heterogeneity within a single tract. By capturing this heterogeneity across WM, this technique indicates an ability to capture structural variances caused by other sources, including degradation from injury or pathology or recovery through applied therapies.

Although structural variations provide can provide significant information about soft tissue health, skeletal muscle has primarily been evaluated through functional measures of health, such as tissue loading. In the second half of this work, we aim to evaluate MRE's capacity to measure functional outcomes like loading by capturing in-vivo estimates of skeletal muscle tension response and force production. Using multi-muscle MRE (MM-MRE), we provide in-vivo measurements of

functional changes through three primary factors: correlation between combined muscle load and shear stiffness parameter outcomes; significant shear stiffness differences between muscles during agonist and antagonist actions; and variation of shear stiffness outcomes with different levels of initial loading due to muscle length. We then applied TI-NLI to skeletal muscle to quantify the anisotropic variations during passive muscle lengthening and isometric contractions and found unique parameter responses between the two conditions. These unique responses indicate anisotropic MRE's capacity to provide a multifaceted approach to analyzing response to functional measures and provide a valuable tool for evaluating further changes in response due to injury-based or pathological changes to skeletal muscle.

Chapter 1

INTRODUCTION

Human soft tissues are highly complex networks comprised of a variety of components that contribute the overall functionality of the tissue [1–4]. In fact, the body's regulation and maintenance of these components and their proper arrangement within the tissue plays a vital role in their continued healthy function. Injury or pathology leading to tissue impairment or degradation causes disruption to the overall makeup of the tissue, and therefore begins impacting tissue function, leading to either rapid onset or slowly emerging symptoms. As such, evaluation of tissue structure and function provides a means for characterization of tissue health and dysfunction. In-vivo imaging provides the opportunity to observe and compare healthy tissue to pathologically affected tissue within living subjects, thereby limiting the effects of outside influences. Additionally, imaging methods can produce repeated measures of the same tissue over time, allowing for monitoring and characterization of subjects during pathology progression or tissue recovery from injury.

Magnetic resonance elastography (MRE) is an imaging technique that has shown promise in providing mechanical property estimates of human soft tissue that are sensitive to structural changes in these tissues, including sensitivity to pathological changes. MRE is a phase contrast magnetic resonance imaging (MRI) technique that uses harmonic shear wave propagation to estimate the viscoelastic mechanical properties of soft tissues [5–7]. Recent studies in the field have shown MRE's ability to quantify these pathological changes in multiple human tissues, including liver [8,9],

brain [10,11], heart [12], and skeletal muscle [13,14]. Most MRE studies have worked under the material assumption of mechanical isotropy within the tissue of interest, which is an assumption that holds fairly well in most human soft tissues [15,16]. However, mechanical evaluation of fibrous tissues, such as brain white matter (WM) and skeletal muscle, requires a parameter estimation method that utilizes an anisotropic material model for accurate tissue assessment. Using an anisotropic material model provides additional parameters by which to define the tissue, capturing the increased mechanical complexity of a fibrous soft tissue. Therefore, by utilizing MRE to quantify the anisotropic material parameters of fibrous soft tissues, we can evaluate the structural health of these tissues and characterize tissue degradation and recovery.

1.1 White Matter: Structure and Pathology

White matter structure is primarily formed by axons, which are long fibrous projections of neuronal cells, and other supportive tissues including myelin and oligodendrocytes. These axons transmit signals to along their lengths to synapses on other neuronal cells with the signals travelling through action potential, an electrochemical pulse caused by voltage gradients. While axons serve as the primary structure in WM, they are supported by multiple other structures that help ensure proper function of the tissue. Though injury and degradation of axons does occur, most pathologies affect the supportive structures, and through doing so, affect the functionality of axons and WM as a whole.

The primary support structure of axons in WM is myelin, a lipid and protein based structure that forms protective sheaths around the axon [17–20]. In addition to protecting axons, the myelin sheath increases the transmission rates of the action

potential along the axon through insulation, causing the electrochemical pulse to jump between short gaps between the myelin sheaths, called nodes of Ranvier. In WM, these myelin sheaths are the creation of oligodendrocytes wrapping one of their multiple processes around an axon [21,22]. A single oligodendrocyte can insulate up to 50 axons, thereby binding these multiple axons together and creating an inter-axonal support structure. In the case of demyelination through axonal injury or other pathological cell death, oligodendrocyte progenitor cells create new oligodendrocytes, and are therefore responsible for myelin regeneration. Though the myelin regenerates, the actual functionality of the myelin sheaths is significantly diminished.

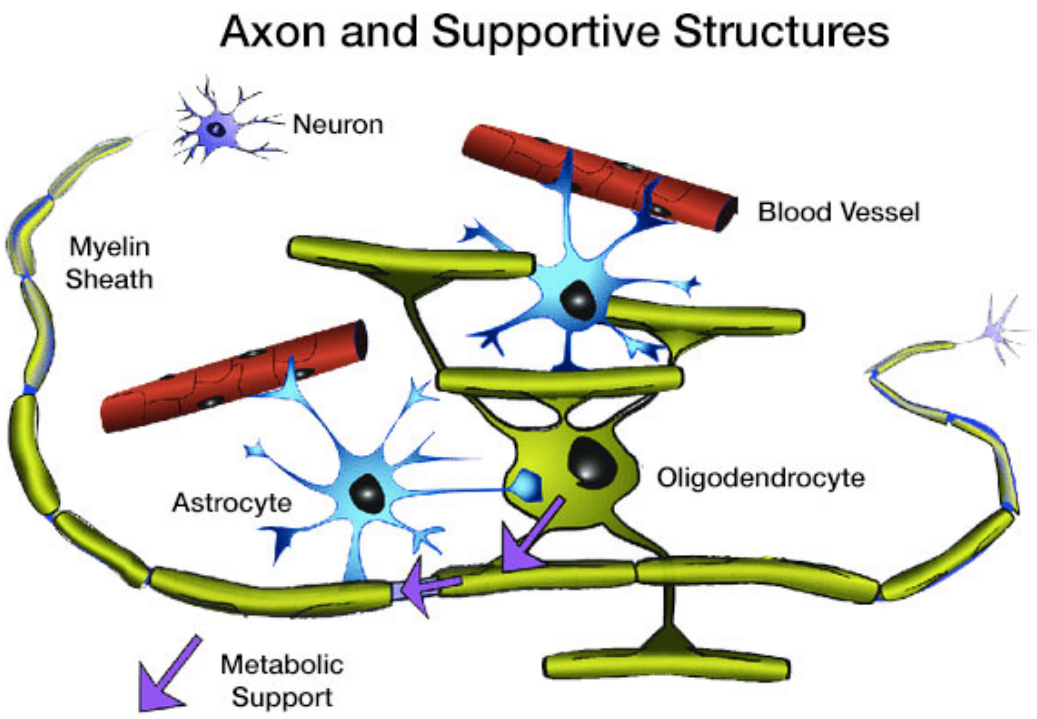

Figure 1.1: Axons (blue) are supported by various structures, such as myelin (green sheath), oligodendrocytes (green spindle), and astrocytes (light blue). These structures serve multiple functions including protecting and stabilizing the axon as it transmits signals between axons within the brain. *Adapted from Stassart, et al. 2018* [19]

Demyelination can occur through a number of factors due to pathology. In the case of traumatic brain injury (TBI), primary axonal injury occurs immediately following impact with axonal shearing, where both axons and the associated myelin are destroyed, and neuronal death throughout a multitude of WM regions [23]. This axonal and myelin-based damage causes the collapse of the associated oligodendrocytes serving both damaged and healthy neurons and leaves the healthy neurons in a demyelinated state, further decreasing tissue function. The damage to oligodendrocytes triggers inflammation within the region and microglial activation to eliminate dead tissue, which appears to progress over long periods of time, and as the cells die, they release molecules and proteins that induce a pro-inflammatory response of microglia and astrocytes.

Microglia are WM's primary immune defense system to ensure healthy growth and tissue regeneration [24,25]. Microglial cells act as macrophages and consume and destroy dead neurons and cellular debris through a process known as phagocytosis, and in particular, they are responsible for the clearing of degenerated myelin, which allows for oligodendrocytes to rebuild using new myelin. Secondary damage and injury in TBI often follows due to inflammatory responses including ischemia and brain edema from activated microglia post-insult [26,27]. If the microglia fail to properly clear damaged myelin from healthy axons, the remyelination process is slowed or halted and blocks the differentiation of oligodendrocyte progenitor cells. Dysregulation of the microglia creates a state of chronic neuroinflammation, further contributing to neurodegeneration, likely due to infiltration into regions adjacent to the initial insult site [28,29]. Due to the demyelination effects occurring over its course,

TBI causes increased risk of secondary WM demyelination pathologies such as Alzheimer's disease [30–32].

Additionally, astrocytes function as homeostatic regulators, ensuring proper functionality of neuronal and other glial cells [33,34]. During normal function in WM, astrocytes create long fiber-like processes that create junctures, both with other astrocytes to form a general matrix within the tissue and to other structures including neurons and blood vessels. Specifically, the processes connect to nodes of Ranvier and function as a bridge to the blood vessels through which glycogen flow to allow for powering of the axonal transmission. Astrocytes supply and control individual regions, or domains, with the necessary resources, but once the tissue suffers injury, the astrocytes proliferate and help form a barrier between the healthy and injured tissues, leading to glial scarring. While these glial scars prevent the effects of cell death and inflammation from reaching the healthy tissue and leading to further damage or infection, the scars also prevent cell regrowth or remyelination within these regions. As such, dysfunction of these cells during the aging process is believed to cause many pathologies, including Alzheimer's disease and multiple sclerosis.

Both Alzheimer's disease (AD) and multiple sclerosis (MS) are diseases that manifest as degradation to white matter through slow degeneration and death of oligodendrocytes, primarily due to toxicity from the surrounding cells. AD is typically characterized as a progression of two primary pathological factors, amyloid-beta plaques and neurofibrillary tangles, and these factors predominantly manifest in older populations [35–37]. One of the leading theories of AD's effects on WM is that of oxidative stress upon the oligodendrocytes, particularly that caused by amyloid-beta plaque toxicity [38]. As previously discussed, oligodendrocytes progenitor cells are

responsible for the differentiation of oligodendrocytes which are responsible for the myelination of axons, and oxidative stressors, such as amyloid-beta plaques, decrease the expression of the genes that allow for oligodendrocyte differentiation [39,40]. Oligodendrocytes also possess a natural vulnerability to oxidative stresses from a high iron capacity and low antioxidant content. Through these effects upon the oligodendrocytes, myelin integrity from oligodendrocyte regeneration is significantly diminished as researchers have found reduced myelin sheath thickness and shorter sheath lengths. As the integrity diminishes, the axons are left exposed to functional failure from trauma or further oxidative stresses. The demyelination and limited functionality of the regenerated myelin that takes itself place diminishes WM's functionality and leaves individuals with cognitive deficits. Alternatively, MS characteristically displays as an inflammatory response around focal brain lesions within the central nervous system and WM [41–43]. In MS, lesions affecting the WM specifically target and destroy oligodendrocytes. This demyelination and neurodegeneration in MS is the result of a combination of factors acting upon WM, including a cytotoxic inflammatory response to the brain lesions and the resulting microglia activation. Furthermore, oxidative injury results in mitochondrial damage and other downstream molecular consequences [44].

1.2 Skeletal Muscle: Structure, Function, and Pathology

While in-vivo analysis of WM dysfunction primarily focuses on cell death and breakdown of the primary supportive structures in WM, skeletal muscle provides the opportunity to evaluate both the structural makeup and the functional response of the tissue to assess its health. Skeletal muscle is comprised of a tiered categorization of tissues, beginning with full skeletal muscles (Figure 1.2A). A single muscle consists

of several fascicles, or bundles of muscle fibers, which are the individual cells within skeletal muscle. Muscle fibers are complex, multi-nucleated cells built from rod-like organelles called myofibrils, which are in turn comprised of many sarcomeres linked end-to-end (Figure 1.2B). These sarcomeres are the basic motor units of the human body that gives muscle its functionality and often described as a sliding filament model [45,46], where multiple smaller protein filaments, known as myofilaments, comprise this motor unit in a form that the primary myofilaments, actin and myosin, slide past each other to cause contraction. The actin and myosin mostly makeup thin and thick filaments within the sarcomere, respectively, and These two filaments provide the basic structure of sarcomeres, with the thick filament sliding between two thin filaments.

A pathology characterized by degradation and death of muscle fibers is Duchenne's muscle dystrophy (DMD), a progressive genetic muscle disorder [47]. This degradation is caused by a deficiency of the dystrophin protein, which functions as an assistive regulator of the extracellular matrix during muscle contractions, and the elimination or dysfunction of this protein means a disassociation between the extracellular matrix and the sarcomere-based actin myofilaments [48,49]. The disassociation of these structures causes a breakdown of the sarcolemma, the skeletal muscle cell membrane that handles mechanical stressors during activation in addition to standard cell membrane duties.

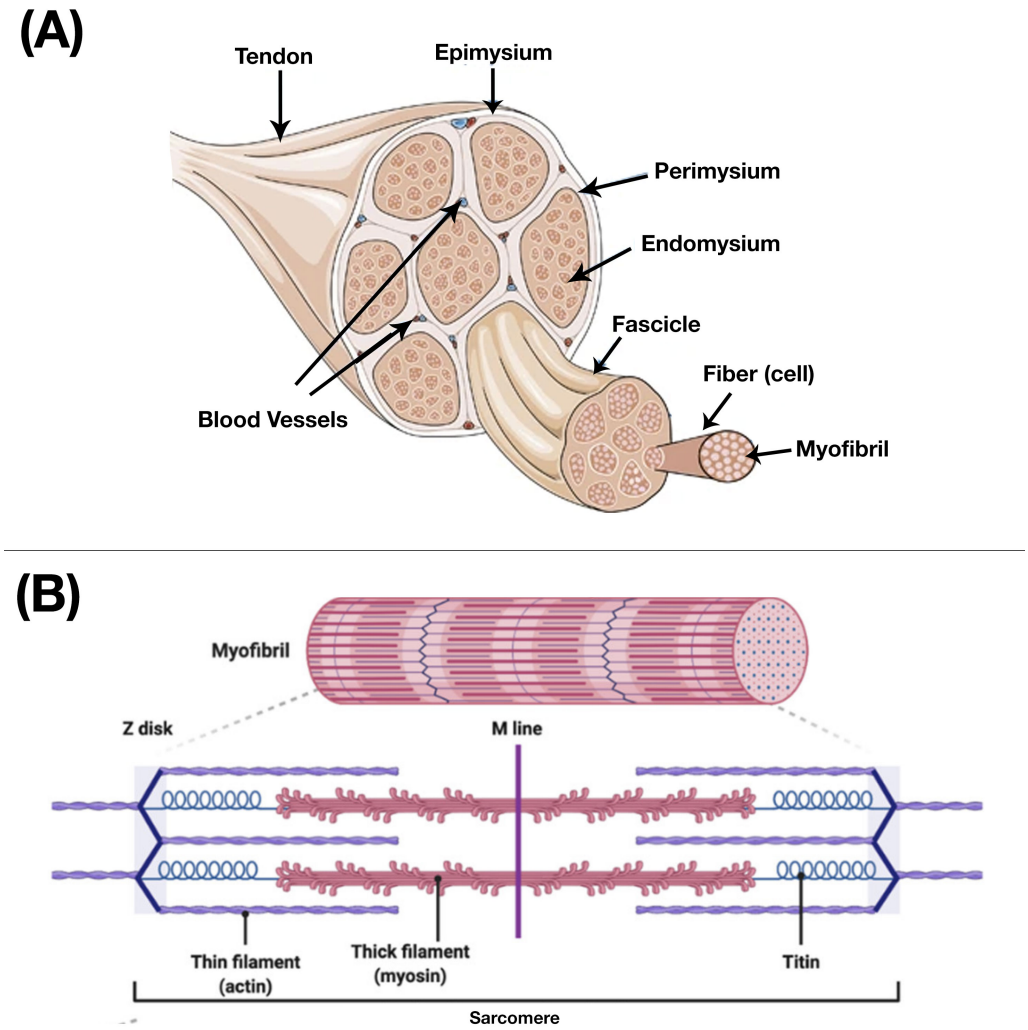

Figure 1.2: (A) Skeletal muscle consists of a hierarchal structure of fibers and other supportive structures. The fibers are made of (B) sarcomeres which consist of three primary protein based myofilaments, actin, myosin, and titin. *Adapted from Sciorati, et al. 2016 and Tharp, et al. 2020* [50,51].

In functional loading through active tension, myosin and actin generate force through cross-bridge cycling, which refers to the connection created by the myosin head attachment to a tropomyosin attachment point on the thin filament and these myosin heads attach and detach repeatedly to walk along the length of the thin

filaments, creating a tension both longitudinal and perpendicularly within the filaments. The longitudinal force then transfers to the Z-discs on the ends of the sarcomeres, eventually moving the limbs through the tendons. The releasing of the bond creates causing a power stroke from the myosin head, pushing the actin filaments towards one another.

Cross-bridge theory also helps explain tissue activation during another contraction condition, isometric contraction, during which the sarcomeres maintain length, even during loading [52]. During isometric contraction, myosin heads attach to the actin in the typical cross-bridge manner, yet do not cause the typical ensuing power stroke. Instead, the cross-bridge twitches, sending short tension impulses along its length and therefore, not constantly being strongly attached to the tropomyosin binding site. Instead the myosin heads spend only a short time strongly attached, which is known as a duty cycle, and both time between force-inducing pulses increases and number of heads increase as the total loading of the tissue increases.

While actin and myosin have been the primary myofilaments used describing muscular responses and functionality, recent studies have suggested the presence of a third myofilament called titin [53–55]. An elastic filament, titin acts as a molecular spring and possesses the distinctive ability to regulate its spring stiffness in response to stimuli. The elastic filaments help loosely hold the actin and myosin together when they are not actively binding and assist in the transmission of force between the actomyosin and the Z-discs. By supporting these structures in this manner, titin creates the tissue response for muscle lengthening as it naturally stretches according to its spring constant and giving rise to natural muscle stiffness. During active contraction however, titin plays a slightly different role and binds to calcium and then binds to

actin to increase its own stiffness and applied force during active contractions. This increased stiffness largely stabilizes sarcomeres during the descending limb of the force-length curve (Figure 1.3A) and preventing damage the center of sarcomeres (A-band) when fully or nearly-fully actively stretched.

Sarcomeres are maintained within an ideal muscle length range, called resting length, due to titin elasticity and attachment of muscles to bone through tendons, which keeps the muscles under constant tension [56–58]. If separated from the bone or the tendon, the muscle retracts and significantly shortens in length. Muscle length plays a significant role in regulating both the base tension and the force production, with deviation from the resting length, either longer or shorter, significantly decreasing the total possible tension generated. This variation in tension potential results from overlap between of actin and myosin myofilaments within the sarcomeres, with ideal length ranging from 80-120% of base sarcomere length.

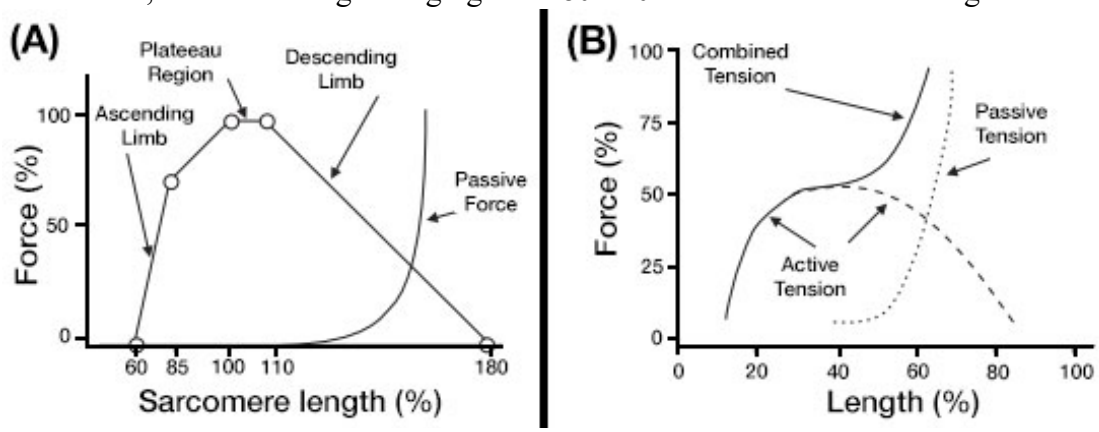

Figure 1.3: The force output from muscles is a component of (A) relative sarcomere length and (B) combined tension level for the overall muscle. *Adapted from Brughelli, et al. 2007* [59]

Injury and pathology can drastically affect skeletal muscle length, and thereby affect the optimal sarcomere length (Figure 1.3A) and combined tension curves (Figure 1.3B). Muscle strain injuries leading to damage in skeletal muscle can lead to many primary and secondary pathologies that affect movement in both the short and long term with the most common form occurring during eccentric, or loaded lengthening, muscle actions, as these actions are significantly less stable, particularly near full extension, than either isometric or concentric contraction [60]. Damage during eccentric loading includes that at the ultrastructural level, both immediate and up to seven days following initial tissue insult. Proske, et al. suggests the primary sign of this initial damage is the overstretching of sarcomeres, which causes a cascade of structural disruption, including alignment errors between the various filaments [61]. The alignment error is believed to be caused by a disruption of titin's elastic properties or the securing Z-discs by a protein called desmin. Studies have suggested that the increased compliance of the muscle from the overstretched sarcomeres shifts the force output curve, requiring a longer muscle to achieve the same force output [59]. From this point, muscle shows adaptation through these disrupted sarcomeres do not fully reset to their previous alignment, meaning the surrounding sarcomeres shorten compared to pre-contraction length and therefore require increased stretching before a noticeable level of tension occurs in the tissue. This shortening of sarcomeres is accounted for by an increased number of average sarcomeres per muscle fiber and increased tissue compliance and ability to reproduce the same eccentric loading without reinjury [62,63].

While injury through eccentric exercise results in shorter sarcomeres, spasticity from pathology such as cerebral palsy (CP) can result in longer and therefore less

functional sarcomeres [64] as well as increased extracellular stiffness. Spastic CP results from a primary injury to the brain or abnormal development during pregnancy, childbirth, or shortly thereafter [65,66], affecting the motor cortex of the brain. Over the course of healthy development, stretching occurs on relaxed muscle with standard physiological loading, but in those affected by spastic CP, the damage to the motor cortex limits muscle's ability to relax due to the neuromuscular spasticity [67,68]. Tissue development under these conditions produces significantly stiffer muscles, limiting force production and joint range of motion, therefore limiting subject mobility and movement [64].

1.3 Thesis Overview

Therefore, evaluation of these fibrous soft tissues requires a technique capable of capturing changes, such as WM structural changes like demyelination and skeletal muscle functional changes like spasticity, in-vivo. As previously stated, imaging techniques, specifically MRE, should provide a basis for the assessment of fibrous soft tissue health through characterization of these changes.

In this thesis, we propose to develop and test an MRE method to evaluate the health of fibrous soft tissues by evaluating structural and functional changes from pathology or injury. To accomplish this, we aim to quantify the viscoelastic mechanical properties of skeletal muscle and WM using MRE. Particularly, we evaluate multiexcitation MRE's ability to create unique waveforms throughout the entire brain with two orthogonal excitations, AP and LR, by investigating the generated wave propagation patterns within the human brain and the resulting slow and fast waves within white matter. Using this multiexcitation MRE method in combination with an anisotropic inversion method, we quantify the anisotropic

viscoelastic mechanical properties of white matter tracts and analyze tract heterogeneity, demonstrating the capacity of this technique to quantify structural differences of fibrous soft tissue. Additionally, we employ MRE to quantify the mechanical response of skeletal muscle to isometric contraction under multiple loading conditions. We further investigate MRE's ability to capture the functional response of skeletal muscle by estimating the anisotropic viscoelastic material parameters in the gastrocnemius and how these parameters change during both passive and active loading conditions.

Chapter 2

TECHNIQUES FOR *IN-VIVO* EVALUATION OF FUNCTION AND STRUCTURE IN FIBROUS SOFT TISSUE

2.1 Overview

Human soft tissues are highly complex amalgamations of multiple individual structures, some of which are function drivers while others support those functional mechanisms. In-vivo analysis allows for examination of these tissues' interactions without missing their interactions with surrounding supportive structures or even with other tissues. Multiple techniques exist for in-vivo investigation of tissue, though some methods are more advantageous to employ during investigation of certain tissues or when investigating an aspect of a tissue. Tissue evaluation of fibrous soft tissues like brain and skeletal muscle often leverage electrical stimulation and soft tissue imaging methods, such as ultrasound and magnetic resonance imaging (MRI). Though some methods measure of tissue function while others measure structural differences, utilizing a technique that allows for the simultaneous capturing of both functional and structural aspects of tissue will result in a more complete assessment of tissue and the effects of pathological and injury-based degradation.

2.2 Electrical Stimulation Techniques

Many of the body's important tissues are involved in the sending and receiving of electrical signals and the resulting feedback. The brain both sends and receives electrical signals between its internal neurons and other tissues in the body, including

skeletal muscles and the heart, to regulate the function of these tissues. While multiple methods of measuring these electrical signals may be used to evaluate the function and health of these tissues [69], these techniques usually have methodological differences in how they collect the signal owing to unique factors in each tissue. For instance, characterization of neurological electrical signal is known as electroencephalogram (EEG) [70–72], which is often used for diagnostic or treatment purposes with brain tumors [73–75], brain dysfunction or damage [76–78], and stroke [79–81]. Heart electric signal output is measured similarly through an electrocardiogram (ECG or EKG) [82–85], which is mostly used for evaluation of heart rhythm for diagnosing arrythmias [86,87] and coronary artery disease [88]. While both techniques are non-invasive through surface-level application of electrodes, the interface between the electrode and the skin may be compromised by any substances or other confounding factors, which may impact signal accuracy [89,90]. In skeletal muscle, researchers apply the method electromyography (EMG) through either the non-invasive surface-level technique surface electromyography (sEMG) [91,92] or the invasive technique known simply as EMG, where the electrodes are inserted directly into the muscles [93,94].

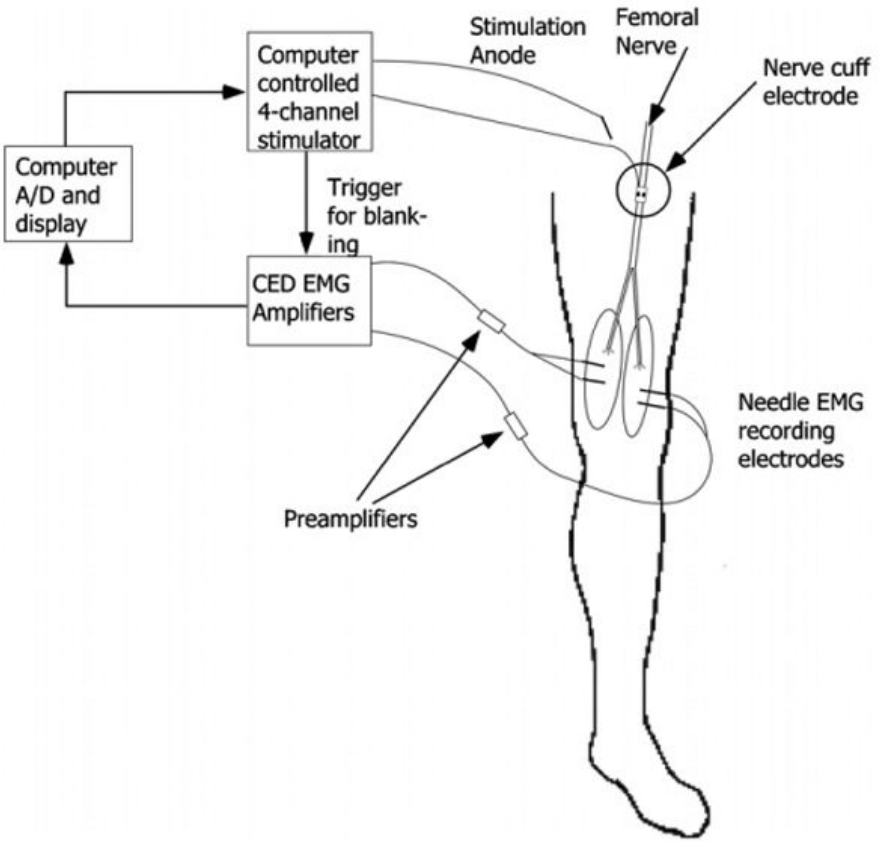

Figure 2.1 A diagram of the generalized setup and readout of electromyography. *Repurposed from Polasek, et al. 2009* [95]

Electrical stimulation techniques evaluate the functional response of the evaluated tissue, as changes to the static electrical output only manifest during variation in functional output. As such, sEMG measures the tension output of muscle during active contraction but lacks information about the structural integrity of the muscle during other periods [96]. By measuring these functional outputs, researches have utilized sEMG for diagnostic purposes in muscular injury and diseases including cerebral palsy [97–100] and muscle dystrophy [47,101,102]. While they are the gold standard in relating muscle function of individual muscles with force output in

kinematics studies of skeletal muscle, sEMG methods are limited in their ability to directly quantify force generated in individual muscles . As the electrodes are placed on the skin, sEMG also cannot reach the deeper muscles within muscle groups, limiting its ability to analyze an entire tissue at once. Overall, while sEMG and other electrical stimulation methods provide useful functional tissues estimates, they are limited in their capacity to provide a holistic evaluation of soft tissue health and degradation. For non-invasive evaluation of soft tissues and for diagnostic purposes, imaging techniques as a whole are the gold standard, offering researchers and clinicians a variety of techniques depending on the pathology being investigated.

2.3 Ultrasound Imaging

Ultrasound imaging utilizes a transducer to generate high frequency acoustic waves that propagate through human tissue [103–106]. Upon reaching a tissue, these waves can continue propagating through the tissue, reflect back to the transducer, or scatter. The image is then reconstructed from the wave reflections read by the transducer. Researchers and clinicians may produce 2D, 3D, and 4D images of internal tissues or perform real-time mapping of tissues and blood flow, allowing them to evaluate the properties of the internal soft tissues.

Functional ultrasound, consisting of either Doppler ultrasound or ultrasound elastography, is both a clinically viable technique while also providing multiple avenues of research in both the brain and skeletal muscle tissue. Doppler ultrasound offers a quick and cost-effective method of measuring the blood flow velocity in a tissue using low frequency acoustic waves and allows for the acquisition and monitoring of blood flow velocity over extended periods of time, all while maintaining a high temporal resolution during the imaging process [107]. The technique has found

limited success in the assessment of function in skeletal muscle, primarily used for evaluation of the effects of exercise [108,109] and pathology such as fibromyalgia [110,111].

2.3.1 Ultrasound Elastography

Ultrasound elastography (USE) is primarily used to evaluate two types of soft tissue in clinical settings, liver [112–115] and skeletal muscle [49], though it has also been used to evaluate others including breast [116,117], thyroid [118,119], and prostate [120]. Functionally, USE techniques measure tissue displacements, which can be created through external compression, a secondary transducer, or the original transducer [121]. The most common USE technique in the application to skeletal muscle is shear wave elastography (SWE), which generates displacements using acoustic radiation force, creating longer wavelength shear waves from a secondary actuator that propagates perpendicular to the primary transducer's waves [122–124]. The primary transducer captures this wave propagation through displacements, from which shear wave speed (C_s), which can be reported or converted to Young's modulus (E), can be measured. SWE has primarily been used to evaluate muscle mobility and compare dynamic tissue properties as altered by pathological changes. USE has primarily been utilized as a means to directly measure muscle stiffness and the effects of functional or pathological changes on the tissue [125,126]. Specifically, USE has shown alterations in passive tension levels during muscle lengthening in cerebral palsy [124] and post-stroke [127].

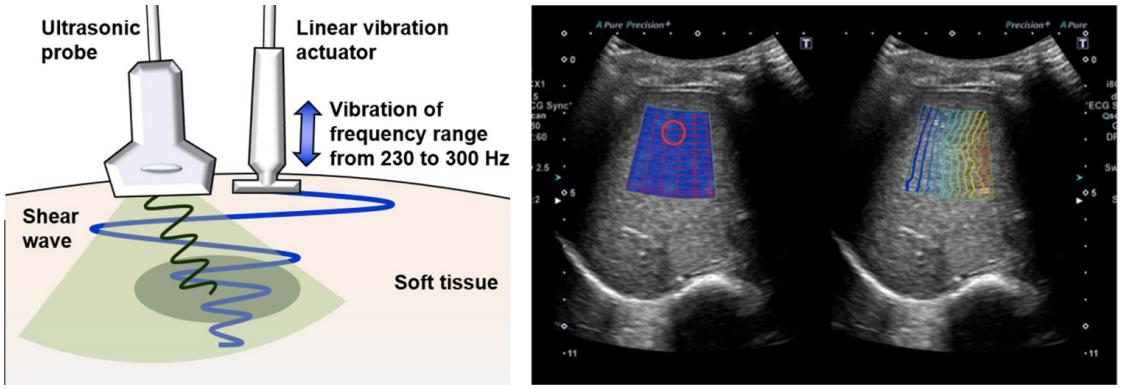

Figure 2.2: [*Left*] The experimental method of shear wave elastography (SWE) using two actuators to acquire [*Right*] displacement images. *Adapted from Tsuchida, et al 2020 and Nakayama, et al. 2021.* [128,129]

Ultrasound possesses some technical limitations including shadowing, reverberation, and clutter artifacts, though advances in technology may overcome these challenges. Two of the largest limitations that affect USE are simply innate issues with ultrasound. One of these is operator error that is the tradeoff of the flexibility and mobility that ultrasound allows, while the other is the low field of view (FOV) provided by ultrasound, making it more difficult to acquire large amounts of data simultaneously. Wave attenuation is particularly problematic in USE as the signal diminishes when the waves penetrate deeper into tissue or passes through fluid or fatty tissue, making assessment of deep tissue or organs more difficult. The reproducibility of data is affected by varying levels of applied stress due to acquisition, non-standardized system settings and parameters, and region of interest (ROI) selection by the operator and presents challenges to comparison of data from various studies and research groups.

While USE techniques present advantages, current commercially available USE makes assumptions about the tissue that do not fully describe the material when

considering skeletal muscle. All tissues evaluated by these systems are considered (1) linear, (2) elastic, (3) isotropic, and (4) incompressible. In particular, the two assumptions that least accurately describe skeletal muscle are: (2) elastic, which implies that strain rate plays no part in the measurements; and (4) isotropic, which means evaluation of the tissue from any direction will produce equal property estimates. Studies have previously shown that many human tissues, including skeletal muscle, are complex materials that react in both a viscous and an elastic manner while under strain, meaning that Cs and E, the mechanical properties of the tissues, are strain-rate dependent. Classifying skeletal muscle as isotropic ignores the fibrous nature of the tissue, which when mechanically evaluated has been proven to produce directionally-dependent material property values. These issues stem more from the modelling used rather than USE as a whole, so improvement may come with future progression of the technique.

2.4 Magnetic Resonance Imaging

2.4.1 MRI Physics

One of the most widespread imaging methods due to its relative safety and large field of view is magnetic resonance imaging (MRI). MRI utilizes the phenomenon of nuclear magnetic resonance (NMR), which is where certain atomic nuclei, such as hydrogen, ^{1}H, "spin" on their own axis and generate a magnetic moment [130–133]. This creates a local magnetic field with a north and a south pole around the atomic nucleus. A strong external magnetic field (B_0) applied to an area aligns all of the spins of the nuclei within this field in one of two directions, either parallel or perpendicular to the B_0 field direction. In a solid material, nearly all of

these spins will be parallel with the B_0 field. The angular velocity at which any nuclei spins is known as its Larmor frequency, the equation for which is:

$$\omega_0 = \gamma * B_0 \tag{1}$$

, where ω_0 is the Larmor frequency, γ is the gyromagnetic ratio which is a known constant for each nucleus, and B_0 is the field strength of the applied field. MRI uses a large static magnetic field to align spins of the nuclei, usually ^1H, within the region of the body, with scanners operating 0.5T, 1.5T, or 3T B_0 fields for clinical work.

Then, a smaller radiofrequency (RF) field, B_1, is applied to excite the B_0-aligned nuclei, usually in short microsecond pulses known as RF pulses. The resultant energy transfer causes the nuclei to fall out of alignment and into a higher energy state, which releases that energy when the pulses end and the nuclei realigns with the B_0 field. The energy differential creates a voltage that can be picked up by a tightly coiled metal wire, or RF coil. The electrical signal that is collected by the RF coil, known as free-induction decay (FID), can then be read by a computer and interpreted using a Fourier transform to identify the signal in the FID. However, these readouts can only establish the signal from a singular area since there is no spatial variance to the readout signal, only temporal.

To combat this spatial analysis problem, MRI utilizes what are called gradient magnetic fields where users apply gradient coils to induce a linearly-varying magnetic field in one of the three directions orthogonal to the B_0 field, which can be considered as G_x, G_y, and G_z, where G_z is aligned with the B_0 field. During the application of these gradients to the area, the linearly-varying magnetic field causes variations in the

atomic spin frequencies. A Fourier transform is then applied to the RF coil readout, transforming the different frequencies from having frequency variation to spatial variation as the data is converted into image space. The time the nuclei take to return from their RF-excited states to alignment with the B_0 field are known as relaxation times, where T1 relaxation time measures the time it takes for a proton to realign with the B_0 field and T2 relaxation time measures the time for the nuclei to fall out of B_0 field alignment after the B_0 field is turned off. The difference between T_1-weighted and T_2-weighted imaging are primarily from the echo time (TE), or the time between excitation by an RF pulse and the peak amount of the signal induced the coil, and from the repetition time (TR), or the time between RF pulses. Different materials have different relaxation times, so using various TEs and TRs between MRI pulse sequences will change the output signal.

2.4.2 Diffusion MRI

Diffusion-based MRI is an important MR technique for characterizing the structure of fibrous tissues. Diffusion MRI (dMRI) quantifies the movement of water molecules within tissue, whether it be random as in the case of unconstrained molecules or in a particular direction like their movement when physically restricted [134,135]. Most studies of fibrous soft tissues utilizing dMRI evaluate the restricted flow of water in preferential directions, which aligns with the primary direction of these fibers. These measurements are achieved through the quantification of the spins dephasing within a voxel based upon the overall random motion of water molecules. Determination of the preferential direction of diffusion of these molecules is done by solving for the diffusion tensor, which describes relative direction and amplitude of water molecule movement for a point in space. Diffusion tensor imaging (DTI)

accomplishes solving for this tensor by acquiring diffusion data in at least six non-collinear directions, and as such, its primary use is within fibrous tissues, such as white matter (WM) and gray matter of the brain as well as skeletal and heart muscle, since water molecules with mostly diffuse in the direction aligned with a tissue's internal structure. The diffusion tensor can be processed to produce six primary parameters at every point in the image consisting of three eigenvalues (λ_1, λ_2, λ_3) and three eigenvectors (V1, V2, V3). By using these values, researchers and clinicians obtain a measure of the anisotropy, or directional dependency, and diffusivity of fibrous tissues, through quantifiable measures such as fractional anisotropy (FA) [136–138].

$$FA = \frac{\sqrt{3\left(\left(\lambda_1 - \hat{\lambda}\right)^2 + \left(\lambda_2 - \hat{\lambda}\right)^2 + \left(\lambda_3 - \hat{\lambda}\right)^2\right)}}{\sqrt{2(\lambda_1^2 + \lambda_2^2 + \lambda_3^2)}} \tag{2}$$

In fibrous soft tissues, including skeletal muscle and WM, FA is the primary metric for tissue integrity and has been used to evaluate both functional and structural changes to tissue from aging, pathology, and other sources of degradation. With evaluation of skeletal muscle using dMRI, researchers found correlations between FA and muscle length [139–141]. Additionally, studies have demonstrated quantifiable changes in FA in skeletal muscle pathology such as Duchenne muscle dystrophy [142,143]; in WM degradation due to aging [144–146]; and in pathologies such as epilepsy [147,148], Alzheimer's disease [149,150], and TBI [151,152]. However, dMRI does not currently have a means of measuring functional loading of skeletal muscle during contractile states, limiting its scope as a measure of tissue function.

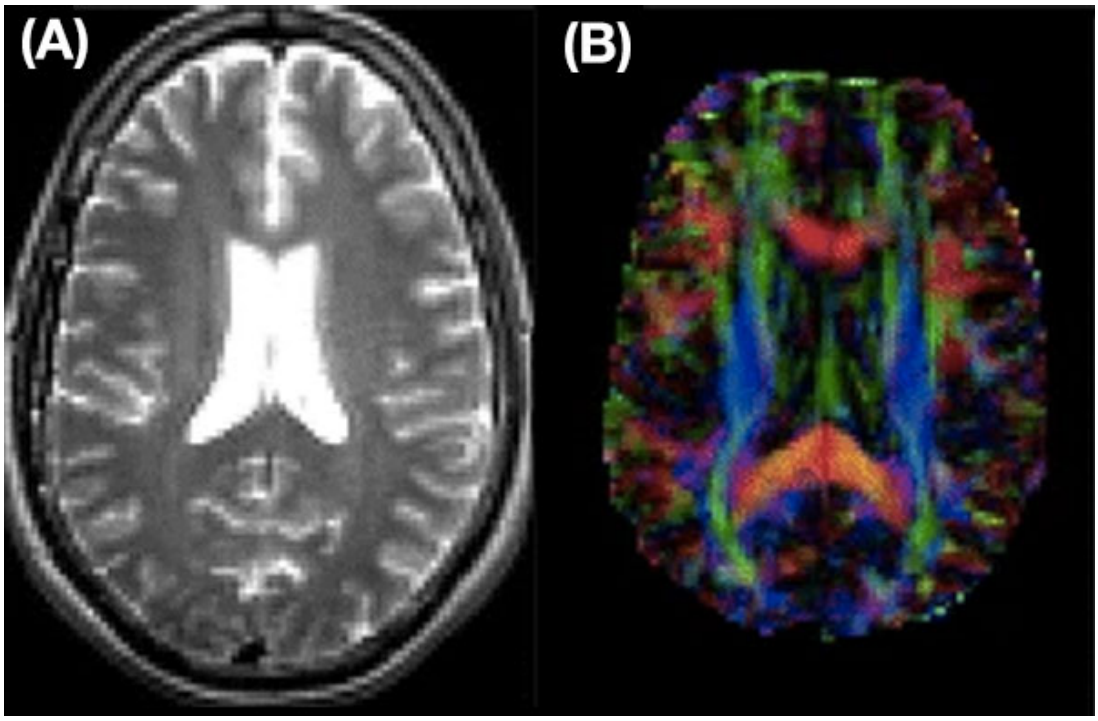

Figure 2.3: Standard MRI structural scans of the brain include (A) T1-weighted anatomical scans and (B) diffusion tensor imaging (DTI) scans, which indicates general fiber direction of white matter by colorization. *Adapted from Assaf, et al. 2008* [153]

2.4.3 MR Elastography

Magnetic resonance elastography (MRE) is one such technique that allows for in-vivo mechanical property estimation in human tissues including liver [154,155], brain [11,156–158], and skeletal muscle [13]. MRE is a phase contrast MRI technique that utilizes harmonic shear wave propagation imaged using a conventional MRI scanner with a modified MRI pulse sequence to estimate the viscoelastic mechanical properties of soft tissue [6].

In MRE, shear waves are generated using external drivers such as electromagnetic, piezoelectric, or pneumatic actuators [159]. Electromagnetic

actuators are simple and easier to make and control than the latter two while still being capable of generating actuations at a wide range of frequencies. However, electromagnetic actuators can cause complications when positioned within B_0, creating image distortions. Alternatively, piezoelectric actuators can produce much higher excitation frequencies but conversely generate low amplitude waves that require a secondary amplification device to boost amplitude of the propagating waves.

The most common actuator in research, pneumatic actuation uses an active driver in the MRI control room to pump compressed air through a tube into a passive driver component placed against the skin of the subject. The air is pumped to create oscillatory acoustic waves that are transferred from the passive driver to the subject. The primary limitation of pneumatic actuation is a more limited range of useable vibrational frequencies, but these ranges are acceptable for the typical frequencies of MRE. The generated acoustic waves create propagating shear waves through the tissue with micron-level displacements, usually between 5-50 microns.

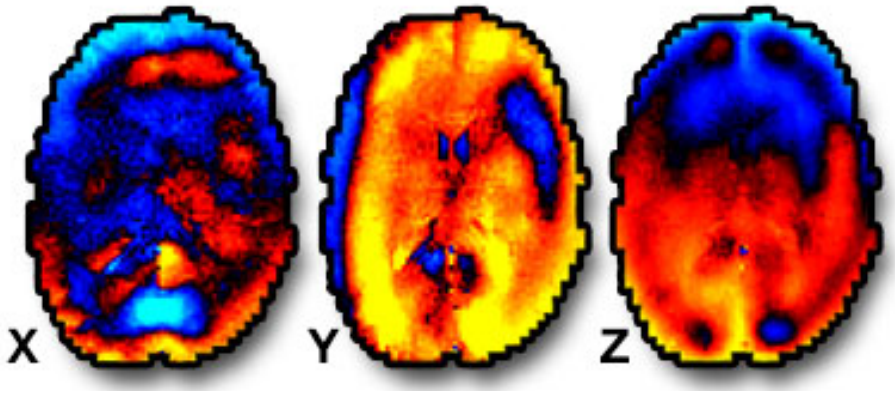

Figure 2.4: Shear waves are generated using actuators and shown here in a single slice of a brain, generated using a pneumatic actuator at 50 Hz vibration frequency.

Another key component of the propagating shear waves, shown in Figure 2.4 , is the vibration frequency. Most MRE studies operate in the frequency range of 30-70 Hz. As with USE, the shear waves attenuate, or dissipate, as they travel through the tissue, with lower frequency waves able to travel further into tissue before attenuating than higher frequency ones. However, higher frequencies have shorter wavelengths and thus have the potential for greater spatial resolution. Higher frequency requires a higher input amplitude to generate equal levels of tissue displacement as at a lower frequency in the same tissue, though too low of a frequency can also result in subject discomfort due to greater perception of the applied motion. While there is no standard between MRE research groups, general ranges for certain tissues include 50-60 Hz for brain [160,161] and ~60 Hz for liver [9,162]. It is important to note that due to the viscoelastic nature of soft tissue, the estimated properties are frequency-dependent, as the tissue's response changes based upon the rate of strain caused by the shear waves.

These wave motions are captured in the phase of the MRI image using a modified MRI pulse sequence that employs motion encoding gradients (MEG) in addition to the standard MRI sequence components. By applying the MEGs, the pulse sequences encode the spins with a trajectory into the phase image, from the phase encoding gradients, allowing for the estimation of total tissue displacement from accumulated phase during each time point. As the MEGs change the frequency of the atomic spins based upon their relative position, the displacements from the propagating shear waves cause accumulation of phase during the course of the scan due to the altered spin frequency.

The wave displacements imaged with the MRE pulse sequence are used to estimate mechanical properties of tissue with behavior described by the Navier's equation (3),

$$\nabla \cdot (G(\nabla \boldsymbol{u}(f) + \nabla \boldsymbol{u}(f)^{\boldsymbol{T}})) + \nabla(\lambda \nabla \cdot \boldsymbol{u}(f)) = -\rho\omega^2 \boldsymbol{u}(f) \tag{3}$$

where G is the complex shear modulus of the material, $\boldsymbol{u}(f)$ is the three-dimensional displacement vector, λ is the Lame constant, ρ is the material density of the medium, and ω is the angular frequency of the applied vibration [16]. Through application of a mathematical inversion algorithm, we can calculate the underlying mechanical properties from the imaged displacement of the tissue.

Most studies in MRE operate under a material assumption of mechanical isotropy, or directionally-independent properties, and use some component of one of several inversion algorithms including local frequency estimation (LFE), local direct inversion (LDI), and non-linear inversion (NLI) [5], with LDI and NLI being the two primary methods for single frequency isotropic inversions. LDI assumes homogeneity of the tissue to simplify the equation, often along with a curl operator to eliminate the pressure term, ultimately resulting in the Helmholtz equation (4).

$$G\nabla^2 \boldsymbol{u}(f) = -\rho\omega^2 \boldsymbol{u}(f) \tag{4}$$

The end result uses 6 equations (real and imaginary parts of the Helmholtz equation in three directions), which are solved for two unknowns (the real and imaginary part of the shear modulus) using a least squares inversion technique. LDI's solution involves solving the system algebraically with the second derivative being

determined numerically, which creates a simple solution but one which is sensitive to noisy data.

NLI is a finite element-based optimization algorithm that involves solving two discrete problems: a "forward problem" and an "inverse problem" [163]. The forward problem calculates expected displacement fields from an estimated set of material properties, which, in the case of an isotropic material model, are the storage and loss modulus, G' and G''. On the other side, the inverse problem updates the unknown mechanical property distribution based on differences between calculated and measured displacements. NLI solves the inverse problem as an iterative minimization of the objective function in equation (5),

$$\Phi(\theta) = \sum_{i=1}^{N_m} \left\{ \left(u_{m(i)} - u_{c(i)}(\theta) \right) \left(u_{m(i)} - u_{c(i)}(\theta) \right)^* \right\} \tag{5}$$

where $u_{m(i)}$ represents the complex amplitude of the *i*th displacement of the iterative problem, $u_{c(i)}(\theta)$ is the displacement calculated by the forward model using the FEM based upon properties in *i*th iteration of the model, N_m is the total number of measurements, * represents the complex conjugate, and θ is the matrix of properties being solved for, including both material (G' and G'' for isotropic) and spatial (x, y, z). To solve the forward problem, a partial differential equation is used to describe mechanical motion with boundary conditions, which are applied around the exterior of the problem domain. The most common form of NLI used in MRE employs a subzone method [164], which, due to displacements available through the tissue, enables faster solving through parallel data solving. The subzone method generates a mesh with nodes arranged in a grid that is created from the MRE displacement data. NLI is run in

each of the subzone regions within this mesh, and after a number of cycles, the subzone nodes are adjusted to generate a new set of subzone regions, where the process repeats before assembling the global distributions from the final subzone solutions.

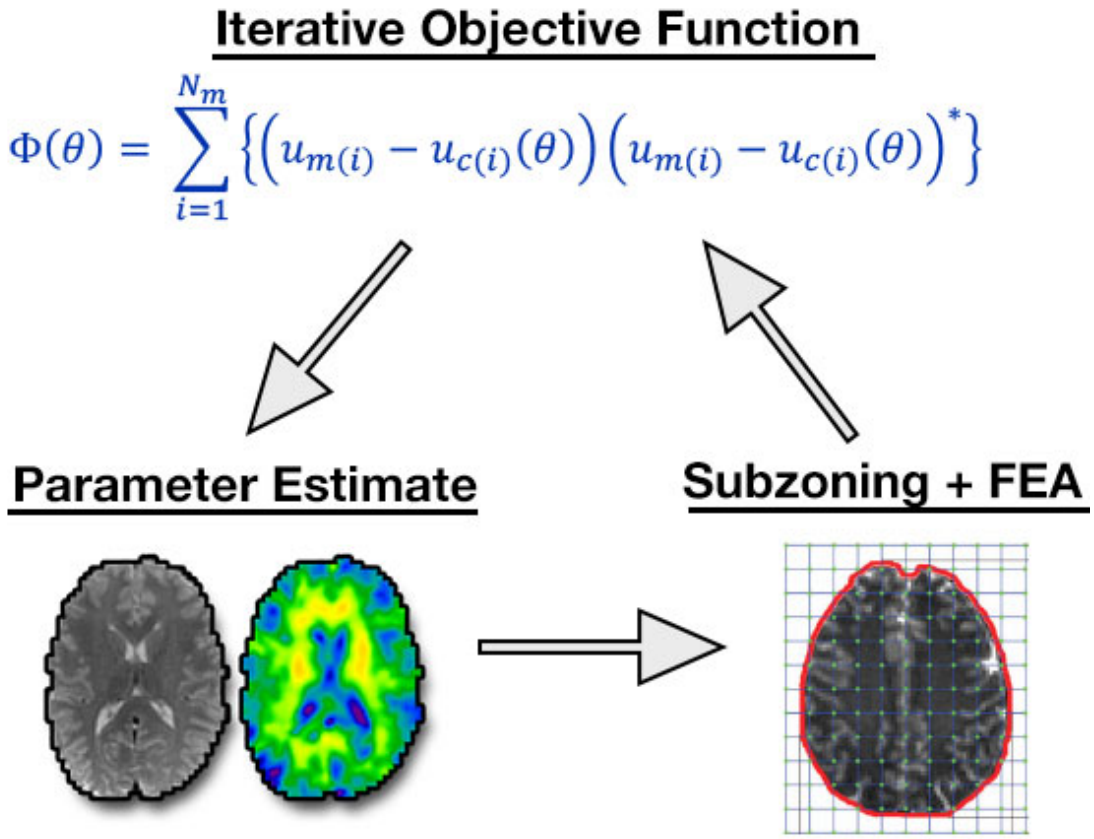

Figure 2.5: The iterative process of NLI consists of three primary parts: the parameter estimate, creation of the FEA model utilizing subzones, and comparison to original data using the iterative objective function. *Adapted from McGarry, et al. 2012* [163]

As previously stated, researchers utilizing MRE have investigated a variety of tissues, as well as analyzed the pathologies of these tissues. Though a relatively new technique, MRE has been used to evaluate the mechanical properties of soft tissue and

to quantify structural and functional changes from healthy or development or decline due to pathology, injury, or aging. The primary role of MRE in the clinical setting is the investigation of liver health and the characterization of hepatic disease [9]. Specifically, clinical use of MRE assesses fibrosis and cirrhosis of the liver, pathology increasing tissue stiffness traditionally assessed through palpation. As with most other MRE techniques, MRE of the liver assumes tissue isotropy for parameter estimation, including studies investigating brain and skeletal muscle. Although most MRE studies have been utilizing an isotropic material model for mechanical property estimation of soft tissues, the application of an isotropic model doesn't fully capture the complexity of fibrous soft tissues within the human body, including skeletal muscle and brain white matter.

In tissues such as brain and skeletal muscle, an anisotropic material model is necessary to better quantify behavior and pathology, as exclusion of these parameters can lead to a model-data mismatch and result in inaccurate assessment of tissue response. Several anisotropic MRE methods have been proposed, varying in both the underlying anisotropic material model, and therefore the corresponding number of material parameters estimated, and the inversion algorithm to solve for these parameters. Material models utilized in MRE include two, three, or five material to be estimated.

Sinkus, et al. 2005 [165] proposed a method while analyzing breast tissue in vivo using a transversely isotropic (TI) model with two independent material parameters, shear moduli parallel and perpendicular to the fiber bundle, $\mu_{\parallel}$ and $\mu_{\perp}$. A TI model proposes that the fibers of a material are aligned so that rotation about the central axis of these fibers does not change the properties of the material. This method

then uses a Helmholtz-Hodge decomposition to solve the material model's derived partial differential equations (PDEs) describing the two shear moduli parameters. This methodology was used by Green, et al. 2013 [166] to investigate skeletal muscle in the primary calf muscles, modeling the shear anisotropy of the soleus, tibialis anterior, and gastrocnemius. This anisotropic material model of a transverse isotropy was the earliest utilized in MRE but also is the simplest presented so far.

Another early method, proposed by Romano, et al. 2012 [167] utilized a higher order anisotropic model, using five material parameters in a TI elastic tensor to describe the corticospinal tract of the brain. This technique combines DTI, MRE with waveguide elastography, and the Helmholtz decomposition. With waveguide elastography, Romano, et al. isolates the shear waves travelling along the fiber axis, as defined by the collected DTI data, through the Helmholtz decomposition.

More recent investigations have employed a three parameter method, a middle ground between the two previous methods. Tweten, et al. 2015 [168] and Guo, et al. 2016 [169] use a TI material model but make an assumption of tissue near-incompressibility, which appears to be a valid assumption based on the volumetric strain being significantly smaller than the shear strain in MRE in brain and skeletal muscle tissues. This assumption reduces the number of parameters from the five used in Romano, et al. to the three used in these studies. The primary element that this captures that is otherwise excluded from the two-parameter method is the tensile strain from the propagating shear and longitudinal waves. However, this is where the two techniques differ, as Guo, et al. uses Young's modulus parallel to the fiber direction while the method used by Tweten, et al. model's for tensile anisotropy, combining modeling the relationship between Young's modulus parallel and perpendicular to the

fiber direction. These studies also differ in the methods used to estimate these parameters within the models using MRE data sets, though both follow an idea presented by Romano, et al. 2012 suggesting that anisotropic models require more than one wavefield to properly resolve the TI model's system of equations. In Guo, et al., the three parameters in skeletal were analyzed under a theory of linear elasticity using multifrequency dual elasto-visc (MDEV) based inversion [170–172] utilizing four driving frequencies, allowing for an overdetermined inverse problem. Meanwhile, Tweten, et al. based their method upon directional filtering of simulated MRE data to acquire additional information along with slow/fast shear wave component analysis. These two methodologies presented by Tweten and Guo demonstrated the viability of using a three-parameter estimation method of a TI material to quantify anisotropic viscoelastic property differences, with Tweten, et al. solidifying the parameters as substrate shear modulus, tensile anisotropy, and shear anisotropy.

As previously mentioned, Romano, et al. 2012 suggested and Guo, et al. and Tweten, et al. reinforced the need for multiple waveforms to fully solve for the anisotropic viscoelastic mechanical properties of fibrous tissue. While both of these methods have proposed methods of gathering this data, Anderson, et al. 2016 [173] presented a third option: multiexcitation MRE. Multiexcitation MRE utilizes two separate pneumatic passive drivers positioned orthogonally to generate waveforms distinct from one another throughout the tissue of interest, which, in the case of Anderson, et al., was the brain. These drivers were connected to the primary actuation device during independent MRE scans so as to generate separate wave motion and isotropic property maps. This study displayed the directionally material properties inherent to white matter structures, including the corpus callosum, corona radiata, and

superior longitudinal fasciculus, through the placement of orthogonal pneumatic actuators behind the skull, generating an anterior-posterior (AP) excitation, and on the side of the skull, generating a left-right (LR) excitation. However, no previous works have quantified how these waveforms within the tissue differ and whether this methodology is feasible as a means of estimating the anisotropic properties of soft tissue.

MRE provides a means of evaluating both structural and functional aspects of soft tissue through quantification of their non-invasive in-vivo measurements of the viscoelastic mechanical properties. Studies utilizing MRE have also quantified changes due to a variety of factors, including development, aging and pathology. However, MRE investigations of fibrous tissues so far have provided incomplete depictions of the mechanical response in these tissue. Specifically, MRE studies investigating WM have used isotropic material models, limiting the structural information acquired during investigations of pathology and other methods of tissue degradation. Further insight into this tissue response through MRE requires an anisotropic method to quantify fibrous WM tissue, and studies have shown that skeletal muscle requires such a method. Recent studies into skeletal muscle with MRE have investigated the effects of isotropic loading with an isotropic material model and muscle lengthening with a pure shear anisotropic model. For a more complete representation of muscle function, we will quantify both passive and active muscle tension using the NITI material model.

Chapter 3

MULTI-EXCITATION MR ELASTOGRAPHY OF THE BRAIN: WAVE PROPAGATION IN ANISOTROPIC WHITE MATTER

This work presented in this chapter is adapted from Smith, et al. *JBME* (2020); 142(7); 51-59

3.1 Introduction

Imaging methods for noninvasively characterizing the microstructural health and integrity of white matter make up an important area of research for understanding various neuropathologies. These include traumatic brain injury, which often involves diffuse axonal injury caused by shearing of white matter due to linear or rotational accelerations of the head. In addition to common metrics of damage or degeneration of white matter tracts, most notably from diffusion magnetic resonance imaging (MRI) [152,174–176], mechanical properties of the brain measured with magnetic resonance elastography (MRE) [5,6,177–179] also appear sensitive to white matter tissue health. Previous work has shown that MRE can detect mechanical alterations in several neurological diseases including multiple sclerosis [180–182], Alzheimer's disease [183,184], and Parkinson's disease [185], and animal studies have demonstrated correlations between these properties with tissue microstructure such as axonal myelination [186,187]. However, most MRE studies use methods that assume the brain is mechanically isotropic [15,163,178], though the fibrous nature of white matter, comprising bundles of aligned axons, gives rise to anisotropic, directionally-dependent mechanical properties [188–191]. As such, anisotropic MRE methods are

likely needed to improve accuracy, sensitivity, and reliability of white matter mechanical property measurements.

Several anisotropic MRE analysis methods have been proposed, which generally vary in the underlying anisotropic material model and thus the number of parameters to be estimated. One anisotropic model used in MRE considers white matter as an incompressible, transversely isotropic (ITI) material with both shear and tensile anisotropy [192–194]. The three parameters of this model can be estimated through the speed of waves propagating in different directions relative to the fiber direction, which can be separated into “slow” and “fast” components based on their propagation and polarization [168]. Two separate methods have been proposed to estimate these parameters from MRE data: one based on filtering data based on the presence of slow or fast waves and a separate method using displacements at multiple frequencies [169]. The three-parameter ITI model provides a minimal model to accurately describe the behavior of white matter in a small number of parameters to be estimated. Additional anisotropic MRE methods include a two-parameter model that includes only shear anisotropy, which has been used to characterize breast tissue [165] and skeletal muscle [166], and a nine-parameter model that does not assume near-incompressibility of tissue [167], which has been used to examine white matter tracts [195].

These anisotropic MRE methods all vary in the complexity of their material model and details of their inversion algorithm, however, they all depend on having sufficient displacement data to estimate parameters. In general, there must be sufficient deformation in multiple directions to calculate the direction-dependent mechanical behavior of white matter [167]. Tweten et al. 2017 [196] described

requirements for accurate estimation of the three parameters of the ITI model that include having slow and fast waves present in multiple propagation directions. To ensure that these requirements are met for anisotropic MRE of white matter, we propose to use multi-excitation MRE to capture distinct displacement fields [173]. Anderson et al. 2016 [173] first used multi-excitation MRE in the human brain and observed differences in recovered properties up to approximately 25% in several white matter tracts, which is likely due to differences in wave propagation arising from excitation location, making this a promising approach for use with anisotropic inversion.

The primary objective of this paper is to measure wave propagation in the brain from multi-excitation MRE to assess whether data requirements for anisotropic property estimation in white matter are met. By directionally filtering the MRE displacement data, we isolate distinct, independent propagating shear waves. We then identify the dominant (primary) and secondary directions of wave propagation, based on relative amplitudes of filtered components. We classify voxels in white matter based on whether they meet minimum data requirements and show that multi-excitation MRE results in more voxels with sufficient displacement information. Finally, we demonstrate that combining wave information from multiple excitations allows us to estimate the three parameters of the ITI model.

3.2 Methods

3.2.1 Slow and Fast Wave Propagation in ITI Materials

The three independent material parameters that determine the behavior of ITI materials are substrate shear modulus, μ, shear anisotropy, ϕ, and tensile anisotropy, ζ,

which are based upon the shear modulus and tensile modulus of the material in two directions: parallel (μ_1 and E_1) and perpendicular (μ_2 and E_2) to the fibers. These parameters are described by Eqs. 5-7:

$$\mu = \mu_2 \tag{5}$$

$$\phi = \frac{\mu_1}{\mu_2} - 1 \tag{6}$$

$$\zeta = \frac{E_1}{E_2} - 1 \tag{7}$$

In an ITI material, shear waves with a given propagation direction, $\widehat{N}$, can be either "slow" (transverse) or "fast" (quasi-transverse) waves, which have separate polarization directions. These components are determined by $\widehat{N}$ relative to the fiber direction, $\hat{A}$, and the angle between them, $\theta = \cos^{-1}\left(\widehat{N} \cdot \hat{A}\right)$. The polarization direction of the slow wave, $\widehat{m}_s$, is perpendicular to $\widehat{N}$ and $\hat{A}$ (Eq. 8), while the polarization of the fast wave, $\widehat{m}_f$, is perpendicular to $\widehat{N}$ and $\widehat{m}_s$ (Eq. 9):

$$\widehat{m}_s = \frac{\widehat{N} \times \hat{A}}{\left|\widehat{N} \times \hat{A}\right|} \tag{8}$$

$$\widehat{m}_f = \widehat{N} \times \widehat{m}_s \tag{9}$$

The slow and fast wave speeds, $c_s$and c_f, are determined from the three material parameters and the angle of propagation relative to fiber direction, θ. The slow wave speed depends on the shear modulus, μ, material density, ρ, and shear

anisotropy, ϕ (Eq. 10), while the fast wave speed also depends on tensile anisotropy, ζ (Eq. 11):

$$c_s^2 = \frac{\mu}{\rho}(1 + \phi \cos^2 \theta) \tag{10}$$

$$c_f^2 = \frac{\mu}{\rho}(1 + \phi \cos^2 2\theta + \zeta \sin^2 2\theta) \tag{11}$$

MRE is potentially well-suited to quantify the three anisotropic material parameters, as wave speed, propagation direction, and fiber direction are obtainable through MRE and MRI (i.e. using diffusion tensor imaging, DTI). However, solving for these parameters requires sufficient displacement data, as described by Tweten et al. [168]. Specifically, there should be (1) multiple slow and fast waves in multiple directions and (2) each wave amplitude must have sufficient signal, i.e. at least 20% of the total original amplitude. Voxels with displacement data that meet these criteria should provide sufficient information for estimating the anisotropic parameters.

3.2.2 Data Acquisition

Four healthy subjects (3/1 M/F; 22-32 years old) provided informed, written consent and participated in the study approved by our Institutional Review Board. Each participant was scanned using a Siemens 3T Prisma MRI scanner with 20-channel head coil. Vibrations at 50 Hz were generated by an active pneumatic driver (Resoundant, Inc., Rochester, MN) and delivered to the head with two passive drivers: a pillow-driver placed behind the head for anterior-posterior (AP) excitation, and a paddle-driver placed against the temple for left-right (LR) excitation, as shown in **Figure 3.1**. Separate MRE scans were acquired for AP and LR excitations. The

acquisition employed an echoplanar-imaging (EPI) sequence with the following parameters: 3 x 3 x 3 mm^3 isotropic voxels; field-of-view = 240 x 240 mm^2; 48 slices; repetition time (TR)/echo time (TE) = 6720/65 ms. Auxiliary scans included DTI with resolution and field-of-view matched to MRE to estimate white matter fiber direction and T1-weighted anatomical image at 0.9 mm^3 isotropic resolution to localize white matter tracts. DTI scan parameters included: TR/TE = 4800/60 ms; b = 1000 s/mm^2; 30 non-colinear direction. T1-weighted anatomical scan parameters included: field-of-view = 256 x 256 mm^2; slices = 176; TR/TE/inversion time (TI) = 2080/4.45/1050 ms.

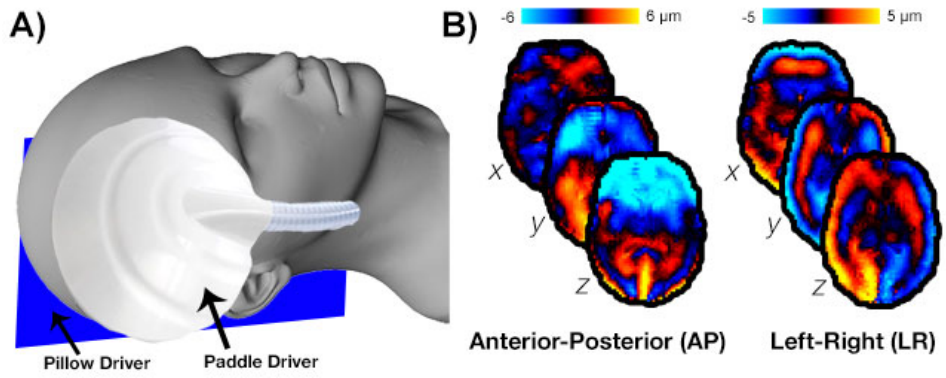

Figure 3.1: Overview of multi-excitation MRE. **(A)** Positioning of pillow driver for AP excitation and paddle driver for LR excitation. **(B)** Representative wave fields from AP and LR excitations, shown as their x, y, and z components.

3.2.3 Individual Wave Identification

We directionally-filtered [197] each MRE displacement field to determine dominant directions of wave propagation [198,199]. Each wave field was directionally filtered in 300 directions across the surface of a sphere, with a spherical bandpass filter (4.2 to 166.7 m^{-1}) applied in all directions. In each voxel, the primary wave direction was determined as the filter direction in which the filtered field retained the highest

energy. We also identified a secondary wave direction as the filter direction which retained the next greatest energy in the filtered field, and that differed by at least 30° from the primary direction. From this analysis, we identified primary ($\widehat{N}_1$) and secondary ($\widehat{N}_2$) wave propagation directions at every voxel for both AP and LR excitations.

We then isolated the slow and fast shear waves in each of the primary and secondary directions. We determined the polarization directions of each slow and fast wave based on propagation direction (primary and secondary, n = 1,2) and fiber direction (Eqs. 12 and 13). Slow and fast waves were then reconstructed by projecting the directionally filtered wave field, $\vec{U}_{filt,n}$, onto the polarization direction (Eqs. 14 and 15):

$$\widehat{m}_{s,n} = \frac{\widehat{N}_n \times \hat{A}}{\left|\widehat{N}_n \times \hat{A}\right|} \tag{12}$$

$$\widehat{m}_{f,n} = \widehat{N}_n \times \widehat{m}_{s,n} \tag{13}$$

$$\vec{U}_{s,n} = \left[\vec{U}_{filt,n} \cdot \widehat{m}_{s,n}\right] \widehat{m}_{s,n} \tag{14}$$

$$\vec{U}_{f,n} = \left[\vec{U}_{filt,n} \cdot \widehat{m}_{f,n}\right] \widehat{m}_{f,n} \tag{15}$$

Using the analysis above, there are eight possible wave fields (AP/LR, primary/secondary, slow/fast) that can be used to meet the criteria for successful anisotropic inversion. We determined if a voxel had sufficient data to meet these criteria if there were at least two slow waves and two fast waves with amplitude greater than 20% of the original motion amplitude and with propagation directions different by at least 15° [196]. We considered the number of voxels that met these

criteria using both single excitations (AP or LR) and multiple excitations together (AP+LR).

3.2.4 Anisotropic Parameter Estimation

In order to demonstrate that individual waves from multi-excitation MRE can be used to estimate anisotropic material parameters, we estimated μ, ϕ, and ζ using an overdetermined system of equations (Eq. 16). Specifically, we considered the relationships for both slow and fast wave speeds (Eqs. 10 and 11) separately for each of the primary and secondary waves included in each excitation. This resulted in a system of eight equations comprising two polarizations (slow and fast) for each of two wave propagation directions (primary and secondary) for each of two excitations (AP and LR). Since the material parameters μ, ϕ, and ζ are the same in each case, this system of equations can be solved to generate property estimates.

$$\begin{bmatrix} c_{s,1,AP}^2 \\ c_{s,2,AP}^2 \\ c_{s,1,LR}^2 \\ c_{s,2,LR}^2 \\ c_{f,1,AP}^2 \\ c_{f,2,AP}^2 \\ c_{f,1,LR}^2 \\ c_{f,2,LR}^2 \end{bmatrix} = \begin{bmatrix} 1 & \cos^2\theta_{s,1,AP} & 0 \\ 1 & \cos^2\theta_{s,2,AP} & 0 \\ 1 & \cos^2\theta_{s,1,LR} & 0 \\ 1 & \cos^2\theta_{s,2,LR} & 0 \\ 1 & \cos^2\theta_{f,1,AP} & \sin^2\theta_{f,1,AP} \\ 1 & \cos^2\theta_{f,2,AP} & \sin^2\theta_{f,2,AP} \\ 1 & \cos^2\theta_{f,1,LR} & \sin^2\theta_{f,1,LR} \\ 1 & \cos^2\theta_{f,2,LR} & \sin^2\theta_{f,2,LR} \end{bmatrix} * \begin{bmatrix} \mu \\ \mu\phi \\ \mu\zeta \end{bmatrix} \tag{16}$$

Solving this system of equations requires estimates of the wave speed for each individual wave field, which we perform for each voxel. First, for a given voxel – i.e. (x_0, y_0, z_0) – we directionally-filtered the wave field from AP or LR excitation in the direction of the primary or secondary wave at that voxel (Figure 3.2A), and then

projected onto the slow or fast polarization direction to create an isolated wave field (Figure 3.2B) – e.g. $\vec{U}_{s,1,AP}(x,y,z)$. This wave field is input to the local direct inversion (LDI) algorithm [200] to estimate the wave speed – e.g. $c_{s,1,AP}(x,y,z)$ – from which we extract the value only at the voxel of interest (x_0, y_0, z_0). This process is repeated for each voxel and for each of the additional wave fields, as seen in Figure 3.2C. Each of the angles, θ, describing the relationship between propagation direction and fiber angle were computed for each individual primary and secondary wave by $\theta = \cos^{-1}(\hat{N} \cdot \hat{A})$. This results in a system of equations (Eq. 12) at each voxel. We use a least squares solution of this system at each voxel, including only the isolated wave fields that meet the amplitude threshold (see above), to estimate μ, ϕ, and ζ at each voxel. We constrained values of μ to be positive between 0 and 8 kPa and left the other parameters unconstrained in the solution.

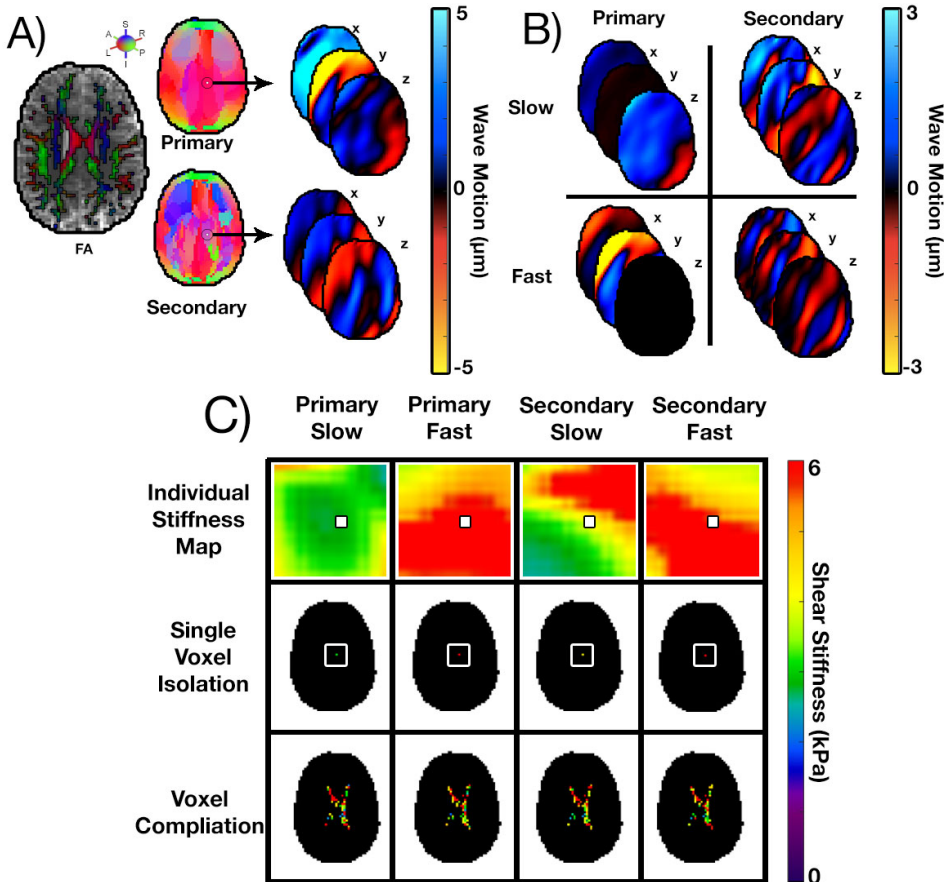

Figure 3.2: The approach used to determine voxelwise stiffness estimates from individual wave fields. **(A)** Directional filters, based on the primary and secondary directions of a specific voxel, are applied to the wave field over the entire brain, providing two (primary and secondary) filtered fields. **(B)** Slow and fast shear waves in those primary and secondary directions. **(C)** Isolated section, outlined by the white box, of the stiffness map estimated for each of the slow and fast waves, at every voxel, and the stiffness map created by compiling results from individual inversions.

3.2.5 Analysis

We analyzed wave propagation throughout the brain, in white matter, and in an individual white matter tract – the body of the corpus callosum, which was chosen as it has highly aligned fibers and thus is likely to behave like an ITI material. The white matter mask was created using the FMRIB Automated Segmentation Tool (FAST) in

the FMRIB Software Library (FSL) [201,202] to segment the T1-weighted MPRAGE, which was then registered to the MRE data. Only voxels with fractional anisotropy (FA) > 0.25 from DTI were included. A white matter atlas in standard-space [203,204] was registered to the MRE data using the FMRIB Linear Image Registration Tool (FLIRT) in FSL [205] to create a mask of the corpus callosum body.

3.3 Results

3.3.1 Shear Wave Differentiation

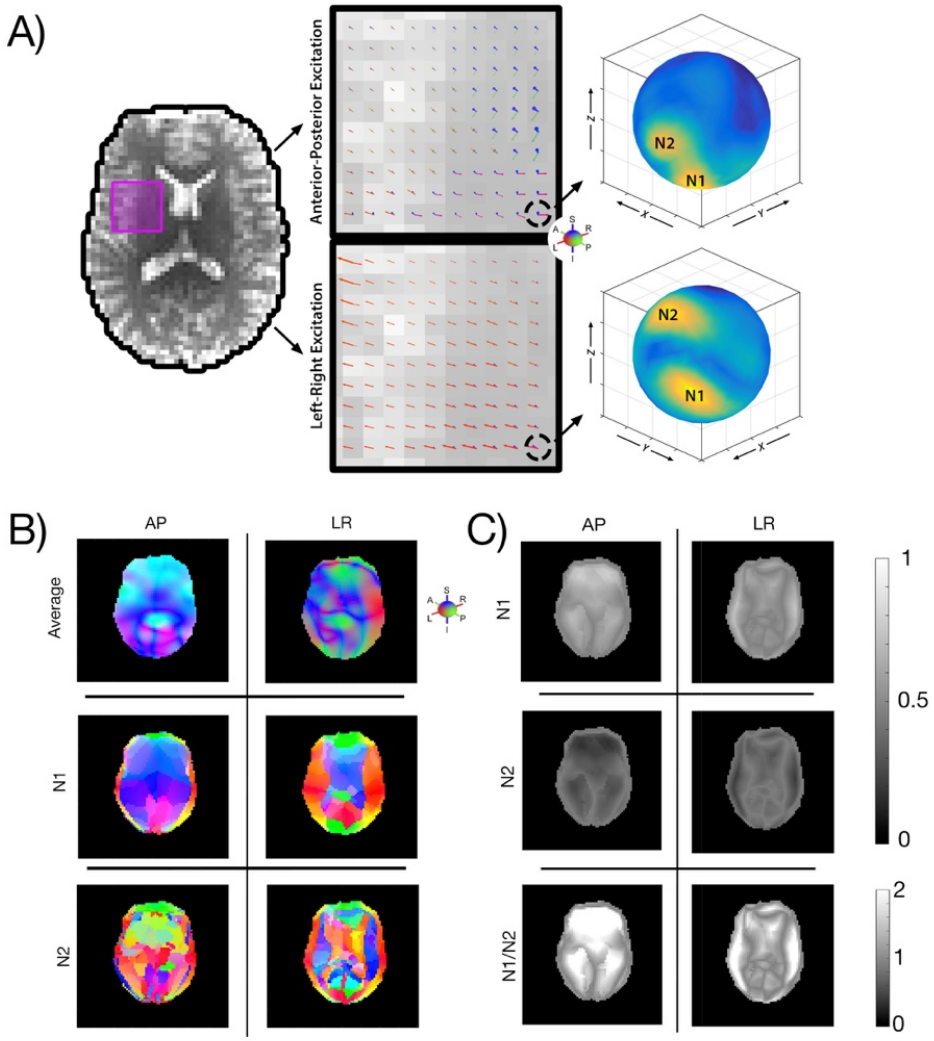

Figure 3.3: Illustration of individual wave propagation directions. **(A)** Primary ($\widehat{N}_1$) and secondary ($\widehat{N}_2$) wave propagation directions for both AP and LR excitations within a single voxel. Note the spheres have different orientations between the two excitations. **(B)** Average wave direction throughout the brain along with primary and secondary wave directions for both AP and LR excitations. **(C)** Amplitudes of the primary and secondary waves and the ratio of the two for both AP and LR excitations.

Figure 3.3 depicts the identification of individual primary and secondary wave directions at each voxel throughout the brain. We plot the energy of the directionally filtered displacement field on a sphere; the maxima on the surface ("hot spots"), correspond to the dominant (primary and secondary) propagation directions. The two spheres show clearly that the AP and LR excitations result in different wave propagation directions at a single voxel. Figure 3.3B shows that the primary and secondary wave directions differ across the brain. Additionally, they are compared with the "average" propagation which is the weighted average of directions based on energy in each filter direction, which has been used previously to describe propagation direction [198]. Figure 3.3C compares the amplitudes of the primary and secondary waves, as well as the ratio between the two. Almost every voxel in the brain has a primary and secondary wave of at least 20% of the total wave amplitude: 98.8% of voxels from AP excitation and 99.2% of voxels from LR excitation had two waves above this threshold. Sharp discontinuities in wave direction are notable where two waves intersect and change their identification from primary to secondary, and vice versa. These regions are also reflected in the amplitude measurements where the two waves are of nearly identical amplitude.

3.3.2 Slow and Fast Shear Wave Identification

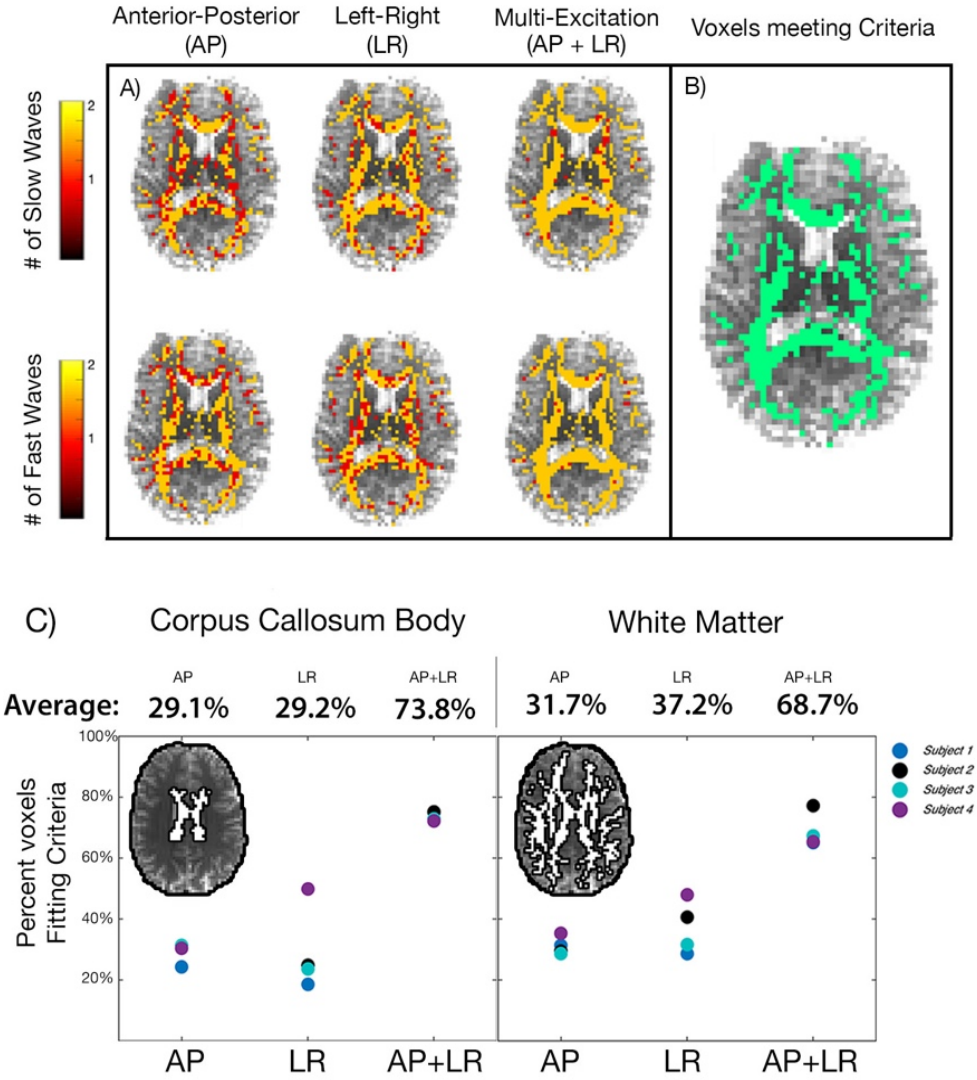

Figure 3.4: Overview of displacement data sufficient for anisotropic inversion in white matter. **(A)** Number of slow and fast waves in each voxel for single excitations (AP or LR) and multiple excitations (AP+LR), and **(B)** white matter voxels with data meeting the minimum inversion criteria from both excitations. **(C)** Percentage of voxels across white matter and in the corpus callosum body, an individual white matter tract, that fit the criteria for each excitation.

Slow and fast waves were isolated in each of the individual primary and secondary wave directions. Figure 3.4 shows which voxels fit the criteria for anisotropic inversion based on the slow and fast waves from single (AP or LR) and multiple (AP+LR) excitations. Combining both excitations results in a substantially greater number of voxels that meet the minimum criteria compared to single excitations (Figure 3.4C). Overall, 68.7% of white matter voxels meet the criteria from multiple excitations, and an even higher 73.8% meet the criteria in the corpus callosum body, while many fewer voxels met these criteria for single excitations (29-37% in each region for both AP and LR).

3.3.3 Least Squares Parameter Estimation

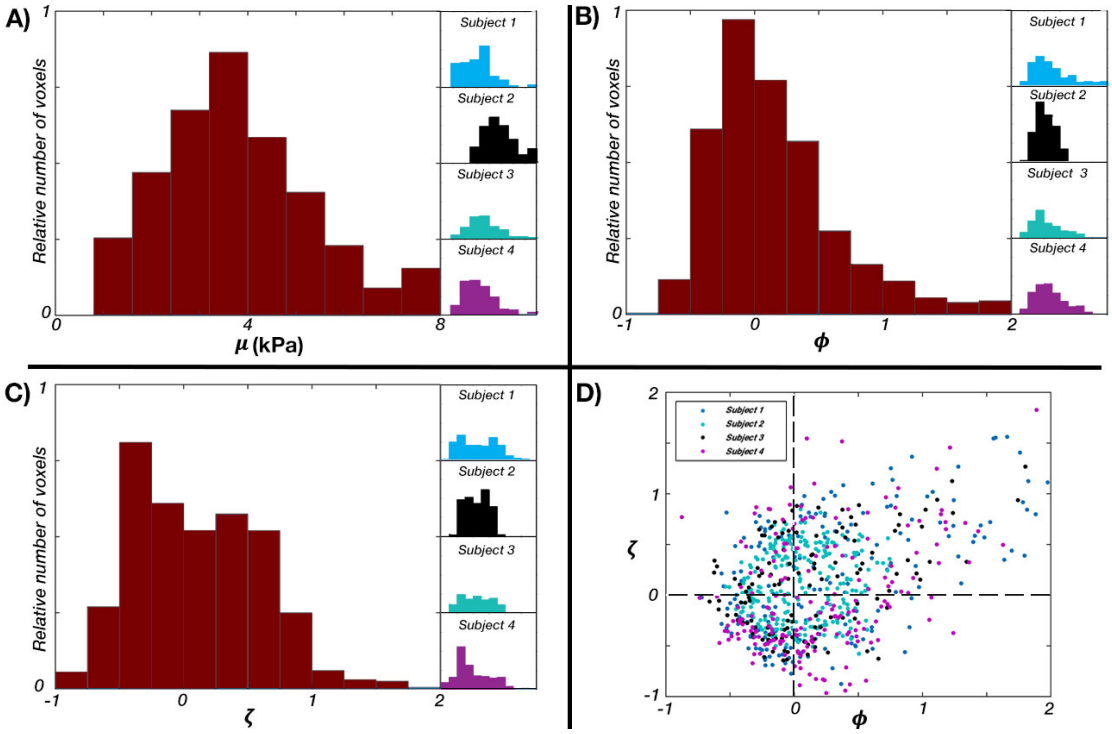

Figure 3.5: Distribution of anisotropic parameters **(A)** substrate shear modulus, μ, **(B)** shear anisotropy, ϕ, and **(C)** tensile anisotropy, ζ, in the corpus callosum body for each subject and all subjects pooled together. **(D)** Relationship between ϕ and ζ in each voxel across all subjects ($r = 0.38$).

Using each of the slow and fast waves for each voxel that met the criteria, we solved the system of equations and estimated the three anisotropic parameters, μ, ϕ, and ζ, in the corpus callosum body. Figure 3.5 shows the distributions of parameter values from each subject and all subjects pooled together. We found the mean μ = 3.78 kPa (95% CI: 3.67-3.90 kPa), mean ϕ = 0.151 (95% CI: 0.116-0.186), and mean

ζ = 0.099 (95% CI: 0.063-0.134). Figure 3.5D illustrates the relationship between ϕ and ζ in each voxel, showing a weak positive correlation between the two (r = 0.38).

3.4 Discussion

In this paper we examined the use of multi-excitation MRE to provide sufficient displacement data to estimate anisotropic mechanical parameters of the brain in vivo. This study builds on, and quantitatively extends, our previous observation that separate excitation directions in MRE give rise to different property estimates in white matter [173], which are presumably due to different propagation and polarization directions from each excitation.

By directionally filtering the MRE displacement fields in the brain, we were able to identify multiple shear waves with different propagation directions in most voxels. This is the first study to demonstrate the presence of at least two (primary and secondary) directions of wave propagation throughout the brain. In brain MRE, shear deformations are generated from the skull [198], and thus the existence of many different source points likely gives rise to the multiple waves. Shear waves are also likely to originate from the falx and tentorium [198], which are stiff membranes between the cerebral hemispheres and the cerebrum and cerebellum, and perhaps even from the brainstem, which can move independently of the brain [206].

The two different excitation methods, AP and LR, lead to motion patterns that are distinct but share some common features. AP-excited primary wave propagation is predominantly in the z-direction (superior-inferior), while LR motion excites primary wave propagation predominantly in the x-direction (left-right). In both cases there are sharp discontinuities in propagation direction away from the skull where the primary and secondary waves cross (and thus swap their identification). At these crossover

regions, two waves exist with similar amplitude. The two excitations result in greater differences in secondary wave direction at the center of the brain where the propagating waves excited by contact with the cranium have converged and mix with waves from internal sources. These waves also dampen and lose amplitude causing the estimation of secondary waves in the center of the brain to be more affected by noise. In future work, these waves might be tracked individually back to their source points to better identify and characterize propagating waves, and potentially identify additional waves that may be useful in improving anisotropic MRE inversion.

By using multiple excitations, more propagation directions are generated, which increases the number of voxels that meet the minimum criteria for anisotropic inversion.

Single excitations (AP or LR) led to a much lower percentage of voxels that met the criteria as compared to the combination of multiple excitations (AP+LR). Thus, using multiple excitations likely increases the ability to determine the anisotropic properties of white matter at the individual tract or voxel level. However, two excitations did not provide sufficient data in every white matter voxel or across an entire white matter tract, and thus additional excitations providing unique displacement data may be required to completely map anisotropic tissue parameters at the voxel level throughout the brain. To combat the commensurate increase in scan time necessary for additional excitations, accelerated data collection may be required, perhaps through simultaneous acquisition of MRE displacement directions [207–209].

We demonstrated that multiple wave fields may be used to estimate anisotropic parameters in white matter by determining the wave speeds of individual slow and fast waves. In the corpus callosum body, we found the mean shear stiffness μ of 3.78 kPa.

This estimate is slightly higher than two other recent estimates that used a different inversion technique without considering anisotropy [173,210], which may account for differences we observe in this work. We found mean shear anisotropy ϕ of 0.151, indicating that the shear modulus is 15.1% higher for shear in planes parallel to the fiber direction compared to planes normal to the fibers. We also found mean tensile anisotropy ζ of 0.099, indicating that the elastic modulus is 9.9% higher parallel to the fiber direction. The recovered ϕ and ζ values in each voxel were positively correlated indicating that the degree of shear and tensile anisotropy increases together, as we may expect for fibrous material like brain white matter.

Our estimate of ϕ is smaller than a similar report of ϕ in porcine white matter between 0.27-0.34 as reported by Schmidt, et al. [192]. However, both ϕ and ζ are more similar to equivalent parameters in the in vivo human corticospinal tract of ϕ = 0.14 and ζ = 0.06 as reported by Romano, et al. [167]. The true in vivo parameters are potentially higher, indicating greater anisotropy, based on ex vivo mechanical testing [188], and the incomplete contrast recovery in our preliminary estimates is likely due to methodological factors. For instance, the resolution used in this study is lower than used in previous studies of white matter tracts [173,210,211], which likely impacts the accuracy and reliability of property maps in these small regions [11,212]. Ideally, future investigations should adopt higher resolution imaging methods to better resolve individual white matter tracts.

Additionally, while this initial attempt to estimate anisotropic parameters showed promising results, we also acknowledge several limitations. First, we used a direct inversion method to process individual wave fields. Direct inversion methods assume local tissue homogeneity [178] and thus introduce uncertainty at tissue

boundaries, which is exacerbated by lower spatial resolution. Inversion methods specifically designed to model white matter anisotropy, such as the waveguide MRE method [167], may be potentially combined with multi-excitation MRE to provide more robust parameter estimates. Additionally, the nonlinear inversion (NLI) method [163,213], which explicitly models tissue as a heterogeneous material and has been applied successfully to estimate local brain properties [11,210], may improve accuracy of measures in specific white matter tracts if formulated to include anisotropy. Advanced inversion methods will also allow us to incorporate data from multiple frequencies and model viscoelastic behavior of the anisotropic white matter [169,214]. More robust methods for LR excitation or additional excitations may improve feasibility and comfort in participants. Yin et al. 2018 [215] previously used multiple active pneumatic drivers, in addition to multiple passive drivers arrayed around the head, in order to excite the brain in several directions; though the use of multiple active drivers can potentially lead to prohibitive equipment costs. Finally, future studies are needed to evaluate the consistency and reliability of parameter estimates through phantom studies, repeated measurements in healthy brains [10,11,210], and studies with a larger number of subjects to determine sensitivity to pathology.

3.5 Conclusions

This study is the first to investigate the use of multi-excitation MRE to estimate anisotropic parameters (μ, ϕ, and ζ) of an ITI material model of white matter. We found that each excitation results in distinct shear waves, in at least two propagation directions, and both “slow” (pure shear) and “fast” (quasi-shear) polarizations. Thus, by combining AP and LR excitations, shear wave data from most voxels in white matter was sufficient for anisotropic inversion. We demonstrated that

by isolating individual waves and calculating their wave speeds we could estimate the three anisotropic parameters and recover values consistent with previous reports in white matter. Overall, these results suggest that multi-excitation MRE is a promising technique for providing data for anisotropic inversion and that this approach can be used in future work to more accurately and reliably map the mechanical properties of brain white matter in vivo.

Chapter 4

ANISOTROPIC ESTIMATION OF WHITE MATTER USING MULTIEXCITATION MR ELASTOGRAPHY AND A TRANSVERSELY ISOTROPIC NONLINEAR INVERSION ALGORITHM

4.1 Introduction

Imaging methods which are sensitive to the health and structural integrity of white matter (WM) tissue are important for characterizing many neuropathological conditions, including multiple sclerosis [181] and traumatic brain injury [23,174]. Magnetic resonance elastography (MRE) has shown promise in assessing changes to the microstructural integrity of brain tissue through quantification of its viscoelastic mechanical properties [6,16]. Past MRE studies have found non-specific softening of brain tissue in multiple sclerosis [180–182], Alzheimer's disease [183,184], and Parkinson's disease [185], indicating a loss of structural integrity in neurodegeneration. However, softening is also reported in normal aging [160,216,217], which limits MRE as a diagnostic imaging modality. In vivo brain MRE studies often assume brain parenchyma is mechanically isotropic in order to simplify the inversion algorithm and property estimation, even though WM tracts exhibit direction-dependent mechanical properties due to their bundles of aligned axons, and thus, isotropic MRE methods can introduce uncertainty in WM regions from model-data mismatch [173]. Therefore, anisotropic inversion methods are likely to be necessary to estimate the properties of WM tracts accurately and recover material parameters sufficient to discriminate normal aging processes from

neurodegenerative diseases. Accordingly, the spectrum of properties estimated in anisotropic MRE models may separate and distinguish the wide range of conditions which appear to cause the tissue softening estimated with isotropic approaches.

Anisotropic MRE inversion methods reported to date vary their underlying anisotropic material models and the corresponding number of descriptive material parameters [165–167,218–220]. A three-parameter material model that describes white matter as a nearly incompressible, transversely isotropic (NITI) material within the space of a single voxel involves parameters that incorporate both shear and tensile anisotropy, or the ratios of shear modulus and Young's modulus parallel and perpendicular to the fiber direction [168,188,194]. It balances accurate modeling of the mechanical behavior of materials with aligned fiber tracts (i.e. WM) [191], with minimal increase in the number of property parameters required for estimation from MRE displacement maps. However, estimating these parameters requires displacement data from mechanical waves having different propagation and polarization directions [196], which is difficult to achieve with sufficient SNR from a single MRE scan. To address this, we have previously implemented multi-excitation MRE in which two drivers, placed in perpendicular orientations, produce mechanical waves in sequential acquisitions sufficient to generate the wave pattern differences necessary to capture the directionally-dependent material properties of WM [173,221].

Estimating the spatial distribution of anisotropic mechanical properties accurately in WM tracts requires an inversion algorithm that accounts for material heterogeneity. WM is strongly heterogeneous comprising large tracts that differ in mechanical properties [210] as well as fiber direction. McGarry, et al. [222] developed a transversely isotropic nonlinear inversion (TI-NLI) to recover heterogenous

anisotropic parameters, and demonstrated accurate estimation of NITI anisotropic property parameter fields when combined with multi-excitation MRE data [223]. Incorporating both anisotropy and heterogeneity in the mechanical model during inversion reduces model-data mismatch and improves property estimates in regions containing WM tracts. Johnson, et al. [210] estimated properties of WM tracts with MRE, though that study utilized an isotropic model and the reported parameter values do not capture direction-dependent material behavior. Local properties have also been reported in cerebral lobes [10] and subcortical gray matter structures [11], which have shown regional sensitivity to aging [156,224], neurological disease [225–227], and cognitive function [228,229]. Understanding the anisotropic properties of WM tracts may further improve the utility of MRE in these applications.

In this study, we measured the anisotropic mechanical properties of individual WM tracts in vivo using multi-excitation MRE with TI-NLI. To collect the multi-excitation data required, we used a custom designed passive driver combined with the standard pillow driver common in brain MRE. We examined the repeatability of anisotropic parameter estimates from MRE data collected with this custom multi-excitation driver coupled with TI-NLI. We estimated the average anisotropic material parameters of gray and white matter in a sample of healthy, young adults, and in individual white matter tracts, such as the corpus callosum and the corona radiata. We further analyzed the heterogeneity in material properties between individual regions of the corpus callosum to examine potential relationships with underlying axonal microstructure.

4.2 Methods

Seventeen healthy participants (7/10 M/F; 22-30 years old) provided informed, written consent to participate in the study approved by our Institutional Review Board. Each participant completed a scanning session using a Siemens 3T Prisma MRI scanner with a 20-channel head coil. One subject completed the protocol ten times to quantify repeatability of the outcome measures.

4.2.1 Data Acquisition

The protocol included multi-excitation MRE scans with excitation in both left-right (LR) and anterior-posterior (AP) directions. We designed a secondary actuator to generate LR actuation [230,231] with the goal of improved reliability and stability of applied vibrations relative to previous approaches, for example as described in Anderson, et al. [173] and Smith, et al. [221]. The custom LR actuator includes two flexible bottles attached to the head coil using custom 3D printed pieces, shown in Figure 1. These bottles contacted the sides of the head near the temples – one was connected to an active pneumatic driver and the second acted as a support; both were adjustable for different head sizes. In multi-excitation MRE, vibrations are applied with the LR actuator as well as the typical pillow driver for AP excitation via an active pneumatic driver (Resoundant, Inc., Rochester, MN). All vibrations were applied at 50 Hz.

Each of the two MRE acquisitions with either LR or AP excitation used a 3D multiband, multishot spiral sequence [232] to encode full vector displacement fields in the brain. Imaging parameters included: 2.0 x 2.0 x 2.0 mm^3 isotropic resolution; field-of-view = 240 x 240 mm^2; 64 slices; repetition time (TR)/echo time (TE) = 2240/76 ms.

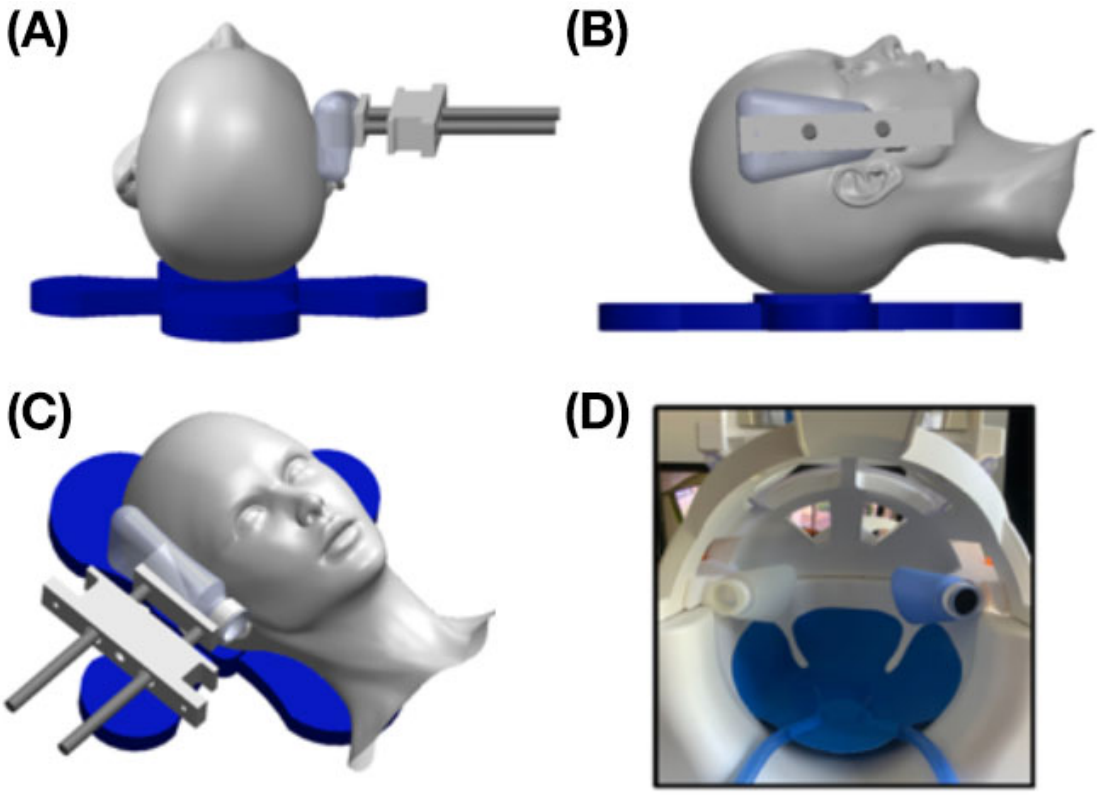

Figure 4.1: Schematic of the multi-excitation actuator design including pillow driver for anterior-posterior excitation and custom 3D printed left-right actuator, as well as a picture of the drivers inside the 20 channel head coil. The design allows the actuator to rest against the side of the subject's head and is adjustable for different head sizes.

Additional scans in the MRI protocol included diffusion tensor imaging (DTI) acquisitions to estimate fiber direction and a T1-weighted anatomical image to localize WM tracts. The DTI acquisitions used a simultaneous multislice EPI sequence with the following parameters: field-of-view = 240 x 210 mm^2; 1.5 x 1.5 x 1.5 mm^2 resolution; 92 slices; TR/TE = 3520/95.2 ms; b-values = 1500 & 3000 s/mm^2; directions = 128. The two DTI scans were acquired with opposite phase encoding direction – one in the anterior-posterior direction and the other in the posterior-anterior

direction – which were combined to correct for distortions by applying TOPUP in FSL [233]. We used FMRIB's Linear Image Registration Tool (FLIRT) [201] to register the DTI images to MRE space, and the diffusion gradient directions for each image were rotated according to this registration to correct for motion in DTI data [234]. These data were processed using the FMRIB's Diffusion Toolbox (FDT) from FMRIB's Software Library (FSL) [202] to extract fractional anisotropy (FA) and primary eigenvector (V1). T1-weighted anatomical images were acquired with an MPRAGE sequence having the following parameters: field-of-view = 256 x 256 mm^2; slices = 176; TR/TE/inversion time (TI) = 2300/2.32/900 ms; 0.9 x 0.9 x 0.9 mm^3 isotropic resolution.

4.2.2 Transversely Isotropic Nonlinear Inversion

Shear wave displacement fields were calculated by subtracting MRE phase images obtained with opposite-polarity motion encoding gradients, unwrapping phase with FSL PRELUDE, and temporally Fourier filtering to isolate the harmonic component of interest. We then used both AP and LR wave motion fields and the primary eigenvector from DTI, which is assumed to be the fiber direction defining material symmetry, to estimate a single set of anisotropic material parameters with TI-NLI, as illustrated schematically in Figure 2. The latter returns spatial maps of three NITI model parameters describing the mechanical behavior of viscoelastic, fiber-reinforced tissue: the complex-valued substrate shear modulus ($G = G_2$), real-valued shear anisotropy ($\phi = G_1/G_2 - 1$), and real-valued tensile anisotropy ($\zeta = E_1/E_2 - 1$). Here, shear modulus is denoted by G while Young's modulus is denoted by E, with subscript 1 indicating the direction of fiber orientation, or the direction normal to the plane of isotropy, while subscript 2 indicates the direction orthogonal to the fiber

within the plane of isotropy. In a coordinate system where the fiber is in the x_1 direction in standard Voigt notation, the relationship between the components of the rank 2 symmetric stress tensor, σ, and strain tensor, ϵ, is given by

$$\begin{Bmatrix} \sigma'_{11} \\ \sigma'_{22} \\ \sigma'_{33} \\ \sigma'_{12} \\ \sigma'_{23} \\ \sigma'_{13} \end{Bmatrix} = \begin{bmatrix} c_{11} & c_{12} & c_{13} & 0 & 0 & 0 \\ c_{21} & c_{22} & c_{23} & 0 & 0 & 0 \\ c_{31} & c_{32} & c_{33} & 0 & 0 & 0 \\ 0 & 0 & 0 & c_{44} & 0 & 0 \\ 0 & 0 & 0 & 0 & c_{55} & 0 \\ 0 & 0 & 0 & 0 & 0 & c_{66} \end{bmatrix} \begin{Bmatrix} \epsilon'_{11} \\ \epsilon'_{22} \\ \epsilon'_{33} \\ 2\epsilon'_{12} \\ 2\epsilon'_{23} \\ 2\epsilon'_{13} \end{Bmatrix} \tag{17}$$

The components of the elasticity matrix are expressed in Eqs. (18-23),

$$c_{11} = \kappa + \frac{4}{3}G\left(1 + \frac{4}{3}\zeta\right) \tag{18}$$

$$c_{22} = c_{33} = \kappa + \frac{4}{3}G\left(1 + \frac{1}{3}\zeta\right) \tag{19}$$

$$c_{44} = c_{66} = G(1 + \phi) \tag{20}$$

$$c_{12} = c_{13} = c_{21} = c_{31} = \kappa - \frac{2}{3}G\left(1 + \frac{4}{3}\zeta\right) \tag{21}$$

$$c_{32} = c_{23} = \kappa - \frac{2}{3}G\left(1 - \frac{2}{3}\zeta\right) \tag{22}$$

$$c_{55} = G \tag{23}$$

Here, κ represents the bulk modulus, which describes "isotropic compressibility" and is set to a large value to obtain near incompressibility. The model accommodates slow ("pure shear) and fast ("quasi-shear") shear waves, predicted and observed in transversely isotropic materials [194,235], as well as the very fast acoustic (longitudinal, or compression) wave.

TI-NLI estimates the complex-valued substrate shear modulus, $G_2 = G' + iG''$,, where G' and G'' are the storage and loss modulus, respectively. Here we report the substrate shear stiffness, $\mu = \frac{2\left(G'^2+G''^2\right)}{G'+\sqrt{G'^2+G''^2}}$ [16], which reflects the square of the wave speed in a viscoelastic material and is commonly reported in the MRE literature. In this model, with real-valued ϕ and ζ, the damping ratio is isotropic, defined by $\xi = G''/2G'$ [222].

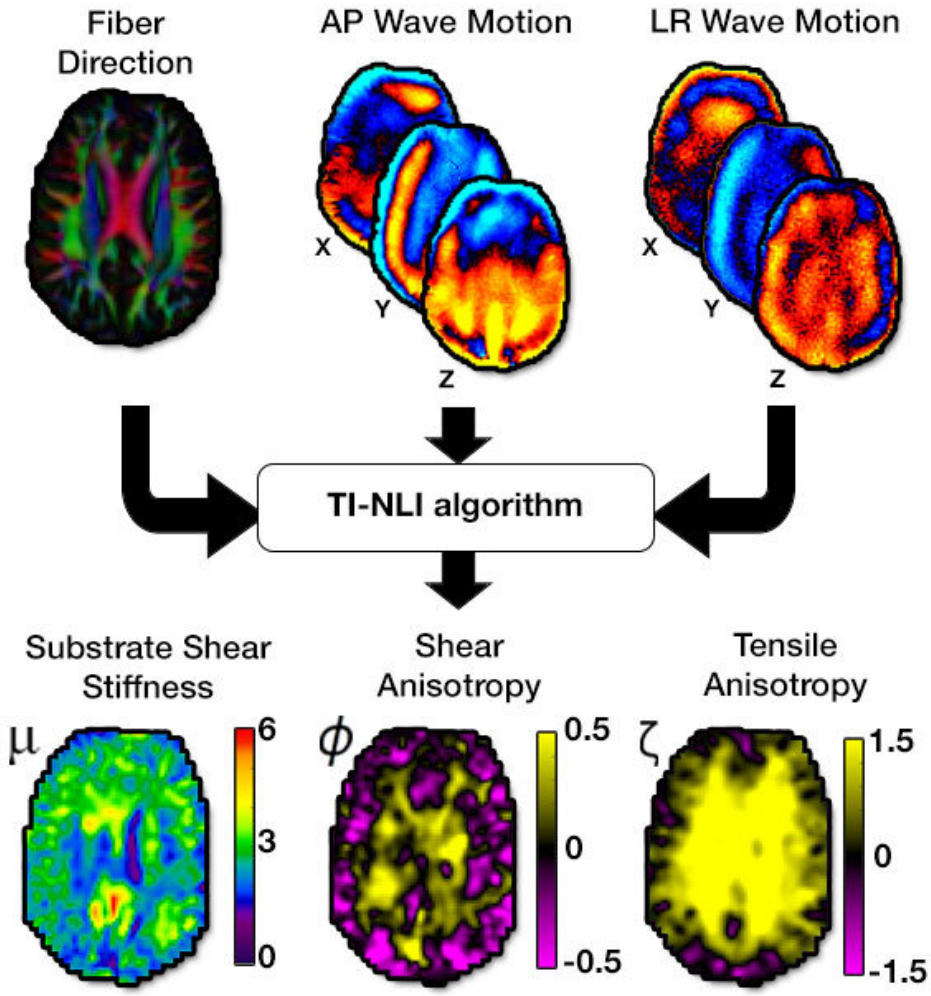

Figure 4.2: The data from MRE (AP and LR wave motion) and DTI (V1) are input into the transversely isotropic, non-linear inversion algorithm (TI-NLI) to solve for the three anisotropic parameters: substrate shear modulus, μ, shear anisotropy, ϕ, and tensile anisotropy, ζ.

4.2.3 Analysis

We determined the average anisotropic properties in gray matter (GM) and white matter (WM), as well as in several individual white matter tracts. Segmentation of GM and WM from the T1-weighted images was performed with FSL FAST (FMRIB's Automated Segmentation Tool) and registered to MRE space using FLIRT

[201]. We generated masks of individual WM tracts including the corpus callosum (CC), corona radiata (CR), superior longitudinal fasciculus (SLF), forceps major (FM1), and forceps minor (FM2) using two WM atlases in MNI space [203,204]. Each tract region was registered to MRE space using FSL FLIRT and thresholded with DTI FA values above 35% to create binary masks. Additionally, we examined the three major parts of the CC – the genu, body, and splenium – to investigate heterogeneity within an individual tract.

We examined repeatability of extracted properties via ten measurements in a single volunteer. We then compared standard deviations of μ, ϕ, and ζ between the repeated measures and the variability in the overall sample population. We determined differences in anisotropic properties between ROIs using one-way ANOVAs with post-hoc Tukey tests to determine relationships between individual pairs of tracts. Additionally, we executed paired t-tests to compare variability in each measure in a single subject relative to the entire sample. All statistical analyses were performed with JMP statistical software v.16.0

4.3 Results

4.3.1 Anisotropic Mechanical Properties of White Matter Tracts

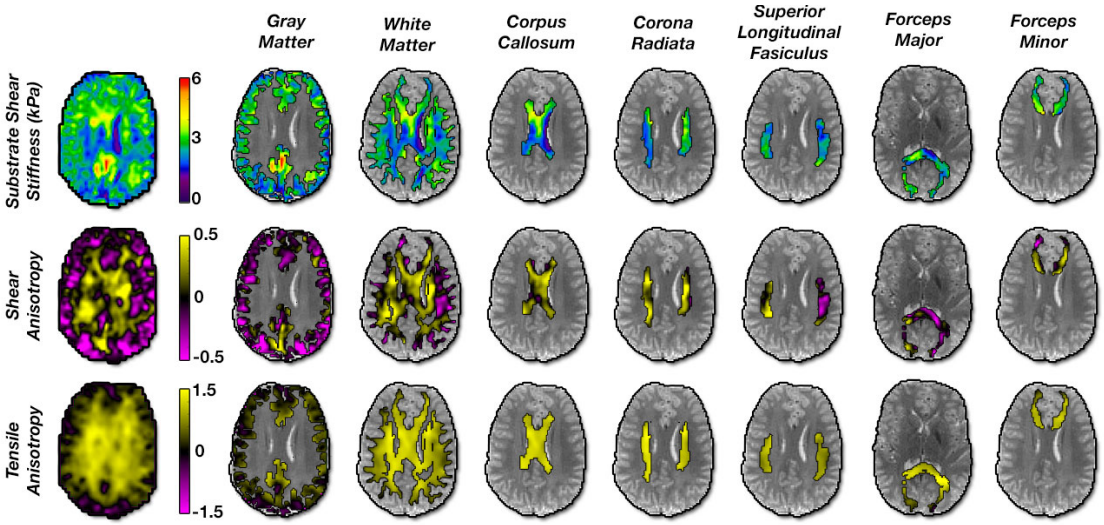

Figure 4.3 Maps of the estimated anisotropic parameters in the human brain in a representative slice for each of the ROIs used in this study: gray matter, white matter, corpus callosum, corona radiata, superior longitudinal fasciculus, forceps minor, and forceps major.

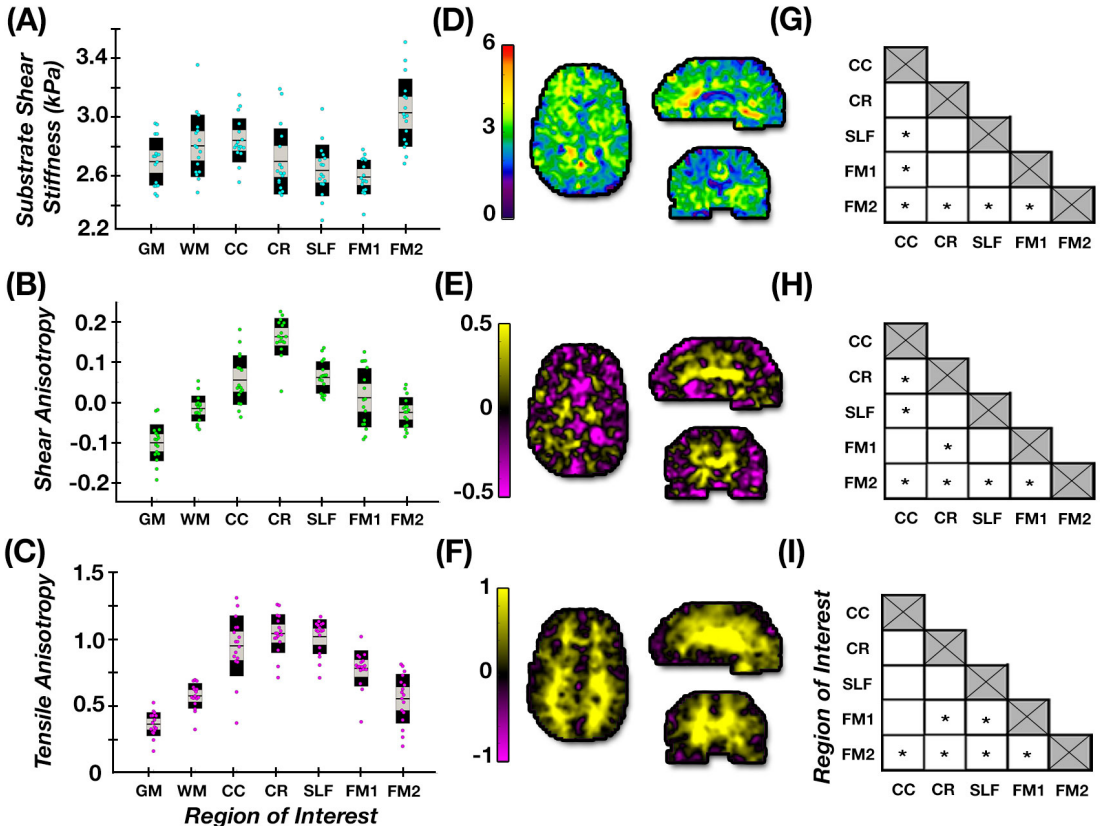

Figure 4.4: (A-C) Average parameter outcomes in healthy young adults for each ROI; (D-F) representative axial, sagittal, and coronal slices of each property; (G-I) differences between individual tracts properties with significant differences denoted by * ($p < 0.05$).

Figure 4.3 illustrates estimated anisotropic parameter – μ, ϕ, and ζ – and their distribution in the investigated ROIs: GM, WM, and the individual WM tracts of the CC, CR, SLF, and forceps minor and major. Figure 4.4 presents μ, ϕ, and ζ in our population of young adults in each of the ROIs. The overall WM region exhibited an average ϕ of - 0.016 ± 0.032 and average ζ of 0.580 ± 0.095, which were significantly greater than gray matter ($p < 0.05$), where ϕ = -0.101 ± 0.046 and ζ = 0.367 ± 0.088. The individual white matter tracts demonstrated mostly positive shear anisotropy, with

ϕ ranging from -0.026 to 0.164, and positive tensile anisotropy, with ζ ranging from 0.559 to 1.049. For both parameters, the CR exhibited the largest anisotropy parameters, while forceps minor exhibited the smallest. μ values for the individual tracts ranges from 2.57 to 3.02 kPa. Figure 4.4 also presents how each tract differs for each of the properties. Almost every tract showed a significant difference with every other tract in at least one property ($p < 0.05$), with the exception of CR and SLF. In particular, the forceps major and each of the other WM tracts shows significant differences in all properties.

Table 4.1: A comparison showing the mean and standard deviation of the three anisotropic parameters, μ, ϕ, and ζ, for each the seven ROIs across the entire population sample.

	GM	**WM**	**CC**	**CR**	**SLF**	**FM1**	**FM2**
μ *(kPa)*	2.68 ± 0.17	2.79 ± 0.22	2.83 ± 0.15	2.68 ± 0.23	2.62 ± 0.18	2.57 ± 0.12	3.02 ± 0.24
ϕ	-0.101 ± 0.046	-0.016 ± 0.032	0.056 ± 0.062	0.164 ± 0.047	0.062 ± 0.040	0.011 ± 0.074	-0.026 ± 0.038
ζ	0.367 ± 0.088	0.580 ± 0.095	0.956 ± 0.227	1.049 ± 0.144	1.025 ± 0.130	0.787 ± 0.135	0.559 ± 0.185

4.3.2 Measurement Repeatability

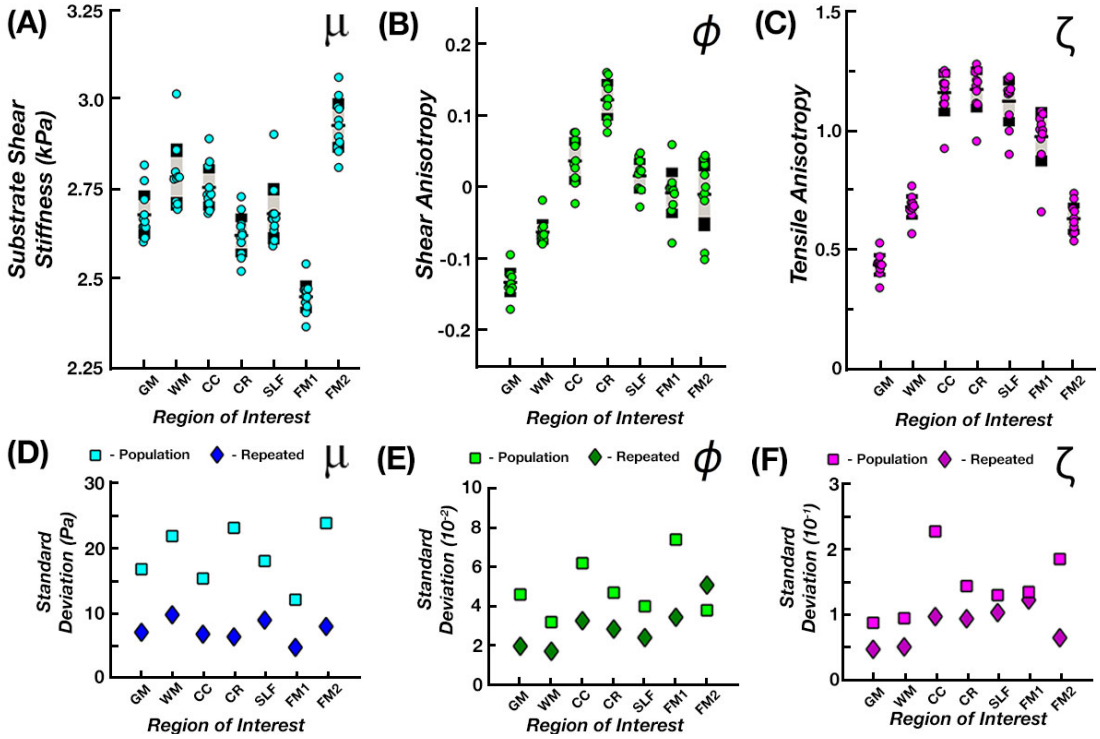

Figure 4.5: (A-C) The average parameter outcomes for the single subject data set were estimated within each of the generated ROIs and presented in box plots to analyze repeatability of the data. (D-F) The variability measures (COV or standard deviation) of the single subject data set are plotted against those of the mulit-subject data set, with the single subject data set denoted by the darker color.

Figure 4.5 presents the repeatability of the anisotropic parameter estimates in one subject scanned ten times. The μ, ϕ, and ζ parameter estimates showed relatively stable outcomes with μ standard deviations ranging from 0.05 to 0.10 kPa, ϕ standard deviations ranging from 0.017 to 0.051, and ζ standard deviation ranging from 0.048 to 0.123. Across the three parameters, μ appears to be the most repeatable of the three measures, while the anisotropy parameters appeared slightly lower. The variability of

properties in the repeated measures were significantly lower than the variability in the population sample ($p < 0.05$), where μ standard deviations ranged from 0.12 to 0.24 kPa, ϕ standard deviations ranged from 0.032 to 0.074, and ζ standard deviations ranged from 0.088 to 0.227. Comparison of these variabilities is presented in Table 4.2.

Table 4.2: This comparison shows the standard deviations of the three anisotropic parameters, μ, φ, and ζ, between the population and repeated subject data sets.

	Subject Group	GM	WM	CC	CR	SLF	F. Major	F. Minor
μ *(kPa)*	*Population*	0.167	0.218	0.153	0.231	0.180	0.120	0.238
	Repeated	0.070	0.097	0.067	0.063	0.089	0.047	0.079
ϕ	*Population*	0.046	0.032	0.062	0.047	0.040	0.074	0.38
	Repeated	0.020	0.033	0.033	0.029	0.024	0.035	0.051
ζ	*Population*	0.088	0.095	0.227	0.144	0.13	0.135	0.185
	Repeated	0.048	0.051	0.100	0.094	0.103	0.122	0.66

4.3.3 Tract Heterogeneity

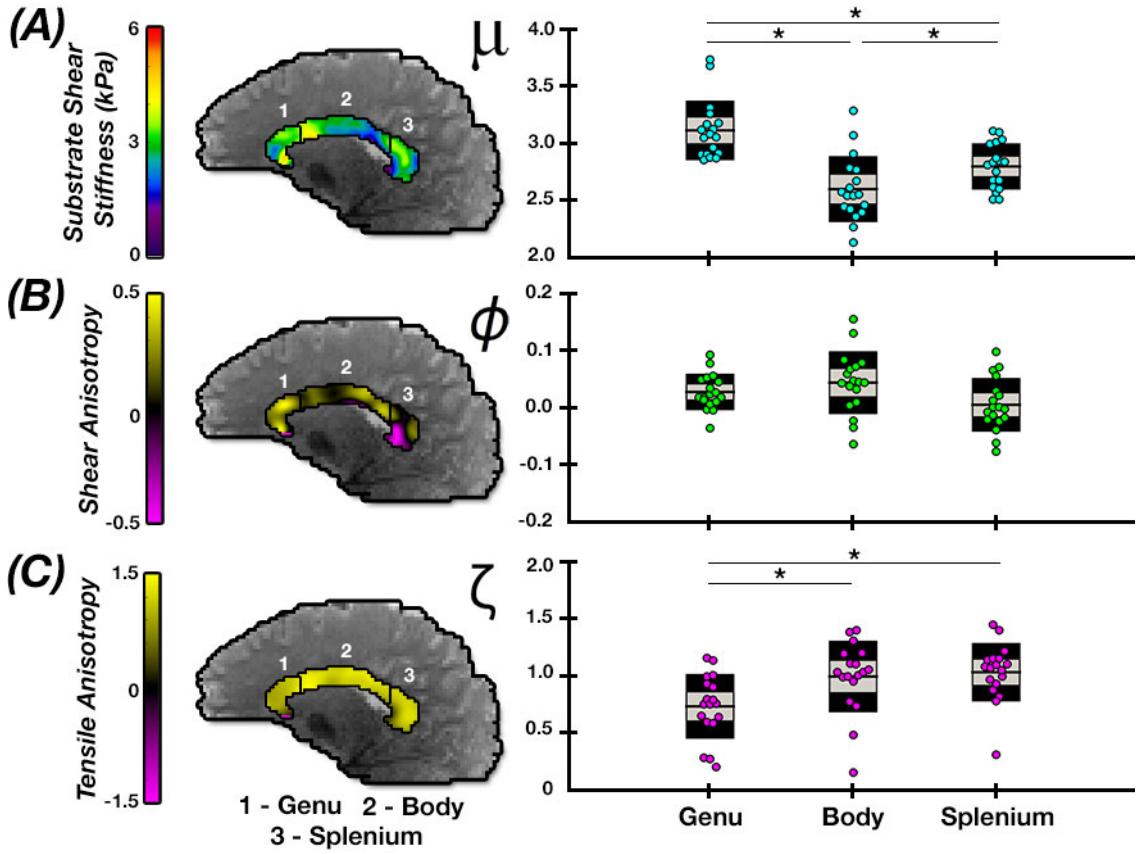

Figure 4.6: Comparison of the anisotropic parameter estimates in the subregions of the corpus callosum: the genu, body, and splenium. Significant differences in properties between regions denoted by * ($p < 0.05$).

Figure 4.6 shows the anisotropic properties of the subregions of the CC including the genu, body, and splenium to examine how sensitive TI-NLI is to the microstructural differences in tissue that exist at that level. We found significant differences ($p < 0.05$) between all three subtracts for μ, ranging from the highest stiffness in the genu (3.09 kPa) and lowest in the body (2.60 kPa). While there was no significant variation in ϕ between tracts, we do show significant differences ($p < 0.05$)

in ζ between the tracts, including between the genu (0.70) and the body (1.03) and between the genu and the splenium (1.09).

4.4 Discussion

In this work, we quantified the anisotropic properties of individual WM tracts within the healthy human brain using multi-excitation MRE and TI-NLI. We identified significant differences in anisotropic parameters, μ, ϕ, and ζ, between tracts, and found the method is sensitive to expected microstructural differences throughout WM. We also illustrated the robust nature of these measurements through calculations of parameter repeatability at the tract level. Additionally, we demonstrated the capacity of TI-NLI to capture heterogeneity within WM tracts through analyses of the corpus callosum.

Using ten data sets collected from a single subject, we quantified repeatability of TI-NLI property estimates that incorporate displacement data from the custom pneumatic multi-excitation actuator. Though previous experiments have been performed with an actuator that generated LR excitations, these data produced less repeatable results [173], likely due to unreliable contact between the actuator and the skull. With our improved multi-excitation MRE yielding improved data quality and richness with which to represent the NITI material model [221], we produced repeatable measures of anisotropic parameters from TI-NLI. Overall, the repeatability of these measurements compared favorably with those found in WM with isotropic MRE previously reported by Johnson, et al. [210]. This result suggests the reduced model-data mismatch achieved by using a more appropriate WM model offsets the added computational complexity of a two-fold increase in the number of recovered parameters (four parameters in TI-NLI: storage modulus, loss modulus, shear

anisotropy, tensile anisotropy) compared to isotropic approaches (two parameters: storage modulus and loss modulus).

Analysis of technique repeatability was performed by evaluating standard deviations of ROI parameter averages in the repeated measures from a single-subject data set. However, other studies evaluating repeatability of MRE measures use coefficient of variation (CV), which reports standard deviation relative to the mean in a group of samples. CV of μ measures reported in this study was highly repeatable with a range of 1.9 – 3.3%. The value is similar to other studies that analyzed repeatability of MRE isotropic shear stiffness within different regions of the brain, including cerebral lobes reported by Murphy, et al. (1.1 – 4.4%) [10], subcortical gray matter structures reported by Johnson, et al. (1.4 – 7.1%) [11], and hippocampal subfields reported by Delgorio, et al. (3.8 – 7.4%) [160]. CV is not an appropriate measure for evaluating the anisotropy parameters of NITI since the interpretation of CV should not significantly change by adding a numerical constant to the equation (this results in a relative change in variance though not actual variance itself [236]). As the definitions of both ϕ and ζ include subtraction of a constant, we instead reported just the standard deviation alone. When comparing variability in the repeated measures relative to variability in our sample of healthy young adults, we found significantly lower variation in the repeated subject data than across subjects. From this analysis, we conclude our measures likely reflect true tract properties rather than random measurement error, an outcome which is supported further by the significantly different parameters between tracts across all subjects. Additionally, through analyses of realistic simulated data sets, the TI-NLI method used in this study has previously

provided accurate estimations of μ, ϕ and ζ, supporting the accuracy of the measurements found in this study [222,237].

When examining the average anisotropic parameter values for each tract and comparing gray and white matter estimates, we found our properties agreed approximately with previous in vivo and ex vivo measurements. Additionally, we observed that substrate shear stiffness of white matter was substantially lower than shear stiffness estimated from an isotropic material model, as shown in Johnson, et al. [210], who measured WM shear stiffness at 3.30 ± 0.35 kPa compared to 2.79 ± 0.22 kPa of substrate shear stiffness measured in this study. Comparison of individual tracts including the CC (3.45 kPa vs. 2.83 kPa current) and CR (3.72 kPa vs. 2.68 kPa current) also followed this trend as two regions with high levels of anisotropy within WM. These differences in stiffness estimates are likely due to use of the isotropic model in previous works because isotropic estimates of fibrous WM tracts recover an average of stiffnesses parallel and perpendicular to the tract, weighted by the proportions of wave energy in slow and fast shear waves. The anisotropic model recovers a lower substrate shear modulus, and faster waves along the fibers are reflected by $\phi,\zeta>0$. We note that shear anisotropy alone is not sufficient to describe this difference between parameter measures, and tensile anisotropy also affects shear wavelength depending on wave propagation and polarization directions [196]. Estimated stiffness of GM by Johnson, et al, of 2.40 kPa was similar to our estimated substrate stiffness of 2.69 kPa, which is expected given the more isotropic nature of GM.

The degree of shear anisotropy in WM has been debated and discussed in the literature [238]. Here, we found low levels of shear anisotropy in the overall WM and

in individual WM tracts, which agrees overall with other MRE studies. Schmidt, et al. [192] found shear anisotropy in the white matter of the porcine brain to be approximately 25-35% through ex vivo MRE analysis and approximately 10-15% using dynamic shear testing. Similarly, Feng, et al. [188] analyzed ex vivo lamb brain samples using dynamic shear testing and measured a higher WM shear anisotropy of approximately 40%. While these previous findings are consistent with the work reported here in terms of identifying WM shear anisotropy of a similar magnitude, differences may be attributed to use of ex vivo samples collected at frequencies of 100-300 Hz for MRE and 20-30 Hz for dynamic shear testing, while our study was performed in vivo and at 50 Hz.

Tensile anisotropy, on the other hand, is a parameter less commonly studied in WM. In addition to shear anisotropy found in the tissue, Budday, et al. [238] estimated low levels of tensile anisotropy (~5-10%) in ex-vivo tissue during tension, though not nearly at the levels found in our study (~96%). Alternatively, Velardi, et al. [239] found high tensile anisotropy of 1.77 (~177%) recorded during ex vivo evaluation of the CC. The relatively strong tensile anisotropy, when compared to shear anisotropy, may arise from differences in how the axons and the surrounding extra-axonal matrix of the WM respond to loading during shear wave propagation. The bundles of axons and their myelin sheaths form a mechanically complex system that becomes even more complicated when including the various astrocyte and oligodendrocyte populations [19]. Higher anisotropy in tension than in shear may be explained by relatively stiff myelinated axonal fibers acting as a reinforcement structure when stretched axially (in the direction of fiber alignment). In tension, strains in the fibers and surrounding matrix must be equal. However, in shear deformations involving

displacements either parallel or perpendicular to aligned fibers, the fibers need not deform as much as the connective matrix. The behavior of the tissue in shear is thus not determined solely, or even primarily, by fiber mechanical properties, but by interactions of the fibers with surrounding matrix. Astrocytes and oligodendrocytes in WM may in fact reinforce the tissue in deformations involving displacements perpendicular to the fibers, thereby increasing substrate shear stiffness and reducing the overall shear anisotropy of the tissue.

Most MRE studies incorporating anisotropic inversion methods focus primarily on the shear components of anisotropy, μ and ϕ [166,218]. These investigations thus inherently assume existence of only slow shear waves in MRE displacement data and neglect the effects of fast shear waves which involve fiber stretching. Sensitivity to noise in recovering tensile anisotropy has been cited as a motivation for using a simplified model [218]. However, given that both slow and fast shear waves have been observed in transversely isotropic tissue-mimicking phantoms [240] and simulations, including tensile anisotropy as a parameter appears to be necessary when estimating the anisotropic viscoelastic parameters of fibrous tissues. In the current approach, excluding ζ in these analyses likely leads to increases in model-data mismatch, and thus, additional uncertainty and overestimation in other parameters, along with the missed opportunity to examine a potentially useful biomarker.

Brain tissue is known to be heterogenous in composition with WM comprising axons, astrocytes, myelin, and various extracellular matrix components. In addition, myelinated axonal fibers, the likely basis of mechanical anisotropy in WM, have been shown to vary in size, with different amounts of these fibers being present within

regions of individual tracts, such as the CC [241,242]. High levels of heterogeneity in WM axon properties have been recorded with respect to axon diameter, axon density, and inter-axon distance. Large diameter axons potentially possess a higher structural stiffness than thinner axons; and therefore, the distribution of these thin and thick axons within the tissue likely affects its mechanical response. The three CC subtracts – genu, body, and splenium – have revealed different ratios of thin and thick axons, which also correlates with levels of myelination in the tissue [241].

Within the CC tracts, we found heterogeneity in the anisotropic parameters between multiple regions of the tract, including the genu, the body, and the splenium. In the genu, we found the highest estimates of μ and lowest estimates of ζ, while the body exhibited the lowest estimates of μ and highest estimates of ζ. The heterogeneity exhibited between these regions of the CC may exist because of variation in the microstructure of the CC, primarily the axon diameter distribution [241–243]. Average axon thickness in the CC is lowest within the genu and highest within the body [244], correlating with our estimates of ζ in these tracts. The potential relationship between tensile anisotropy and average axon thickness indicates an increased structural rigidity caused by thicker axons, which possess relatively thin myelin sheaths, and therefore a smaller area fraction of myelin to axon within the tissue [245]. Alternatively, total myelin content and small-axon density are negatively correlated with axon thickness and ζ, possibly indicating total myelin content as a driver for ζ [246]. Additionally, myelin content and a small axon density correlate positively with μ, indicating a possible link between the number of axons and the supportive structure perpendicular to the fiber. Increased numbers of axons lead to an increase in myelin, and therefore a larger density of oligodendrocytes, thereby creating a more rigid structure

perpendicular to axonal direction. The finding of these previous studies of tract WM microstructure appear to correlate with the results presented here, suggesting anisotropic MRE is sufficiently sensitive to detect variations in tissue microstructure and integrity.

4.5 Conclusions

In this study, we used multi-excitation MRE to acquire full-field displacement data during shear wave propagation in the human brain, and used TI-NLI to estimate spatial maps of the anisotropic viscoelastic material parameters in a NITI constitutive model. We observed a substrate shear stiffness that was slightly lower than the measured isotropic shear stiffness in prior studies, along with modest shear anisotropy, ϕ, in agreement with past findings. Importantly, the study also considered tensile anisotropy, ζ, as a parameter when representing WM in MRE; the tensile anisotropy in healthy brain appeared to be substantially higher than its shear anisotropy. One of the primary limitations of the current method is parameter estimation in GM and the consequences for parameter estimates in neighboring WM. Due to the microstructure of GM, the NITI model with a dominant "fiber direction" may not appropriately describe the tissue behavior, or may be difficult to determine from DTI data given the low FA in GM; this may underlie estimates of negative shear anisotropy in GM, as well as at the boundaries of WM. Future studies will investigate the use of multi-excitation MRE and TI-NLI to examine anisotropic mechanical properties of WM in aging, neurological disease, and traumatic brain injury.

Chapter 5

MULTI-MUSCLE MR ELASTOGRAPHY IN THE HUMAN FOREARM

5.1 Introduction

Within the realm of human movement, object manipulation allows for interaction between an individual and their environment. However, object manipulation is one of the most complex motor functions, which requires the proper and coordinated activation of skeletal muscles to achieve complex tasks [247,248]. This activation requires high accuracy by the neuromuscular system, and to properly understand the way in which the neuromuscular system controls the muscles to manipulate objects, we must analyze either the inputs or outputs of the neuromuscular activation [249,250]. Analysis of the neuromuscular input signal from the motor cortical neurons, originating in the motor cortex of the brain, can be used to analyze motion; however, current methods do not differentiate the signals sent to the individual muscles. However, the outputs of the neuromuscular system, i.e. the force applied by each individual muscle, can provide more signal differentiation through analysis of the muscle activation.

Unfortunately, direct measurement of muscle force is extremely difficult in-vivo in humans as such protocol due to methodological challenges, as direct measurement typically requires removal of the tissue from its natural space [251].

Several methods have recently been proposed to indirectly estimate the value of muscle force using indirect measurements of muscle activity. The primary method used in published studies to quantify muscle activity has been surface

electromyography (sEMG), a non-invasive technique that involves using sensors placed on the skin to detect, to record, and to interpret the electrical signals sent by the motor cortical neurons to the muscles [93,251]. This technique has been used to great effect in multiple studies analyzing muscle activation and contraction in both static [252] and dynamic [253–255], muscle recruitment [256], and limb kinematic data [257]. However, sEMG can only be used to measure muscle activity from those muscles that contact the skin, limiting the ability of the technique to analyze the interior muscles. While this limitation is reduced if sEMG is used to estimate forces from the leg muscles [258,259], it can lead to large estimation errors if sEMG is used to estimate force application in muscle groups with multiple layers of muscle, such as the forearm [256].

Another technique for analyzing the activation of individual muscles is shear wave elastography (SWE), an ultrasound elastography (USE) technique that uses a high-intensity pulse transmitted from the ultrasound device to produce shear waves, which propagate through the tissue [124]. Previous applications of USE include analysis of activation of both muscles and tendons each in healthy [125] and pathologically affected states, including stroke [260] and cerebral palsy [261]. While SWE can provide reasonable estimates of muscular activation for both surface and deep muscles non-invasively, the limited field of view (FOV) provided by USE techniques does not allow for estimation of material properties in a large number of muscles during a singular activation. Therefore, any variation in activation between data collections will provide an inaccurate estimation of the total tissue response.

As a technique similar to SWE, magnetic resonance elastography (MRE) is a magnetic resonance imaging (MRI) technique for analyzing the health of human soft

tissue, while also providing a large FOV, through analysis of the viscoelastic mechanical properties [5,16]. MRE uses propagating shear waves from an actuator, either piezoelectric [179] or pneumatic [210,262], to quantify the viscoelastic mechanical properties of the soft tissue, including the liver and brain. Previous works have shown that MRE can detect mechanical alterations in several hepatic [7] and neurological pathologies [161,181,183]. Preliminary works with MRE and skeletal MRE studies [16] investigated the correlation between stiffness changes and contractile state of the muscle, helping to establish the basis of the technique. A recent study by Schrank, et al [263] used MRE to quantify individual muscle response to activation in real-time, in a method similar to SWE, and found responses in the shear wave velocities. Other base mechanics of the tissue were investigated by Debernard, et al. [264] in which MRE was used to investigate the age related changes in stiffness at rest and during contraction caused, by quantifying the muscle stiffness of children and middle-aged adults, providing a baseline future analysis of diseased tissue.

In this study, we propose to use a newly developed MRE technique, multi-muscle magnetic resonance elastography (MM-MRE) [265], which captures the shear wave velocity in each of the forearm muscles involved in wrist movement and object manipulation. The primary objective of this study is to determine MM-MRE's sensitivity to muscle activation, while also quantifying its effectiveness as a measurement of muscle force output. We analyzed the sensitivity of MRE to muscular activation by quantifying the individual muscle stiffness of the flexor and extensor muscles of the forearm at different multiple levels of muscle activation and at different contraction states. These contraction states included multiple amplitudes of activation

in two activation, flexion and extension, and adjusting the wrist through different positions, thereby changing muscle length.

5.2 Methods

5.2.1 Experimental Design

This study was conducted on a Siemens 3T Prisma MRI scanner in conjunction with a custom-built actuation device to produce shear waves, as shown in Figure 5.1A, which contains a passive driver. The muscle belly of the forearm is placed onto the passive driver, which is linked to the Resoundant pneumatic actuator (Rochester, MN) in the MRI control room. Additionally, the device holds the flexible MRI coil that wraps around the passive driver and forearm and has a pair of supports for the hand and wrist that they are strapped into. A force sensor is connected to the base of the hand support, to which force is applied with a visual feedback mechanism (Figure 5.1B) to ensure the proper application of force during scanning. The subject is positioned as seen in Figure 5.1A, prone with their right arm forward and positioned in the actuation device.

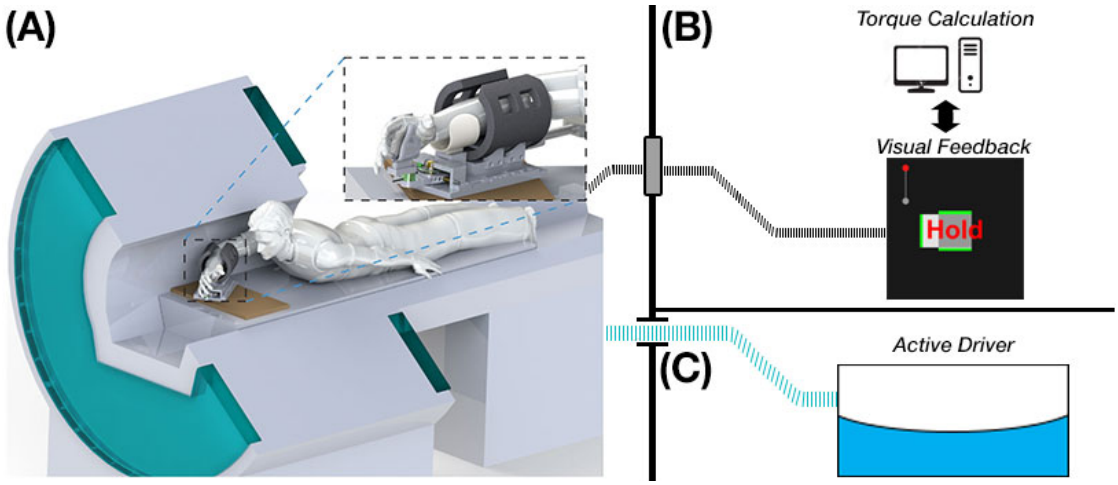

Figure 5.1: (A) Subjects are positioned head first and prone with their right arm placed in the custom MRE actuator, (C) connected to an active driver, and perform isometric contractions as cued by (B) the visual feedback system that allows the subject to visualize and maintain applied torque.

We scanned fourteen young healthy subjects (11/3 M/F; ages 22-35) through the wrist activation protocol. The protocol consists of 45 MRE scans divided between three wrist positions as defined by the angle in the flexion/extension (FE) and radial/ulnar deviation (RUD) directions $[\theta_{FE}, \theta_{RUD}] = [\{-15,0\}, \{0,0\}, \{15,0\}]$ degrees. To achieve these wrist positions, subjects manually adjusted the device by unlocking from one position and then adjusting wrist angle and relocking the hand support into the new position. At each wrist position, 15 MRE scans were collected with three scans at each of five activations states: $[\tau_{FE}; \tau_{RUD}] = [\{-1; 0\}, \{-0.5, ; 0\}, \{0,0\}, \{0.5; 0\}, \{1; 0\}]$ N·m. During each of these scans, the subjects were cued to applied and hold the designated torque through a visual feedback system. This feedback was presented to subjects through the VisuaStimDigital (Resonance Technology) audio-visual system.

We used an echo-planar imaging MRE sequence with the following parameters: 2 x 2 x 3 mm^3 anisotropic voxels; FOV = 128 x 128 mm^2; 15 slices; TR/TE = 1314/41 ms; vibration frequency = 80 Hz; 4 phase offsets; single gradient polarity; time = 21 seconds per MRE scan. The MRE scans at each wrist position were followed by an anatomical scan for region-of-interest (ROI) identification. A T_2-weighted BLADE anatomical scan was acquired with the following parameters: 1 x 1 x 3 mm^3 anisotropic voxels; FOV = 128 x 128 mm^2; slices = 60; TR/TE = 9520/79 ms.

5.2.2 Data Analysis and Statistics

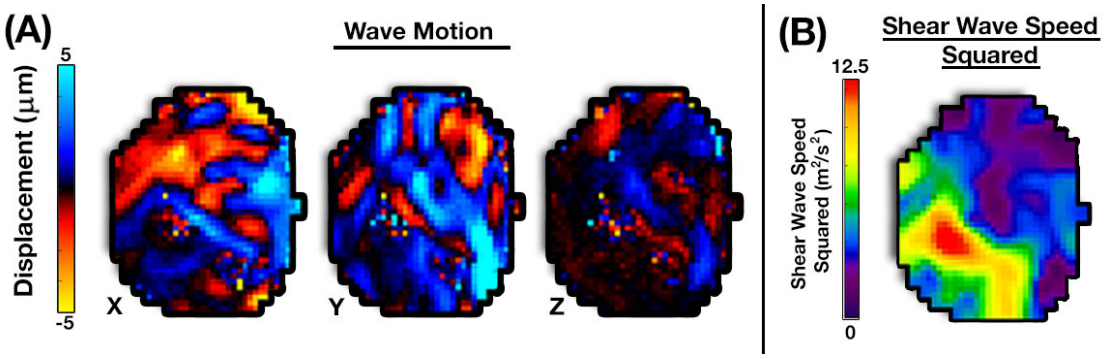

Figure 5.2: The custom actuator is used to generate (A) the shear wave motion that is then used by the non-linear inversion algorithm (NLI) to creates (B) maps of shear wave speed squared.

We used the imaged displacement fields (Figure 5.2A) from MRE to estimate the viscoelastic mechanical properties using a finite element based nonlinear inversion algorithm (NLI) [163] to determine the shear wave speed squared, or SWSS. NLI determines the properties based upon a forward problem using a finite element

solution of the displacement fields and an inverse problem, which is solved using an iterative minimization of the objective function:

$$\Phi(\theta) = \sum_{i=1}^{N_m} \left\{ \left(u_{m(i)} - u_{c(i)}(\theta) \right) \left(u_{m(i)} - u_{c(i)}(\theta) \right)^* \right\} \tag{5}$$

where $u_{m(i)}$ represents the complex-valued amplitude of the *i*th displacement measurement, $u_{c(i)}(\theta)$ is the analogous displacement calculated from the forward computational model based on the current estimate of the properties, θ, N_m is the number of measurements and * represents the complex conjugate. The solving of the forward problem involves calculating $u_c(\theta)$, while the inverse problem involves estimating the material properties through iterations of the minimization of the objective function seen above. For solving the forward FE problem, NLI models the material as a heterogeneous, isotropic, viscoelastic material which is governed by Navier's equation of the form:

$$\nabla \cdot \left(\mu(\nabla \vec{u} + \nabla \vec{u}^T) \right) + \nabla(\lambda \nabla \vec{u}) = -\rho\omega^2 \tag{3}$$

where $\vec{u}$ is the 3D displacement field, λ and μ are Lame's material constants, ρ is the density (assumed to be 1000 kg/m^3), and ∇ is the gradient operator.

Thirteen individual muscles were manually segmented using Matlab to generate individuals ROI masks using the T_2-weighted anatomical images as a reference. The muscle regions were then registered to MRE image space using FMRIB's Liner Registration Tool (FLIRT) from FMRIB's Software Library (FSL) [202] to create binary masks for analysis. The 13 muscles segmented for analysis are: abductor pollicis longus (APL), extensor carpi ulnaris (ECU), extensor pollicis longus

(EPL), extensor digitorum (ED), extensor digitorum minimus (EDM), extensor carpi radialis longus (ECRL), extensor carpi radialis brevis (ECRB), flexor carpi radialis (FCR), palmaris longus (PL), flexor digitorum sublimis (FDS), flexor carpi ulnaris (FCU), flexor digitorum profundus (FDP), and flexor pollicis longus (FPL), as shown in Figure 5.3.

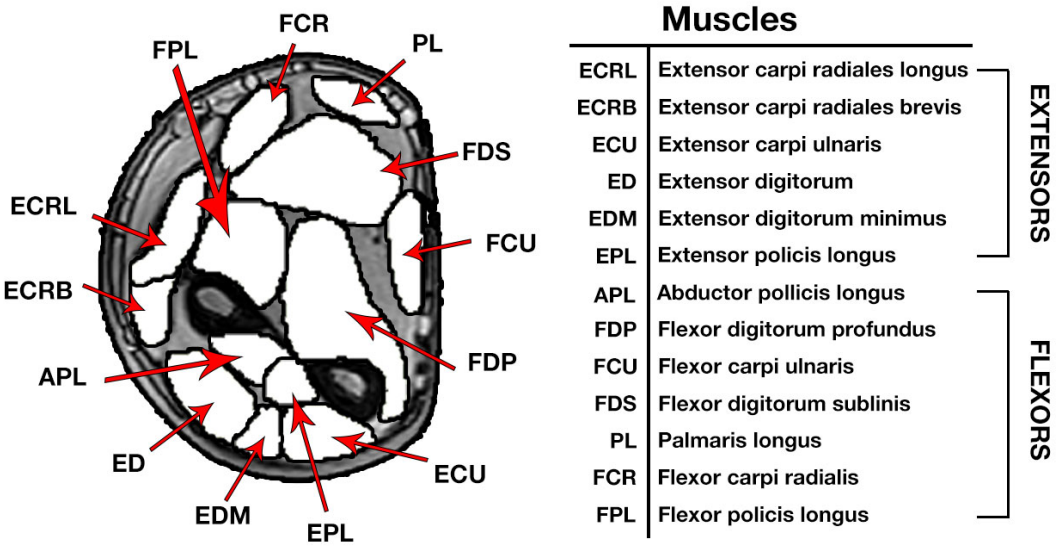

Figure 5.3: Each muscle of the thirteen muscles that are involved in wrist motion and analyzed in this study are manually segmented. A representative cross section with an region of interest defining each of the muscles is shown in the figure.

To investigate the ability of MM-MRE to measure muscle active tension, we compare the measured SWSS due to three primary factors: muscle type/recruitment; contraction intensity; and wrist position. Additionally, these factors are compared at both the muscle group level and individual muscle level. Statistical analysis consisted of mixed model ANOVAs, fitting for repeated measures, wrist position, and muscles, with post-hoc Tukey tests to test for different levels of SWSS between torque

application levels. Tests were run on the normalized SWSS values. Additionally, effect sizes for each muscle were calculated for each relationship between active contractions and their corresponding resting condition.

5.3 Results

The results of the mixed-effect nested ANOVAs performed to assess the effect of muscle contraction on measured shear wave velocity squared at the muscle group level are reported in Table 1. Multiple significant interactions were found at the individual and combined effect levels of interactions, though wrist position appeared to be the least stable predictor of muscle activation, with the lowest F-value of all individual predictors.

Table 5.1: ANOVA marginal analyses performed on the shear wave speed squared measurements collected for contraction states

Predictor	DoF	F-value	Prob.
Muscle Type	1	19.4	$p < 0.05$
Contraction State	4	20.1	$p < 0.05$
Wrist Position	2	2.24	$p = 0.13$
Muscle Type/Contraction State	4	8.68	$p < 0.05$
Muscle Type/Wrist Position	2	3.23	$p = 0.06$
Contraction State/Wrist Position	8	5.62	$p < 0.05$
Muscle Type/Contraction State/ Wrist Position	8	2.54	$p < 0.05$

5.3.1 Muscle Recruitment: Agonist vs. Antagonist Action

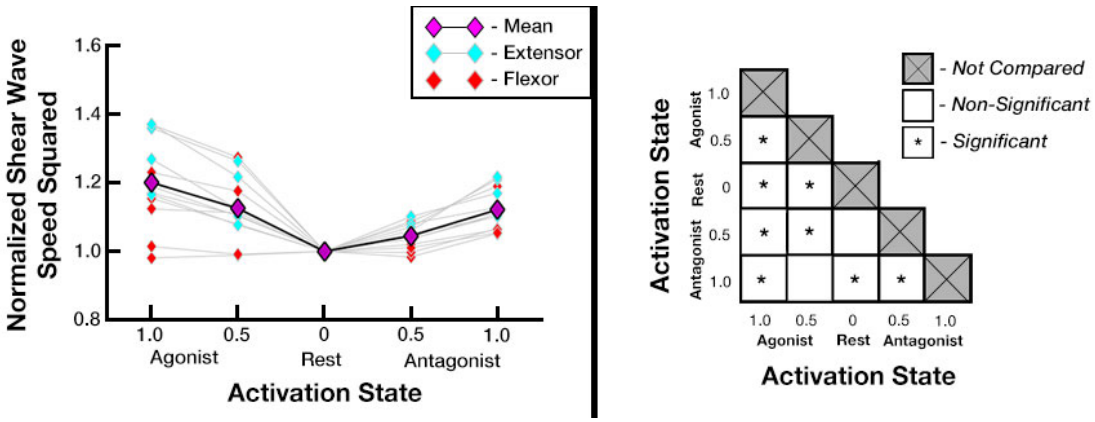

Figure 5.4: (Left) This figure shows the normalized shear wave speed squared values for all muscles during their agonist and antagonist states. Averages are denoted by data set with the black lines while individual muscles use gray lines. (Right) We show the statistically significant relationships between the various activation states for the agonists and antagonists with Statistical significance is denoted by a *.

The differences in normalized shear wave speed squared was more apparent when comparing the muscles in their agonist and antagonist state, shown in Figure 5.4, where we found significant differences in all important agonist-antagonist comparisons: active and resting states, applied torque, and corresponding agonist and antagonist action at both applied torques. The data shows an average increase of

14.9% and 10.2% during 1.0 and 0.5 N·m of torque when acting as an agonist and 10.6% and 4.2% during 1.0 and 0.5 N·m of torque when acting as an antagonist.

5.3.2 Muscle Group Analysis

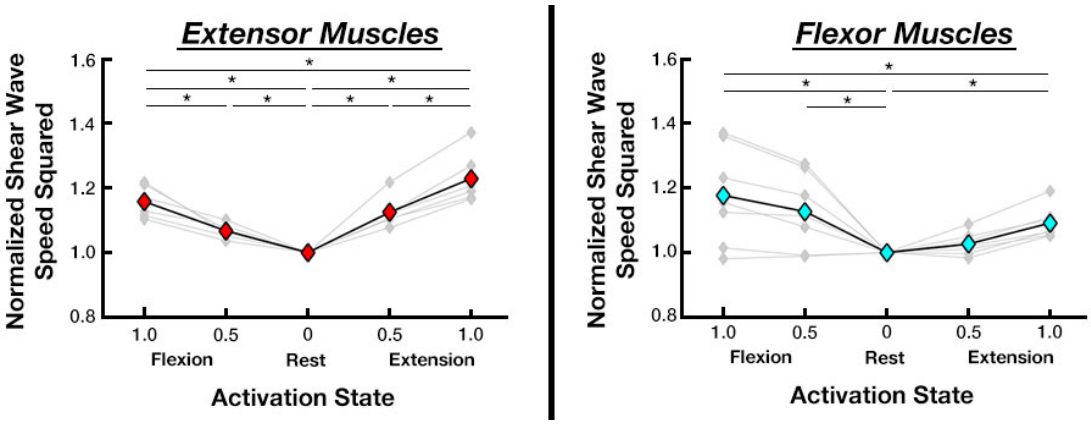

Figure 5.5: This figure shows the normalized shear wave speed squared values for the extensor (left) and flexor (right) muscles during each of the contraction states. Averages are denoted by data set with the black lines while individual muscles use gray lines. Statistical significance is denoted by a *.

Figure 5.5 shows the combined average normalized shear wave speed squared values across all repetitions, all wrist positions, and all subjects, but separated by whether the muscles are flexors or extensors. Both the flexor and extensor muscles showed significant increases during activations. Flexors showed an increase of 10.0% and 12.6% during 0.5 N·m and 1.0 N·m of flexion respectively and 1.8% and 7.3% during 0.5 N·m and 1.0 N·m of flexion and extension respectively. Extensors showed an increase of 6.6% and 13.9% during 0.5 N·m and 1.0 N·m of flexion respectively and 10.5% and 17.3% during 0.5 N·m and 1.0 N·m of extension respectively.

5.3.3 Wrist Angle Analysis

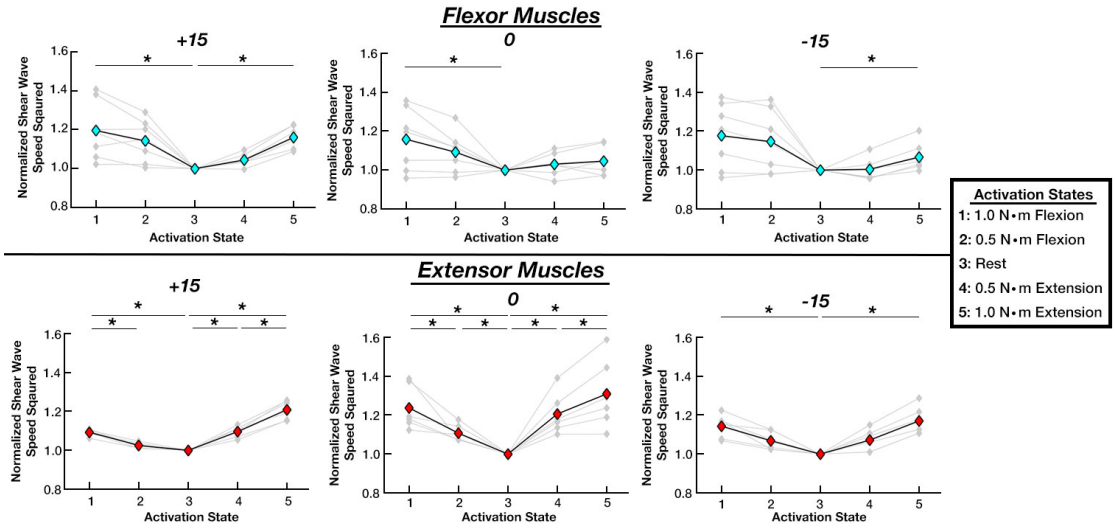

Figure 5.6: This figure shows the average normalized shear wave speed squared for the flexors (Top) and extensor (Bottom) muscles at separated by wrist position. The average of each muscle group is shown in colored diamonds and black lines, while the individual muscle averages are in light gray.

Shown in Figure 5.6 are the effects of altering wrist position on the flexor and extensor muscle SWSS outcomes across the five activation states. Both muscle groups engage differently during contractions based upon alterations in wrist position. While flexors appear to show overall increases in relative SWSS during activation while in the non-neutral wrist positions, the extensors react in an opposite manner, exhibiting decreased relative SWSS in the non-neutral wrist positions. With the group level differences variations presented in Figure 5.6, we further investigate the effects of altering wrist position along with activation state at the individual muscle level in Figure 5.7.

5.3.4 Individual Muscle Analysis

Wrist Angle & Activation State		Extensor Muscles						Flexor Muscles							# of Significant Differences	
		ECRB	ECRL	ECU	ED	EDM	EPL	APL	FCR	FCU	FDP	FDS	FPL	PL	Extensors	Flexors
-15°	Flex 1.0 N*m													*	0	1
	Flex 0.5 N*m														0	0
	Ext 0.5 N*m														0	0
	Ext 1.0 N*m		*	*		*	*	*		*					4	2
0°	Flex 1.0 N*m		*			*	*		*			*		*	3	3
	Flex 0.5 N*m														0	0
	Ext 0.5 N*m					*	*								2	0
	Ext 1.0 N*m		*		*	*	*	*							4	1
+15°	Flex 1.0 N*m		*	*					*	*		*		*	2	4
	Flex 0.5 N*m								*			*		*	0	3
	Ext 0.5 N*m	*													1	0
	Ext 1.0 N*m														0	0

Cohen's D Effect Size: 1.0, 0.8, 0.6, 0.4, 0.2, 0.0

- Non Significant p-value

Figure 5.7: This figure is a chart depicting the Cohen's D effect size for statistical differences comparing each activation to the rest condition for each of the individual flexor and extensor muscles. Activations shown in gray were non-significant, while those shown in varying levels of green were found to show significance.

In Figure 5.7, we show the resulting effect sizes of the individual muscle level comparison for those muscles that show significant differences between one of the activation states and the rest condition for each of the three wrist positions. As seen in Figure 5.7, many of the forearm muscles, including the EPL, FCR, FDS, and PL, show changes in effect size and significance in varying torque output during agonist action as the wrist angle changes, as well as occasionally during antagonist motion. Additionally, flexors and extensors both are not showing many significant activations when muscle length is longest. For flexors, this longer muscle length occurs at a wrist angle of -15º and for extensors it occurs at wrist angle of 15º.

5.4 Discussion

In this study, we introduced MM-MRE and displayed the technique's ability to identify changes to muscular tension and loading by measuring the shear wave speed at a variety of activation conditions. Specifically, we compare the effects of agonist vs. antagonist action, contraction intensity, and muscle length on the shear wave speed measures. This study provides insight into the individual and group level responses of muscles during contractile states and how the muscles in the forearm coordinate to generate isometric force.

The primary objective of this study was to analyze the correlation between torque application via individual forearm muscles and changes to the MM-MRE measured shear wave speed within the muscles. We found significant differences when comparing the applied torque activation states to the resting states, indicating that increases in the viscoelastic mechanical properties of muscles correlate with muscular activation and loading, a finding supported by previous MRE [16,263] and ultrasound elastography research [266,267]. By taking data points at multiple force application states, we determined that the changes in SWSS also correlated with level of activation and force application, as we found significantly higher shear wave speeds for torque applications of 1.0 N·m and 0.5 N·m compared to the rest condition, with 1.0 N·m also showing significantly higher shear wave speed outcomes than 0.5 N·m. This change in shear wave speed comes primarily as a result of isometric contraction, through which the muscle fibers increase tissue loading, but do not alter in length. This increased loading of the tissue is a phenomenon known as cross-bridging, [45,52,268] which describes myosin chains attaching to bonding sites on actin creating cross-bridges between the two proteins.

Muscular co-contraction is when two groups of muscles, on opposite sides of a joint, are simultaneously activated to regulate joint stability [269]. During co-contraction, muscles are classified into one of two roles, agonist and antagonist. Muscles are considered agonists when the muscles are being used as a primary driver of motion and force application in a direction, while they are considered antagonists when the muscles are being recruited to support and stabilize in response to the agonistic activation. In this work, we found significant differences in how the muscles responded when comparing how the flexors and extensor muscles acted in their agonist and antagonist states. Both flexors and extensors showed significant increases during both agonistic and antagonistic action compared to the rest condition, indicating both that they are being recruited during as a part of co-contraction and that MM-MRE is sensitive to such activation. We also found that the muscles showed significantly higher shear wave speed when being recruited for their agonist action compared to when these muscles are acting as antagonists. The difference in the muscle activation during these two muscle recruitment actions further indicates that MM-MRE provides sensitive measures of muscular activation.

Researchers studying muscular co-contraction have utilized other methods including sEMG and SWE have found similar but different results to those found in this study. For instance, Raiteri, et al. [267] used SWE along with sEMG to quantify agonistic and antagonistic responses of the lateral gastrocnemius of the calf and found a higher shear wave speed during agonist action than during antagonist. However, though the study found increases sEMG outputs during antagonist activation, they did not find the increased shear wave speed, instead finding negligible changes. Using an MRE technique, Schrank, et al. [263] found overall similar results to the outcomes

found in this study with increases in measured shear wave speed during in both agonist and antagonist conditions, with agonist action resulting in higher wave speed than antagonist.

Another important aspect of measuring these shear wave speed outcomes in skeletal muscles is the level of pre-loading due to initial tension level. Every muscle has a resting level of tension when at a neutral and natural position, as opposed to slack or overstretched, which leads to the non-significant activation levels [270]. In this study, we aimed to quantify if and how changes to these tension levels altered the responses of the measured shear wave speed by changing the wrist positioning by inducing passive flexion and extension. We subsequently found differences in the response of the forearm muscles both at the muscle group and individual muscle level of response. As shown in the study, we found higher percentage changes in shear wave speed and larger effect sizes when muscles were passively shortened and given slack with the opposite occurring during increased tension levels. We hypothesize this response is due in part to two biological means, either (A) a higher rest condition shear wave speed due to increased tension or (B) the muscle length and/or tension level alters the response ability of the muscles to generate the necessary force during isometric contraction.

Previous studies, including Raiteri, et al. [267], have shown a positive correlation between passive muscle tension and muscle length, which agrees with the changes in wrist position shown in this study. Additionally, a recent MRE study by Babaei, et al. [218] showed a relationship between shear wave speed and muscle length during passive flexion in the calf, with measurements displaying a positive correlation between the two parameters. Now, the mechanism for this increase in

muscle tension is likely tied to a third structural protein within sarcomeres known as titin [53,54]. Multiple studies have shown that titin is a primary cause of passive force enhancement during isometric contraction as it primarily acts a molecular spring, altering stiffness during muscular activation and maintains force in muscles that are stretched to long lengths, such as those during changing wrist positions.

The analysis performed in this work shows that MM-MRE provides measurements of active muscle tension that are sensitive to muscle recruitment type, tension level, and muscle length. With MM-MRE showing sensitivity to changes in shear wave speed from variations to active and passive tension, the method provides evidence of the ability to capture evidence of microstructural alterations in pathologically affected muscle, including spastic muscle due to stroke or CP. MM-MRE provides a inclusive view of the forearm muscle group, capturing all of the muscles required for wrist motion and object manipulation, and therefore allowing for simultaneous examination of each forearm muscle and helping guide rehabilitation progression through the recovery process.

5.5 Limitations

While this study was successful in showing sensitivity to muscular tension, the current technique is not without drawbacks. One of primary difficulty in any imaging modality resides in the signal quality from the data, particularly at higher resolution, measured as the signal-to-noise ratio (SNR) [271,272]. Longer scans provide the ability to increase signal while increasing the resolution increases noise within the data, creating a tradeoff between the two variables during creation of the scanning protocol. Muscle contraction presents a unique problem within the realm of MRE as it limits the possible acquisition time of each scan before muscle fatigue sets in from

excessive cross-bridge loading, particularly at larger loads [54]. Once muscle fatigue occurs, the data is prone to additional noise and artifacts from subject motion. To account for this, the scanning time is shortened to acquire the best data possible in the limited time frame.

Another data quality challenge within this data is the inclusion of the bones within the acquired volume and the size of the bones compared to the forearm muscles. Forearm muscle are relatively small when compared to those in other appendages such as the upper arm, calf, or thigh, and though the bones are also smaller, their relative size to the muscles is larger. NLI has typically been used in much larger tissues with larger matrix volumes and the material model does not apply to bone as bone is several ordered of magnitude stiffer than the surrounding tissues of interest, thus causing data mismatch and uncertainty in the outcomes.

While there have been multiple MRE and SWE studies utilizing isotropic estimation methods for skeletal muscle, recent studies have utilized anisotropic material models for parameter estimation because of the fibrous nature of the tissue [166,169,218]. In this study, however, we use an isotropic inversion in NLI to estimate shear wave speed due the more robust nature of current isotropic methods compared to anisotropic ones as an appropriate anisotropic MRE method for the forearm, including diffusion and heterogeneity measures across the arm, have not yet been developed. Though as anisotropic techniques become more robust, those would be more suitable method for parameter estimation.

5.6 Conclusions

In this study, we quantify MM-MRE's sensitivity to the activation of skeletal muscles in the forearm by collecting MRE data during a variety of contraction

conditions and wrist positions. The MM-MRE outcomes of SWSS are then used with a muscular model to estimate the individual contributions of each of the forearm muscles. MM-MRE showed linear increases of SWSS during varying levels of contraction and signs of co-contraction activation with agonist and antagonist activity, including significant differences between how a muscle reacts when being recruited into one of these two functions. Furthermore, we discovered how changing the position of the wrist, and therefore the length of the muscles, affected the different muscle activations. We then showed promising results while using the SWSS estimations from MM-MRE to estimate the force contributions of the individual muscles. Future directions of this work include creating a two degree of freedom method to better estimate these individual contributions from muscles and then application of this technique in the rehabilitation of stroke and CP subjects.

Chapter 6

IN-VIVO ESTIMATION OF ANISOTROPIC MECHANICAL PROPERTIES OF THE GASTROCNEMIUS DURING TENSION-BASED LOADING

6.1 Introduction

Skeletal muscle contraction is a complex event that requires the microscale cellular components to move in concert through active tension to achieve or oppose motion. This active tension is accumulated and discharged during a process known as cross-bridge cycling, where actin and myosin proteins, the building blocks of sarcomeres, connect and release from one another [45,52]. Tension can be also accrued in the muscle through variations in muscle length, due to elastic proteins known as titin, which induce a passive tension within the tissue [53–55]. In the case of pathology, such as spastic cerebral palsy (CP), where the structural organization of muscle fibers is altered, the functional response of the tissue is severely limited [273,274]. Although standard assessment of skeletal muscle health for neuromuscular pathologies utilize electromyography (EMG) to evaluate tissue function or dysfunction [252,275]the use of in vivo imaging may improve the evaluation of skeletal muscle health through measures of structural integrity as well as function.

An emerging method for quantifying the mechanical properties of skeletal muscle is magnetic resonance elastography (MRE) [5]. MRE is an MRI technique that measures propagating time-harmonic shear waves to probe the mechanical properties of a particular tissue, and is often used to analyze the health of soft tissues such as the liver and brain [6,7]. One of the primary advantages of MRE over other techniques

(e.g., ultrasound shear wave elastography, SWE [125,276], or EMG) is simultaneous ¬in vivo quantification of functional responses of multiple muscles over its large field of view. MRE has been used to capture functional changes in skeletal muscle during contraction across a variety of muscle groups, including bicep [16], thigh [277], forearm [265], and calf [263]. In particular, Zonnino, et al. [265] quantified the effects of variable isometric contraction on MRE estimates in the human forearm. Additionally, Schrank, et al. [263] used a real-time MRE method to quantify parameter changes in calf muscles during isometric contraction loading conditions. Other studies utilizing MRE to examine skeletal muscle have investigated relationships between mechanical property changes and aging [264,278], exercise [279,280], or pathology, such as Duchenne's muscle dystrophy [14,281,282].

Though these previous studies have demonstrated the potential of MRE for characterizing skeletal muscle, they have largely employed isotropic material models which are susceptible to inaccurate estimation of the tissue mechanical properties due to its fibrous composition, which typically leads to anisotropic mechanical behavior. Several recent MRE studies of skeletal muscle have attempted to model the anisotropy, including works by Green, et al. [166], Guo, et al. [169], and Babaei, et al. [218]. All three of these investigations modeled muscle as an incompressible, transversely isotropic tissue but did not include tensile anisotropy, and therefore not capturing effects of fiber stretching on the propagating shear waves, and thus estimated just two anisotropic shear parameters defining the tissue response to shear deformations parallel and perpendicular to the muscle fibers. These studies examined passive muscle structure, though not the effects of contraction on anisotropic parameters when the mechanical response is likely to be more complex. Fiber

stretching, a critical component of the mechanical response of muscle during contraction, cannot be represented by two shear parameters alone, and instead requires an additional parameter to capture the tensile mechanical response. Recently, a nearly incompressible, transversely isotropic (NITI) material model, which incorporates three parameters to describe the tissue – substrate shear stiffness, shear anisotropy, and tensile anisotropy – has shown promise in modeling both the shear and tensile components of anisotropy in fibrous human tissue when combined with MRE displacement data [168,188,196,221]. Through estimation of the three independent mechanical property parameters, the NITI material model provides an effective framework from which to quantify the mechanical response of skeletal muscle as it is functionally activated.

In this study, we estimated the anisotropic mechanical properties of skeletal muscle using the recently developed transversely isotropic, nonlinear inversion algorithm (TI-NLI) that incorporates wave motion fields from MRE with fiber orientation data acquired with diffusion tensor imaging (DTI) [222,237]. We performed two experiments to probe the mechanical reaction of skeletal muscle to contraction: the first to investigate passive contraction through stretching or lengthening of the muscle and the second to explore the mechanical effects on muscle to isometric contraction. We used TI-NLI to quantify the mechanical changes in calf skeletal muscle during tension-induced contraction and observe the differing effects of the two loading conditions.

6.2 Methods

6.2.1 Experimental Setup

Eight healthy young adult subjects (4/4 M/F; ages 23-26 years) completed the study approved by our Institutional Review Board. All participants were imaged in a Siemens 3T Prisma MRI scanner. Each subject was positioned supine, feet first in the bore with legs draped over an adjustable support (Figure 6.1). Two RF receiver coils were wrapped around the calf with two custom-made passive drivers to generate the necessary shear waves for MRE in conjunction with the Resoundant pneumatic actuation system. For Experiment 1, the right ankle of each subject was placed in a custom brace to limit range of motion while the height of the knee was adjusted to achieve three different angles: 105°, 135°, and 165°. For Experiment 2, the right foot of each subject was positioned on a pedal device. Individuals were instructed to press and hold down one side of the footplate to compress fully one of the plastic springs (Figure 6.1B) for the duration of each MRE scan. This positioning induced isometric dorsi- or plantar-flexion depending on which spring the subject compressed.

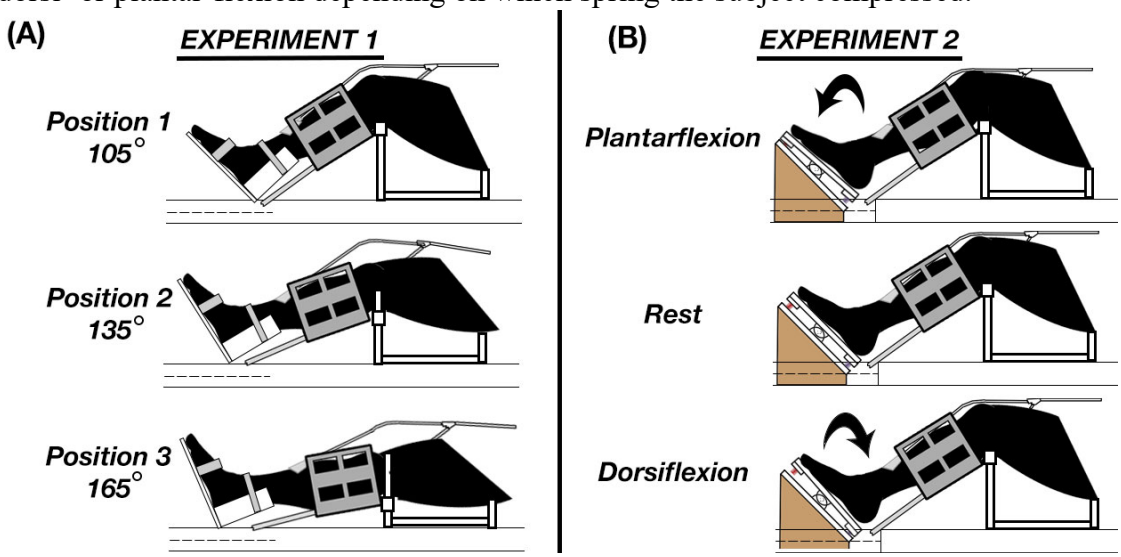

Figure 6.1: (A) Experiment 1 entails placing the subject's foot in a custom ankle brace to maintain a constant ankle angle while the angle of subject's knee is altered through raising or lowering the leg support. (B) Experiment 2 replaces the ankle brace with a peddle-like device which induces isometric contraction when the subject pushes against one of the two springs during plantar- or dorsiflexion, while their leg is supported at a constant knee angle.

6.2.2 Imaging Protocol

MRE data was collected using an echo-planar imaging (EPI) sequence with the following parameters: 2 x 2 x 3 mm^3 voxel size; FOV = 160 x 160 mm; 80 x 80 matrix; 20 slices with 3 mm thickness; repetition time (TR)/ echo time (TE) = 2400/59 ms; vibration frequency = 50 Hz; 4 phase offsets; dual gradient polarity; total acquisition time = 65 sec. We also acquired a diffusion tensor imaging (DTI) scan with resolution and FOV matched to the MRE data with TR/TE = 2200/69 ms, b = 400 s/mm^2 and 30 directions, as well as a T1-weighted scan with the following parameters: 1.25 x 1.25 x 3 mm^3 voxel size; FOV = 160 x 160 mm; 128 x 128 matrix; 20 slices; TR/TE = 2200/11 ms;

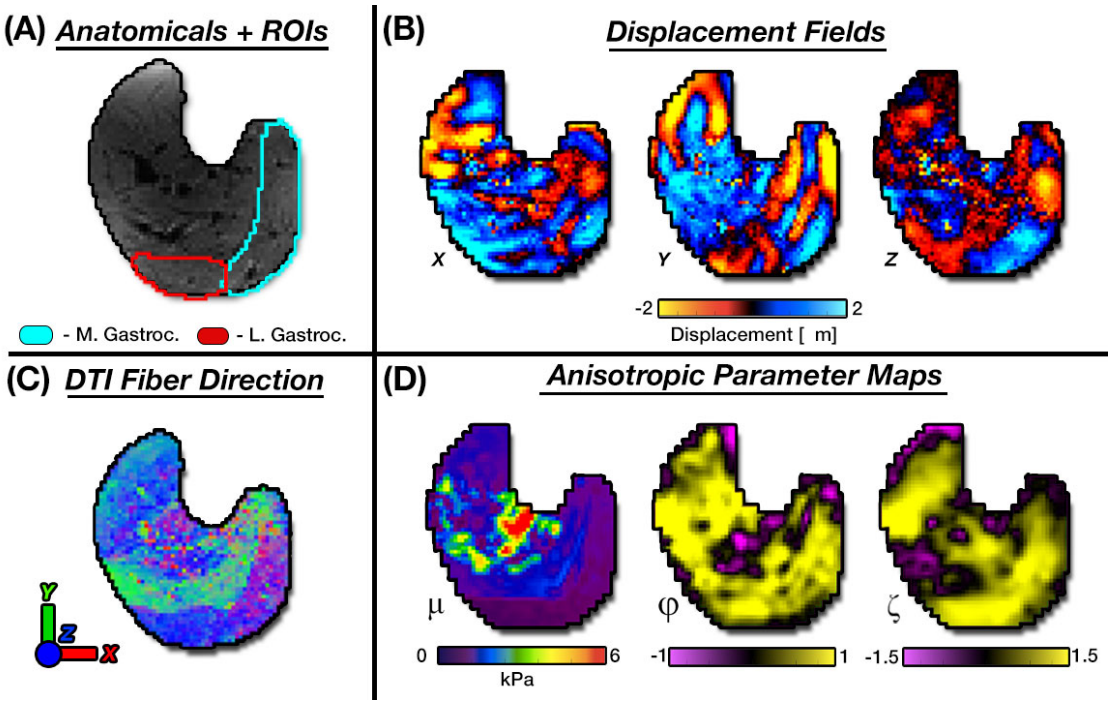

Figure 6.2: Two primary muscles, (A) medial and lateral heads of the gastrocnemius, were investigated to determine the anisotropic material parameters. There material parameters were solved for by combining (B) MRE displacement fields and (C) fiber directions from DTI. (D) The anisotropic parameters solved for include substrate shear stiffness (μ), shear anisotropy (ϕ), and tensile anisotropy (ζ).

Each subject completed both Experiment 1 and Experiment 2 within the same scanning session. Experiment 1 consisted of a set of image acquisitions at each of three knee angles (105°, 135°, and 165°). At each position, we collected three repeated MRE scans, one DTI scan, and one T1-weighted anatomical scan. Experiment 2 consisted of three repeated MRE acquisitions during each contraction condition – dorsi-flexion, plantar-flexion, and rest – for a total of nine MRE scans. Additionally, we acquired one DTI scan and one T1-weighted anatomical scan as in Experiment 1.

6.2.3 Data Processing

Diffusion data was processed with the FMRIB's Diffusion Toolbox (FDT) from FMRIB's Software Library (FSL) [202]. We then used FMRIB's Linear Image Registration Tool (FLIRT) to register the diffusion-weighted images with MRE image space using the diffusion gradient directions for each image rotated according to the registration. From there, fractional anisotropy and the first eigenvector (V1) were calculated using FDT.

Wave motion fields were calculated from MRE data after subtraction to remove background phase, phase unwrapping with FSL PRELUDE [283], and temporal Fourier filtering to isolate the harmonic motion of interest. We used a transversely isotropic, non-linear inversion algorithm (TI-NLI) to estimate anisotropic material parameters based on the acquired wave fields and the primary eigenvector from DTI, the assumed fiber direction, as shown in Figure 6.2 [222,237]. TI-NLI is an iterative, finite element-based inversion that estimates spatial maps of the three material property parameters used to describe a NITI model: substrate shear modulus, G_2, shear anisotropy, $\phi = G_1/G_2 - 1$, and tensile anisotropy, $\zeta = E_1/E_2 - 1$. Subscript 1 denotes a property parallel to the direction of the fiber, or normal to the plane of isotropy, while a subscript 2 denotes a property perpendicular to the fiber direction, or in the plane of isotropy. The substrate shear modulus is defined by the equation: $G_2 = G_2' + iG_2''$, where G_2' is the substrate storage modulus, and G_2'', is the substrate loss modulus. Here we calculate the substrate shear stiffness as $\mu_2 = \frac{2|G_2|^2}{G_2'+G_2''}$, which describes the square of the wave speed perpendicular to the fibers. We also considered the shear stiffness parallel to the fibers as $\mu_1 = \mu_2(1 + \phi)$. We note that the parameters estimated in this study are "effective" mechanical properties due to the nonlinear acoustoelastic effects of the pre-strain fields on the skeletal muscle [284].

We estimated the average anisotropic properties in individual calf muscles, specifically the medial and lateral heads of the gastrocnemius, which were manually traced from anatomical images. Within TI-NLI, we applied soft prior regularization using these generated volumes as a priori spatial information to stabilize the estimation of properties [210]. To analyze differences in muscle parameters between contraction states, we applied a linear mixed model with variables of muscle, subject, and position as fit parameters for Experiment 1, and a one-way ANOVA with repeated measures within subject and muscle with relationships between a post-hoc Tukey test for Experiment 2.

6.3 Results

6.3.1 Experiment 1 – Passive Lengthening

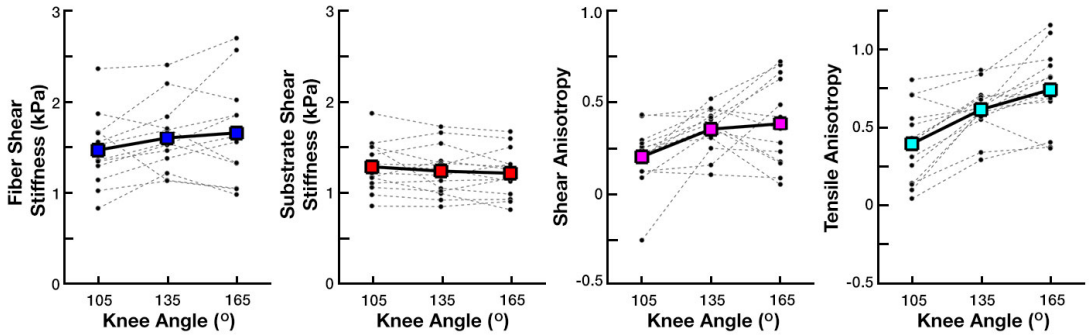

Figure 6.3: Results of Experiment 1, comparing the effects of increasing muscle length with knee angle on the NITI anisotropic parameters, from left to right, fiber shear stiffness, substrate shear stiffness, shear anisotropy, and tensile anisotropy.

Figure 6.3 displays results from Experiment 1 and shows changes in the anisotropic material parameters in the gastrocnemii when placed in the three knee positions: 105°, 135°, and 165°. Associated descriptive statistics are summarized in Table 6.1. We found increases in μ_1, ϕ, and ζ as knee angle increases (each $p < 0.05$), while μ_2 stayed relatively stable. Using data from both muscles individually, μ_1 increased by approximately 7.6% overall, from 1.66 kPa to 1.79 kPa, between the initial and final position ($p = 0.061$). ϕ, however, increased 7.6% between a knee angle of 105° and 135° and 1.8% between a knee angle of 135° and 165°, for a total increase of 9.5% from 0.30 to 0.33 ($p < 0.05$). ζ exhibited similar increases the three knee positions – 38% between a knee angle of 105° and 135° and 33% between a knee angle of 135° and 165° for an overall increase of 84% ($p < 0.05$).

Table 6.1: The average and standard deviations of each of the four parameters at the three different knee angles measured during Experiment 1.

	$\boldsymbol{\mu_1}$(kPa)	$\boldsymbol{\mu_2}$(kPa)	$\boldsymbol{\phi}$	$\boldsymbol{\zeta}$
105°	1.49 ± 0.41	1.28 ± 0.27	0.20 ± 0.17	0.40 ± 0.24
135°	1.62 ± 0.40	1.23 ± 0.27	0.35 ± 0.12	0.62 ± 0.16
165°	1.67 ± 0.57	1.21 ± 0.26	0.38 ± 0.24	0.74 ± 0.25

6.3.2 Experiment 2 – Active Muscle Contraction

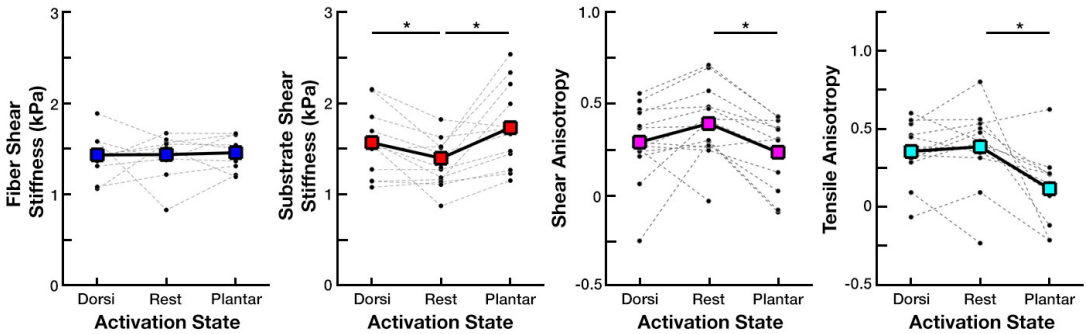

Figure 6.4: This figure shows the results of Experiment 2, comparing the effects of isometric contraction on (from left to right), fiber shear stiffness, substrate shear stiffness, shear anisotropy, and tensile anisotropy. Statistically significant differences in the data set are denoted by a *.

Figure 6.4 highlights the anisotropic parameter estimates of gastrocnemius during isometric contraction in dorsi-flexion and plantar-flexion relative to rest from Experiment 2. Associated descriptive statistics are summarized in Table 6.2. Here, the parameters – μ_2, ϕ, and ζ – exhibited significant changes between the contraction states ($p < 0.05$), while μ_1 was relatively stable. From the rest condition, μ_2 increased from 1.39 kPa to 1.56 kPa during dorsiflexion ($p < 0.05$) and to 1.73 kPa during plantarflexion ($p < 0.05$), increases of 20% and 13%, respectively. ϕ and ζ had opposite responses, instead showing non-significant decreases from 0.13 to 0.03 (34.6%; $p = 0.106$) and 0.39 to 0.36 (6.9%; $p = 0.72$) during dorsiflexion, respectively, and significant decreases from 0.13 to -0.02 (66.7%; $p < 0.05$) and 0.39 to 0.12 (67.5%; $p < 0.05$) during plantarflexion.

Table 6.2: The average and standard deviations of each of the four parameters at the three different active contraction states measured during Experiment 2.

	$\boldsymbol{\mu_1}$(kPa)	$\boldsymbol{\mu_2}$(kPa)	$\boldsymbol{\phi}$	$\boldsymbol{\zeta}$
Dorsiflexion	1.43 ± 0.29	1.56 ± 0.36	0.03 ± 0.20	0.36 ± 0.18
Rest	1.43 ± 0.38	1.39 ± 0.30	0.13 ± 0.19	0.39 ± 0.24
Plantarflexion	1.45 ± 0.19	1.73 ± 0.45	-0.02 ± 0.19	0.12 ± 0.23

6.4 Discussion

In this study, we quantified the effects of varying the state of skeletal muscle, including during isotropic contraction and passive lengthening, on the anisotropic mechanical properties of the medial and lateral heads of the gastrocnemius muscle. Effects were evaluated through anisotropic MRE utilizing TI-NLI to estimate spatial maps of fiber shear stiffness, μ_1, substrate shear stiffness, μ_2, shear anisotropy, ϕ, and tensile anisotropy, ζ.

Most evaluations of anisotropic mechanical properties of skeletal muscle quantify the resting state shear stiffness and shear anisotropy. In this study, measurements of shear stiffness and shear anisotropy were relatively similar to results from previous reports in the MRE literature with similar vibration frequencies (μ_1 = 1.26 – 1.32 kPa , μ_2 = 1.53 – 2.00 kPa, and ϕ = 0.18 – 0.59) [166,169,218]. None of the prior published studies reported ζ as a material parameter; hence, comparisons were not possible with the data presented here. In previous studies, MRE-

measurements of calf muscles have utilized large knee angles with a nearly-straight leg and a non-flexed ankle, most similarly to our Position 3 at 165° knee angle during Experiment 1. The TI-NLI employed in this study has been demonstrated to accurately recover μ, ϕ and ζ images using realistic simulated data which supports the accuracy of our measurements [222,237].

In Experiment 1, we showed the degree of anisotropic parameter change during alterations in passive tension on a muscle through changes in muscle length. The gastrocnemius is the only dual-joint muscle in the calf, meaning it crosses both knee and ankle joints. Therefore, by limiting the motion of the ankle, we can alter the length and pinnation angle of the gastrocnemius by changing knee angle and increase the length of the sarcomeres within the muscle fibers [285,286]. Increases in length of the muscle also increase the applied load on the muscle fibers [46,57,58]. This outcome is reflected in results from Experiment 1, where μ_1, the shear stiffness in planes parallel to the fiber direction, increased with increasing knee angle. The pathway for the increase in tension is possibly related to titin, the third structural protein within sarcomeres which studies suggest causes passive force enhancement [53,54]. Titin primarily acts as a molecular spring and can alter its stiffness during muscle activation to maintain stability in muscles that are stretched to long lengths. Additionally, stretching of collagen-based structures within the muscle, including epimysium, perimysium, and endomysium as well as the muscle fiber extracellular matrix, likely increases the effective fiber shear stiffness due to increasing levels of prestress [287].

In a previous MRE study, Babaei et al. [218] found a similar relationship between μ_1 and muscle length, though results differed for μ_2 and ϕ, as μ_2

significantly increased while ϕ stayed relatively stable as the muscle stretched. One possible reason for differences in these results is the different material models used in the two studies. Babei, et al. assumed tissue incompressibility with only the presence of slow propagating shear waves, and accordingly, no fast propagating shear wave effects (i.e. only shear anisotropy and no tensile anisotropy). Ignoring the fast shear wave component in skeletal muscle may bias estimates of shear moduli, since fast waves are likely to be present in an NITI material unless care is taken to avoid their excitation [168]. Under the assumption of full incompressibility, tissue stretching must be represented in other measurements, possibly resulting in the mismatch in outcomes between the two studies. Another possible explanation could be the lack of knee restraint in the Babei study. As previously noted, the gastrocnemius muscle can be stretched or shortened by changing the angle of either the ankle or knee; hence, while the ankle angle was controlled, any readjustment of the subject's knee angle will cause changes in length and pinnation angle of the muscle, and potentially change the resulting material property parameter estimates.

In Experiment 2, we demonstrated the effects of isometric contraction on the anisotropic material properties of the gastrocnemius. These results indicate that as this activation occurs, the muscle increases its shear stiffness in the direction perpendicular to the fiber direction. Previous studies utilizing MRE for examining skeletal muscle during activation, such as works by Zonnino, et al. [265] and Schrank, et al. [263], also reported increases in stiffness estimates during isometric contractions. These studies also found greater stiffness effects during agonist rather than antagonist actions. We find greater parameter changes during plantar-flexion, when the gastrocnemius functions as an agonist, as compared to dorsi-flexion, or antagonist

action. Our TI-NLI anisotropic property estimates suggest the increase in stiffness estimated in these previous studies was a result of stiffening of the tissue in the perpendicular direction with little to no increase in stiffness in the fiber direction during activation. We expect these increases are a consequence of the cross-bridge model attributed to Huxley [45], which indicates that cross-bridges are created by myosin and actin bonding that exert forces along the bridge during bonding in conjunction with conversion of ATP into ADP.

By illuminating two potential cellular mechanisms of action, the two experiments reported here highlight how anisotropic MRE utilizing TI-NLI can evaluate multiple forms of muscle function. First, we observed how shear stiffness parallel and perpendicular to muscle fibers, μ_1 and μ_2, influenced the complex relationship between ϕ and muscle loading. μ_1 appears to correlate with increasing tension caused by muscle lengthening through passive stiffening, while μ_2 captures the cross-bridging during isometric contraction. On the other hand, while ζ appears to be a necessary component of the parameter estimation process and shows changes with both passive lengthening and active contraction, its trends are similar to those of ϕ in each case.

However, muscle under tension not only changes the shape and structure of cells but also generates significant pre-strain fields which affect shear wave propagation. Muscle stress fields can be reasonably approximated as having symmetry around an axis along the length of the muscle, so these effects can be adequately modeled by effective parameters of a NITI model [288]. A simple model of passive stretching produces tensile pre-stress fields along the muscle, and radially symmetric compressive pre-stress perpendicular to the muscle axis due to the Poisson effect

[289]. This will increase shear wave speed along the muscle axis, and decrease wave speed across the axis, giving an increased effective anisotropy. Active muscle contraction also has tensile stress along the muscle axis; however, this is generated by shortening the muscle which increases cross-sectional area which gives a tensile pre-strain. This increases wave speed in both directions, giving an increased overall effective stiffness, and lower effective anisotropy. Accurate modeling of these acoustoelastic effects [284] requires a nonlinear computational model and knowledge of the both the pre-strain field, requiring the unstressed state to be known, and the nonlinear mechanical properties. As these requirements are difficult to achieve with in vivo imaging, separation of the mechanical property changes from acoustoelastic changes is not currently feasible. Therefore, a small displacement assumption is used in the estimation of "effective" mechanical properties which consist of the true unstressed properties mixed with the nonlinear acoustoelastic effects from the pre-strain field. These effective properties are altered by both changes in cellular structure and changes in muscle function, so, provided conditions are controlled carefully, they can provide useful insight into muscle heath.

While the methods utilized in this study were effective at capturing the viscoelastic responses of muscle function with MRE, the study had several limitations. While the MRE and DTI scans have standard imaging noise, other biological tissues and structures within the volume create additional noise and discontinuities that may affect outcomes [271]. These include the fibula, major blood vessels, fatty tissue, and muscle fascia, each of which create challenges for MRE as they introduce model-data mismatch that we sought to minimize by incorporating spatial information in the inversion process. Muscle fatigue also potentially affected outcomes from Experiment

2 that required consistent force generation over a period of time [290,291]. Experiment 2 was designed using springs that generate a load below 15% MVC for an average human adult to avoid significant fatigue during the short imaging time, but this threshold is variable between individuals and levels of force application were imprecise as no in situ measurements were recorded. Recommendations for future studies include a tailored force output requirement based on an individual subject's MVC and a visual feedback system so that a participant can maintain consistent force output. Additionally, subject knee and ankle positions in both experiments were relatively well controlled and consistent for each individual, however they were unmeasured and could not be accounted for during statistical analysis, and differences between individuals may account for some of the variability in observed outcomes.

6.5 Conclusions

In this work, we use anisotropic MRE to quantify effects of functional changes to the medial and lateral heads of the gastrocnemius. Using TI-NLI, we generated anisotropic material parameter maps and estimated each parameter within the muscle volumes of participants for each of three conditions during each experiment capturing both passive lengthening and active contraction. Anisotropic mechanical parameters exhibited different trends based on the loading condition, and MRE with TI-NLI may allow us to examine functional response of muscle tissue in health and muscle-altering pathologies, such as cerebral palsy.

Chapter 7

CONCLUSIONS AND FUTURE DIRECTIONS

7.1 Conclusions

Over the course of this work, we show the effectiveness of MRE to illuminate structural and functional characteristics in fibrous soft tissues through quantification of viscoelastic material parameters. Additionally, we show how multi-excitation and TI-NLI can be used to provide an improved estimation of tissue properties, particularly due to structural variations and functional changes.

We approach the evaluation of brain WM properties through two principal methods. Initially, we analyze multi-excitation shear wave propagation throughout the brain as well as the resulting slow and fast shear waves in WM based upon the previous works for Anderson, et al. [173] and Tweten, et al. [168,196]. Through use of directional filtering [197], we determine that a single excitation during brain MRE can create multiple propagating waveforms throughout the brain, with almost every point in the brain affected by at least two unique shear wave propagations. We theorize that these unique waveforms result from the indirect shear wave generation in brain MRE, where the external actuators first propagate waves through the skull, which then in turn create additional wave propagations from other focal points where the skull and brain make contact, including the falx and tentorium [198]. As we use AP and LR excitations in multi-excitation MRE, we apply this directional filtering to both excitations and found that they produce unique waveforms throughout most of the brain. As such, we conclude there is sufficient wave information from these slow and

fast waves to estimate the anisotropic viscoelastic mechanical properties based upon the NITI material model.

We build on this work to next combine multi-excitation MRE with the recently developed TI-NLI [222,223] to generate whole brain measurements of anisotropic material parameters. From these parameter estimations, we determine that this technique can provide repeatable and tract specific estimates of mechanical anisotropy within WM. One major finding is the strong tensile anisotropy in WM tracts, supporting the need for it as a necessary parameter when estimating WM or other fibrous soft tissues, even though many anisotropy measurements through MRE make assumptions that eliminate the tensile component from the model [166,169,218]. By showing parameters differences at both the tract and sub-tract level, we demonstrate the capacity of this technique to examine differences due to structural variances at the subject level, and indicating future utility in analyzing pathological changes to WM tissue.

The second half of this work primarily focuses on the measurement and analysis of functional changes to fibrous skeletal muscle with MRE. We use MM-MRE to quantify shear stiffness changes in the human forearm and examine how loading through during isometric contraction changes these outcomes. We determined that MM-MRE provides an avenue for in-vivo measurements of muscle function through three primary factors: a correlation between combined muscle load and shear stiffness parameter outcomes; significant shear stiffness differences between muscles during agonist and antagonist actions; and variation of shear stiffness outcomes with different levels of initial loading due to muscle length. Though we determined that MRE is sensitive to muscle contraction, isotropic measurements of fibrous tissue

provide a limited representation of the possible response, and using an anisotropic MRE technique would likely result in more accurate and complete representation of the functional response of skeletal muscle tissue during a similar isometric loading condition.

Therefore, we use MRE in conjunction with TI-NLI to evaluate functional changes to the gastrocnemius muscle of the calf during isometric contraction to better understand the mechanical response of skeletal muscle in-vivo. We collected data during passive muscle lengthening and found increased fiber shear stiffness as well as shear and tensile anisotropy as the muscle length increased. Additionally, we measured anisotropic parameters during both relaxed and isometric contraction states at a fixed position and found that loading increased substrate shear stiffness, which results in lower tissue anisotropy. The difference in mechanical response to these two functional changes indicates a sensitivity to multiple influences from functional changes, as different mechanisms are likely responsible for the observed tissue behaviors [45,53,54]. By observing these different responsible mechanisms of actions, we demonstrate the capability of MRE to provide a multifaceted approach to analyzing response to functional measures and provide a valuable tool for evaluating further changes in response due to injury-based or pathological changes to skeletal muscle.

7.2 Future Directions of Work

The anisotropic MRE techniques developed and employed in this work provide a framework for future application to pathology and other influences on structure and function, but further refinement of these techniques is likely required before application in these areas. While brain multi-excitation was investigated in this study

and differences between AP and LR excitations were analyzed, there are possible paths forward for further investigation with more excitations. Though this work uses only AP and LR excitations, investigation of the combination of different excitations may provide a better waveform set for anisotropic parameter estimation with TI-NLI. Another possibility is the inclusion of more waveforms and data sets with TI-NLI and whether this increases the accuracy or repeatability of the parameter estimations. Although this work did not utilize multi-excitation for skeletal muscle parameter estimation due to the extra time needed for acquisition, multi-excitation would likely convey similar benefits in muscle as in brain if able to be deployed sufficiently fast to capture muscle contraction.

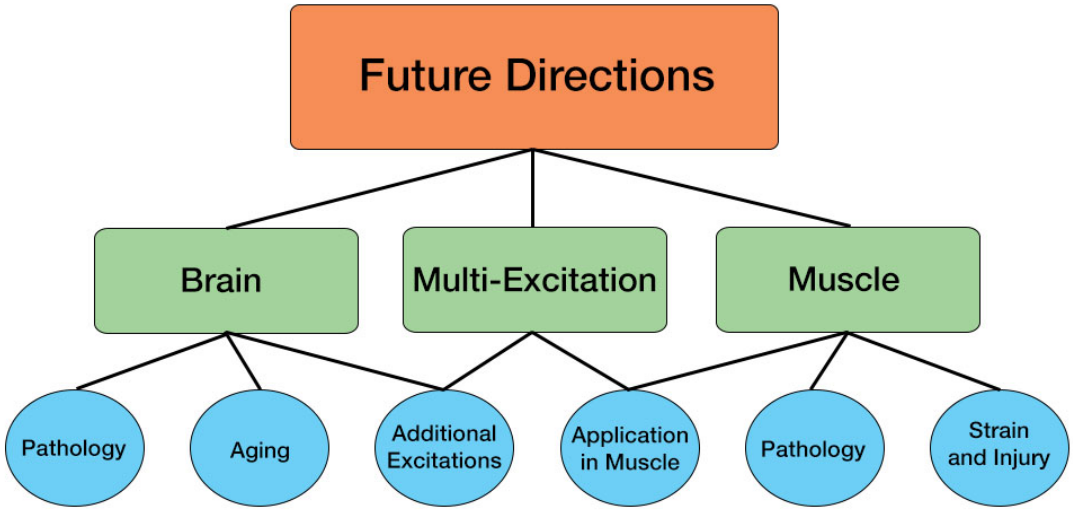

Figure 7.1: The future avenues of this anisotropic MRE research fall under one of three categories: investigation of brain or muscle tissue, or further development of the multiexcitation MRE method, each with their own set of further applications.

As minimal investigation of WM has occurred utilizing MRE for in-vivo estimation of anisotropic viscoelastic parameters, multiple routes of investigation are available for future study. Evaluation of the aging brain and its associated material parameter changes can provide insight into effects of myelination degradation. While the aging brain is an emerging research area for MRE [156,160,217], studies generally employ an isotropic material model, but analyzing WM in aging is now possible due to the anisotropic material model. Investigation of the healthy aging brain also allows for comparison to pathologies common to an older population, such as Alzheimer's disease.

A common approach for understanding how neuropathologies affect brain mechanical properties is through the use of animal models. Rat-based models provide an avenue to evaluate the progression of Alzheimer's disease over a shorter period time with a larger volume of data, as well as providing valuable opportunities for comparison between in-vivo and ex-vivo measurements. By using a rat-based model, future studies could compare MRE measures of WM anisotropy and shear stiffness during disease progression with histology to both confirm disease progression and connect ultrastructural changes with MRE measures. Additionally, similar analysis of other pathologies, including traumatic brain injury and multiple sclerosis, would be other valuable avenues of research for multiexcitation MRE and TI-NLI.

With respect to skeletal muscle, definition of skeletal muscle anisotropic parameters during multiple tension states with MRE creates a framework for future application to characterization of pathology, rehabilitation, and exercise effects. As previously mentioned, pathologies that induce spasticity, such as stroke or CP, resulting in increased extracellular stiffness and longer sarcomeres, as well as lower

active tension outputs. In this work, we have shown that anisotropic MRE can capture variations in both active and passive tension levels and resting stiffness of tissue, making this method ideal for evaluating spastic muscle tissue. Additionally, this technique can be used to monitor these parameters as a subject undergoes various treatment and rehabilitation procedures to assess progress of these procedures through a quantifiable metric of tissue health and function. Similarly, characterization of the effects muscular injury, such as strains or tears, or of injury to adjacent tissues, like ligaments, cartilage, or bone, on the muscle both immediately after and during rehabilitation could provide insight into healthy tissue recovery and an avenue to prevent cascading tissue damage from muscle fibrosis. Characterization in this manner would allow assessment of rehabilitation progress and whether an alternative intervention strategy be required. Another future direction of this work include correlations with other functional measures such as muscle strength and gait mechanics to examine their correlations with anisotropic mechanical properties and functional changes.

7.3 Summary

Overall, this work helps provides a framework for the accurate assessment of fibrous soft tissue health in the human body. Specifically, the technique developed in this work allows researchers to study WM and affecting pathological changes. Additionally, we can now analyze skeletal muscle functional measures for entire muscle groups, such as the calf or forearm muscles, simultaneously.

REFERENCES

[1] Roberts, R. E., Anderson, E. J., and Husain, M., 2013, "White Matter Microstructure and Cognitive Function.," Neuroscientist, **19**(1), pp. 8–15.

[2] Duval, T., Stikov, N., and Cohen-Adad, J., 2016, "Modeling White Matter Microstructure," Funct. Neurol., **31**(4), pp. 217–228.

[3] Gillies, A. R., and Lieber, R. L., 2011, "Structure and Function of the Skeletal Muscle Extracellular Matrix," Muscle Nerve, **44**(3), pp. 318–331.

[4] Frontera, W. R., and Ochala, J., 2015, "Skeletal Muscle: A Brief Review of Structure and Function," Behav. Genet., **45**(2), pp. 183–195.

[5] Hiscox, L. V, Johnson, C. L., Barnhill, E., McGarry, M. D. J., Huston, J., van Beek, E. J. R., Starr, J. M., and Roberts, N., 2016, "Magnetic Resonance Elastography (MRE) of the Human Brain: Technique, Findings and Clinical Applications," Phys. Med. Biol., **61**(24), pp. R401–R437.

[6] Mariappan, Y. K., Glaser, K. J., and Ehman, R. L., 2010, "Magnetic Resonance Elastography: A Review," Clin. Anat., **23**(5), pp. 497–511.

[7] Litwiller, D. V, Mariappan, Y. K., and Ehman, R. L., 2012, "Magnetic Resonance Elastography.," Curr. Med. Imaging Rev., **8**(1), pp. 46–55.

[8] Venkatesh, S. K., Yin, M., and Ehman, R. L., 2013, "Magnetic Resonance Elastography of Liver: Clinical Applications," J. Comput. Assist. Tomogr., **37**(6), p. 887.

[9] Venkatesh, S. K., Yin, M., and Ehman, R. L., 2013, "Magnetic Resonance Elastography of Liver: Technique, Analysis and Clinical Applications," J. Magn. Reson. Imaging, **37**(3), p. 544.

[10] Murphy, M. C., Huston, J., Jack, C. R., Glaser, K. J., Senjem, M. L., Chen, J., Manduca, A., Felmlee, J. P., and Ehman, R. L., 2013, "Measuring the Characteristic Topography of Brain Stiffness with Magnetic Resonance Elastography," PLoS One, **8**(12), p. e81668.

[11] Johnson, C. L., Schwarb, H., D.J. McGarry, M., Anderson, A. T., Huesmann,

G. R., Sutton, B. P., and Cohen, N. J., 2016, "Viscoelasticity of Subcortical Gray Matter Structures," Hum. Brain Mapp., **37**(12), pp. 4221–4233.

[12] Arani, A., Arunachalam, S. P., Chang, I. C. Y., Baffour, F., Rossman, P. J., Glaser, K. J., Trzasko, J. D., McGee, K. P., Manduca, A., Grogan, M., Dispenzieri, A., Ehman, R. L., and Araoz, P. A., 2017, "Cardiac MR Elastography for Quantitative Assessment of Elevated Myocardial Stiffness in Cardiac Amyloidosis," J. Magn. Reson. Imaging, **46**(5), pp. 1361–1367.

[13] Dresner, M. A., Rose, G. H., Rossman, P. J., Muthupillai, R., Manduca, A., and Ehman, R. L., 2001, "Magnetic Resonance Elastography of Skeletal Muscle," J. Magn. Reson. Imaging, **13**(2), pp. 269–276.

[14] Bensamoun, S. F., Charleux, F., Debernard, L., Themar-Noel, C., and Voit, T., 2015, "Elastic Properties of Skeletal Muscle and Subcutaneous Tissues in Duchenne Muscular Dystrophy by Magnetic Resonance Elastography (MRE): A Feasibility Study," IRBM, **36**(1), pp. 4–9.

[15] Oliphant, T. E., Manduca, A., Ehman, R. L., and Greenleaf, J. F., 2001, "Complex-Valued Stiffness Reconstruction for Magnetic Resonance Elastography by Algebraic Inversion of the Differential Equation," Magn. Reson. Med., **45**(2), pp. 299–310.

[16] Manduca, A., Oliphant, T. E., Dresner, M. A., Mahowald, J. L., Kruse, S. A., Amromin, E., Felmlee, J. P., Greenleaf, J. F., and Ehman, R. L., 2001, "Magnetic Resonance Elastography: Non-Invasive Mapping of Tissue Elasticity," Med. Image Anal., **5**(4), pp. 237–254.

[17] Salzer, J. L., and Zalc, B., 2016, "Myelination," Curr. Biol., **26**(20), pp. R971–R975.

[18] Nave, K. A., and Werner, H. B., 2014, "Myelination of the Nervous System: Mechanisms and Functions," Annu. Rev. Cell Dev. Biol., **30**, pp. 503–533.

[19] Stassart, R. M., Möbius, W., Nave, K. A., and Edgar, J. M., 2018, "The Axon-Myelin Unit in Development and Degenerative Disease," Front. Neurosci., **12**(JUL), p. 467.

[20] Weickenmeier, J., De Rooij, R., Budday, S., Ovaert, T. C., and Kuhl, E., 2017, "The Mechanical Importance of Myelination in the Central Nervous System."

[21] McTigue, D. M., and Tripathi, R. B., 2008, "The Life, Death, and Replacement of Oligodendrocytes in the Adult CNS," J. Neurochem., **107**(1), pp. 1–19.

[22] Bradl, M., and Lassmann, H., 2010, "Oligodendrocytes: Biology and Pathology," Acta Neuropathol., **119**, pp. 37–53.

[23] Mesfin, F. B., and Taylor, R. S., 2018, *Diffuse Axonal Injury (DAI)*, StatPearls Publishing.

[24] Färber, K., and Kettenmann, H., 2005, "Physiology of Microglial Cells," Brain Res. Rev., **48**(2), pp. 133–143.

[25] Barron, K. D., 1995, "The Microglial Cell. A Historical Review," J. Neurol. Sci., **134**(SUPPL.), pp. 57–68.

[26] DeKosky, S. T., Ikonomovic, M. D., and Gandy, S., 2010, "Traumatic Brain Injury — Football, Warfare, and Long-Term Effects," N. Engl. J. Med., **363**(14), pp. 1293–1296.

[27] Capizzi, A., Woo, J., and Verduzco-Gutierrez, M., 2020, "Traumatic Brain Injury: An Overview of Epidemiology, Pathophysiology, and Medical Management," Med. Clin., **104**(2), pp. 213–238.

[28] Ramlackhansingh, A. F., Brooks, D. J., Greenwood, R. J., Bose, S. K., Turkheimer, F. E., Kinnunen, K. M., Gentleman, S., Heckemann, R. A., Gunanayagam, K., Gelosa, G., and Sharp, D. J., 2011, "Inflammation after Trauma: Microglial Activation and Traumatic Brain Injury," Ann. Neurol., **70**(3), pp. 374–383.

[29] Donat, C. K., Scott, G., Gentleman, S. M., and Sastre, M., 2017, "Microglial Activation in Traumatic Brain Injury," Front. Aging Neurosci., **9**(JUN), p. 208.

[30] Lye, T. C., and Shores, E. A., 2000, "Traumatic Brain Injury as a Risk Factor for Alzheimer's Disease: A Review," Neuropsychol. Rev. 2000 102, **10**(2), pp. 115–129.

[31] Johnson, V. E., Stewart, W., and Smith, D. H., 2010, "Traumatic Brain Injury and Amyloid-β Pathology: A Link to Alzheimer's Disease?," Nat. Rev. Neurosci. 2010 115, **11**(5), pp. 361–370.

[32] Johnson, V. E., Stewart, J. E., Begbie, F. D., Trojanowski, J. Q., Smith, D. H., and Stewart, W., 2013, "Inflammation and White Matter Degeneration Persist for Years after a Single Traumatic Brain Injury," Brain, **136**(1), pp. 28–42.

[33] Sofroniew, M. V, and Vinters, H. V, 2009, "Astrocytes: Biology and Pathology," Acta Neu, **119**, pp. 7–35.

[34] Dong, Y., and Benveniste, E. N., 2001, “Immune Function of Astrocytes,” Glia, **36**(2), pp. 180–190.

[35] Wenk, G. L., 2003, “Neuropathologic Changes in Alzheimer’s Disease,” J. Clin. Psychiatry, **64**, pp. 7–10.

[36] Goedert, M., and Spillantini, M. G., 2006, “A Century of Alzheimer’s Disease,” Science (80-.)., **314**(5800), pp. 777–781.

[37] Mucke, L., 2009, “Alzheimer’s Disease,” Nature, **461**(7266), pp. 895–897.

[38] Nasrabady, S. E., Rizvi, B., Goldman, J. E., and Brickman, A. M., 2018, “White Matter Changes in Alzheimer’s Disease: A Focus on Myelin and Oligodendrocytes,” Acta Neuropathol. Commun., **6**(1), p. 22.

[39] Bush, A. I., 2003, “The Metallobiology of Alzheimer’s Disease,” Trends Neurosci., **26**(4), pp. 207–214.

[40] Roth, A. D., Ramírez, G., Alarcón, R., and Von Bernhardi, R., 2005, “Oligodendrocytes Damage in Alzheimer’s Disease: Beta Amyloid Toxicity and Inflammation,” Biol. Res., **38**(4), pp. 381–387.

[41] Sospedra, M., and Martin, R., 2004, “Immunology of Multiple Sclerosis,” Annu. Rev. Immunol., **23**, pp. 683–747.

[42] Goldenberg, M. M., 2012, “Multiple Sclerosis Review,” Pharm. Ther., **37**(3), p. 175.

[43] Dobson, R., and Giovannoni, G., 2019, “Multiple Sclerosis – a Review,” Eur. J. Neurol., **26**(1), pp. 27–40.

[44] Witherick, J., Wilkins, A., Scolding, N., and Kemp, K., 2011, “Mechanisms of Oxidative Damage in Multiple Sclerosis and a Cell Therapy Approach to Treatment,” Autoimmune Dis., **1**(1).

[45] Huxley, A. F. ., 1957, “Muscle Structure and Theories of Contraction,” Prog. Biophys. Biophys. Chem., **7**, pp. 255–318.

[46] Gordon, A. M., Huxley, A. F., and Julian, F. J., 1966, “The Variation in Isometric Tension with Sarcomere Length in Vertebrate Muscle Fibres,” J. Physiol., **184**(1), pp. 170–192.

[47] Yiu, E. M., and Kornberg, A. J., 2015, “Duchenne Muscular Dystrophy,” J. Paediatr. Child Health, **51**(8), pp. 759–764.

[48] Deconinck, N., and Dan, B., 2007, “Pathophysiology of Duchenne Muscular Dystrophy: Current Hypotheses,” Pediatr. Neurol., **36**(1), pp. 1–7.

[49] Nakamura, A., and Ichi Takeda, S. ’, 2011, “Mammalian Models of Duchenne Muscular Dystrophy: Pathological Characteristics and Therapeutic Applications,” J. Biomed. Biotechnol., **2011**.

[50] Sciorati, C., Rigamonti, E., Manfredi, A. A., and Rovere-Querini, P., 2016, “Cell Death, Clearance and Immunity in the Skeletal Muscle,” Cell Death Differ., **23**(6), pp. 927–937.

[51] Tharp, C., Mestroni, L., and Taylor, M., 2020, “Modifications of Titin Contribute to the Progression of Cardiomyopathy and Represent a Therapeutic Target for Treatment of Heart Failure,” J. Clin. Med., **9**(9), p. 2770.

[52] Huxley, A. F., 2000, “Cross-Bridge Action: Present Views, Prospects, and Unknowns.,” J. Biomech., **33**(10), pp. 1189–1195.

[53] Herzog, W., Duvall, M., and Leonard, T. R., 2012, “Molecular Mechanisms of Muscle Force Regulation: A Role for Titin?,” Exerc. Sport Sci. Rev., **40**(1), pp. 50–57.

[54] Herzog, W., Powers, K., Johnston, K., and Duvall, M., 2015, “A New Paradigm for Muscle Contraction,” Front. Physiol., **6**(MAY), p. 174.

[55] Lieber, R. L., Roberts, T. J., Blemker, S. S., Lee, S. S. M., and Herzog, W., 2017, “Skeletal Muscle Mechanics, Energetics and Plasticity,” J. Neuroeng. Rehabil., **14**(1), p. 108.

[56] Ter Keurs, H. E. D. J., Iwazumi, T., and Pollack, G. H., 1978, “The Sarcomere Length-Tension Relation in Skeletal Muscle.,” J. Gen. Physiol., **72**(4), pp. 565–592.

[57] Evans, C. L., and Hill, A. V., 1914, “The Relation of Length to Tension Development and Heat Production on Contraction in Muscle,” J. Physiol., **49**(1–2), pp. 10–16.

[58] Kaufman, K. R., An, K. N., and Chao, E. Y. S., 1989, “Incorporation of Muscle Architecture into the Muscle Length-Tension Relationship,” J. Biomech., **22**(8–9), pp. 943–948.

[59] Brughelli, M., and Cronin, J., 2007, *Altering the Length-Tension Relationship with Eccentric Exercise Implications for Performance and Injury*.

[60] Kellis, E., and Baltzopoulos, V., 1998, "Muscle Activation Differences between Eccentric and Concentric Isokinetic Exercise.," Med. Sci. Sports Exerc., **30**(11), pp. 1616–23.

[61] Proske, U., and Morgan, D. L., 2001, "Muscle Damage from Eccentric Exercise: Mechanism, Mechanical Signs, Adaptation and Clinical Applications," J. Physiol., **537**(Pt 2), pp. 333–345.

[62] Vogt, M., and Hoppeler, H. H., 2014, "Eccentric Exercise: Mechanisms and Effects When Used as Training Regime or Training Adjunct," J. Appl. Physiol., **116**(11), pp. 1446–1454.

[63] Butterfield, T. A., 2010, "Eccentric Exercise in Vivo: Strain-Induced Muscle Damage and Adaptation in a Stable System," Exerc. Sport Sci. Rev., **38**(2), pp. 51–60.

[64] Smith, L. R., Lee, K. S., Ward, S. R., Chambers, H. G., and Lieber, R. L., 2011, "Hamstring Contractures in Children with Spastic Cerebral Palsy Result from a Stiffer Extracellular Matrix and Increased in Vivo Sarcomere Length," J. Physiol., **589**(10), pp. 2625–2639.

[65] MacLennan, A. H., Thompson, S. C., and Gecz, J., 2015, "Cerebral Palsy: Causes, Pathways, and the Role of Genetic Variants," Am. J. Obstet. Gynecol., **213**(6), pp. 779–788.

[66] Patel, D. R., Neelakantan, M., Pandher, K., and Merrick, J., 2020, "Cerebral Palsy in Children: A Clinical Overview," Transl. Pediatr., **9**(Suppl 1), p. S125.

[67] Burne, J. A., and Carleton, V. L., 2005, "The Spasticity Paradox: Movement Disorder or Disorder of Resting Limbs?," J Neurol Neurosurg Psychiatry, **76**, pp. 47–54.

[68] Koman, L. A., Smith, B. P., and Balkrishnan, R., 2012, "Spasticity Associated with Cerebral Palsy in Children," Pediatr. Drugs 2003 51, **5**(1), pp. 11–23.

[69] Reilly, R. B., and Lee, T. C., 2010, "Electrograms (ECG, EEG, EMG, EOG)," Technol. Heal. Care, **18**(6), pp. 443–458.

[70] Neil Cuffin, B., and Cohen, D., 1979, "Comparison of the Magnetoencephalogram and Electroencephalogram," Electroencephalogr. Clin. Neurophysiol., **47**(2), pp. 132–146.

[71] Paranjape, R. B., Mahovsky, J., Benedicenti, L., and Koles, Z., 2001, "The Electroencephalogram as a Biometric," Can. Conf. Electr. Comput. Eng., **2**, pp.

1363–1366.

[72] Lindsley, D. B., 1952, "Psychological Phenomena and the Electroencephalogram," Electroencephalogr. Clin. Neurophysiol., **4**(4), pp. 443–456.

[73] Silipo, R., Deco, G., and Bartsch, H., 1999, "Brain Tumor Classification Based on EEG Hidden Dynamics," Intell. Data Anal., **3**(4), pp. 287–306.

[74] Karameh, F. N., and Dahleh, M. A., 2000, "Automated Classification of EEG Signals in Brain Tumor Diagnostics," Proc. Am. Control Conf., **6**, pp. 4169–4173.

[75] Sharanreddy, M., and Kulkarni, P. K., 2013, "Can EEG Test Helps in Identifying Brain Tumor?," Int. J. Heal. Med. Eng., **7**(11), pp. 703–708.

[76] Satterfield, J. H., Lesser, L. I., Saul, R. E., and Cantwell, D. P., 1973, "EEG Aspects in the Diagnosis and Treatment of Minimal Brain Dysfunction," Ann. N. Y. Acad. Sci., **205**(1), pp. 274–282.

[77] Hosokawa, K., Gaspard, N., Su, F., Oddo, M., Vincent, J. L., and Taccone, S. S., 2014, "Clinical Neurophysiological Assessment of Sepsis-Associated Brain Dysfunction: A Systematic Review," Crit. Care, **18**(1), pp. 1–12.

[78] Van Der Stelt, O., and Belger, A., 2007, "Application of Electroencephalography to the Study of Cognitive and Brain Functions in Schizophrenia," Schizophr. Bull., **33**(4), pp. 955–970.

[79] Jordan, K. G., 2004, "Emergency EEG and Continuous EEG Monitoring in Acute Ischemic Stroke," J. Clin. Neurophysiol., **21**(5), pp. 341–352.

[80] Finnigan, S., and van Putten, M. J. A. M., 2013, "EEG in Ischaemic Stroke: Quantitative EEG Can Uniquely Inform (Sub-)Acute Prognoses and Clinical Management," Clin. Neurophysiol., **124**(1), pp. 10–19.

[81] Wu, J., Srinivasan, R., Quinlan, E. B., Solodkin, A., Small, S. L., and Cramer, S. C., 2016, "Utility of EEG Measures of Brain Function in Patients with Acute Stroke," J. Neurophysiol., **115**(5), pp. 2399–2405.

[82] Blackburn, H., Keys, A., Simonson, E., Rautaharju, P., and Punsar, S., 1960, "The Electrocardiogram in Population Studies," Circulation, **21**, pp. 1160–1175.

[83] Geselowitz, D. B., 1989, "On the Theory of the Electrocardiogram," Proc.

IEEE, **77**(6), pp. 857–876.

[84] McSharry, P. E., Clifford, G. D., Tarassenko, L., and Smith, L. A., 2003, "A Dynamical Model for Generating Synthetic Electrocardiogram Signals," IEEE Trans. Biomed. Eng., **50**(3), pp. 289–294.

[85] Zimetbaum, P. J., and Josephson, M. E., 2009, "Use of the Electrocardiogram in Acute Myocardial Infarction," http://dx.doi.org/10.1056/NEJMra022700, **348**(10), pp. 933–940.

[86] Ramanathan, C., Ghanem, R. N., Jia, P., Ryu, K., and Rudy, Y., 2004, "Noninvasive Electrocardiographic Imaging for Cardiac Electrophysiology and Arrhythmia," Nat. Med. 2004 104, **10**(4), pp. 422–428.

[87] Yang, J., Bai, Y., Lin, F., Liu, M., Hou, Z., and Liu, X., 2018, "A Novel Electrocardiogram Arrhythmia Classification Method Based on Stacked Sparse Auto-Encoders and Softmax Regression," Int. J. Mach. Learn. Cybern., **9**(10), pp. 1733–1740.

[88] Simonson, E., 1972, "The Effect of Age on the Electrocardiogram," Am. J. Cardiol., **29**(1), pp. 64–73.

[89] Hewson, D. J., Hogrel, J. Y., Langeron, Y., and Duchêne, J., 2003, "Evolution in Impedance at the Electrode-Skin Interface of Two Types of Surface EMG Electrodes during Long-Term Recordings," J. Electromyogr. Kinesiol., **13**(3), pp. 273–279.

[90] Murphy, B. B., Scheid, B. H., Hendricks, Q., Apollo, N. V., Litt, B., and Vitale, F., 2021, "Time Evolution of the Skin-Electrode Interface Impedance under Different Skin Treatments," Sensors (Basel)., **21**(15).

[91] De Luca, C. J., 1997, "The Use of Surface Electromyography in Biomechanics," J. Appl. Biomech., **13**(2), pp. 135–163.

[92] Tassinary, L. G., Cacioppo, J. T., and Vanman, E. J., 2009, "The Skeletomotor System: Surface Electromyography," Handb. Psychophysiol., pp. 267–300.

[93] Mills, K. R., 2005, "The Basics of Electromyography," J. Neurol. Neurosurg. Psychiatry, **76**(suppl 2), pp. ii32–ii35.

[94] Luca, C. De, 2006, "Electromyography," Encycl. Med. Devices Instrum.

[95] Polasek, K. H., Schiefer, M. A., Pinault, G. C. J., Triolo, R. J., and Tyler, D. J., 2009, "Intraoperative Evaluation of the Spiral Nerve Cuff Electrode on the

Femoral Nerve Trunk," J. Neural Eng., **6**(6).

[96] Komi, P. V., and Viitasalo, J. H. T., 1976, "Signal Characteristics of EMG at Different Levels of Muscle Tension," Acta Physiol. Scand., **96**(2), pp. 267–276.

[97] Perry, J., and Hoffer, M. M., 1977, "Preoperative and Postoperative Dynamic Electromyography as an Aid in Planning Tendon Transfers in Children with Cerebral Palsy.," J. Bone Joint Surg. Am., **59**(4), pp. 531–537.

[98] Hoffer, M. M., Perry, J., and Melkonian, G. J., 1979, "Dynamic Electromyography and Decision-Making for Surgery in the Upper Extremity of Patients with Cerebral Palsy," J. Hand Surg. Am., **4**(5), pp. 424–431.

[99] Lauer, R. T., Smith, B. T., and Betz, R. R., 2005, "Application of a Neuro-Fuzzy Network for Gait Event Detection Using Electromyography in the Child with Cerebral Palsy," IEEE Trans. Biomed. Eng., **52**(9), pp. 1532–1540.

[100] Shuman, B. R., Schwartz, M. H., and Steele, K. M., 2017, "Electromyography Data Processing Impacts Muscle Synergies during Gait for Unimpaired Children and Children with Cerebral Palsy," Front. Comput. Neurosci., **11**, p. 50.

[101] Kubelberg, E., 1949, "Electromyography in Muscular Dystrophies: Differentiation between Dystrophies and Chronic Lower Motor Neurone Lesions," J. Neurol. Neurosurg. Psychiatry, **12**(2), p. 129.

[102] Hilton-Brown, P., and Stålberg, E., 1983, "Motor Unit Size in Muscular Dystrophy, a Macro EMG and Scanning EMG Study.," J. Neurol. Neurosurg. Psychiatry, **46**(11), pp. 996–1005.

[103] Parker, K. J., Doyley, M. M., and Rubens, D. J., 2006, "Ultrasound Imaging," Phys. Med. Biol., **51**(13), p. R83.

[104] Aldrich, J. E., 2007, "Basic Physics of Ultrasound Imaging," Crit. Care Med., **35**(5 SUPPL.).

[105] Ihnatsenka, B., and Boezaart, A. P., 2010, "Ultrasound: Basic Understanding and Learning the Language," Int. J. Shoulder Surg., **4**(3), p. 55.

[106] Chan, V., and Perlas, A., 2011, "Basics of Ultrasound Imaging," Atlas Ultrasound-Guided Proced. Interv. Pain Manag., pp. 13–19.

[107] Routh, H. F., 1996, "Doppler Ultrasound," IEEE Eng. Med. Biol. Mag., **15**(6), pp. 31–40.

[108] Rådegran, G., 1999, "Limb and Skeletal Muscle Blood Flow Measurements at Rest and during Exercise in Human Subjects," Proc. Nutr. Soc., **58**(4), pp. 887–898.

[109] Bangalore-yogananda, C., Rosenberry, R., Soni, S., Liu, H., Nelson, M. D., Tian, F., Blair, S. N., Kohl, H. W., Barlow, C. E., Paffenbarger, R. S., Gibbons, L. W., Macera, C. A., Clark, D. G., Cooper, K. H., Paterson, D. H., Govindasamy, D., Vidmar, M., Cunningham, D. A., Koval, J. J., Yu, G., Floyd, T. F., Durduran, T., Zhou, C., Wang, J., Detre, J. A., and Yodh, A. G., 2018, "Concurrent Measurement of Skeletal Muscle Blood Flow during Exercise with Diffuse Correlation Spectroscopy and Doppler Ultrasound," Biomed. Opt. Express, Vol. 9, Issue 1, pp. 131-141, **9**(1), pp. 131–141.

[110] Elvin, A., Siösteen, A. K., Nilsson, A., and Kosek, E., 2006, "Decreased Muscle Blood Flow in Fibromyalgia Patients during Standardised Muscle Exercise: A Contrast Media Enhanced Colour Doppler Study," Eur. J. Pain, **10**(2), pp. 137–144.

[111] Basford, J. R., and An, K. N., 2009, "New Techniques for the Quantification of Fibromyalgia and Myofascial Pain," Curr. Pain Headache Reports 2009 135, **13**(5), pp. 376–378.

[112] Gharbi, H. A., Hassine, W., Brauner, M. W., and Dupuch, K., 1981, "Ultrasound Examination of the Hydatic Liver.," Radiology, **139**(2), pp. 459–463.

[113] Harvey, C. J., and Albrecht, T., 2001, "Ultrasound of Focal Liver Lesions," Eur. Radiol. 2001 119, **11**(9), pp. 1578–1593.

[114] Williams, C. D., Stengel, J., Asike, M. I., Torres, D. M., Shaw, J., Contreras, M., Landt, C. L., and Harrison, S. A., 2011, "Prevalence of Nonalcoholic Fatty Liver Disease and Nonalcoholic Steatohepatitis Among a Largely Middle-Aged Population Utilizing Ultrasound and Liver Biopsy: A Prospective Study," Gastroenterology, **140**(1), pp. 124–131.

[115] Frulio, N., and Trillaud, H., 2013, "Ultrasound Elastography in Liver," Diagn. Interv. Imaging, **94**(5), pp. 515–534.

[116] Goddi, A., Bonardi, M., and Alessi, S., 2012, "Breast Elastography: A Literature Review," J. Ultrasound, **15**(3), pp. 192–198.

[117] Balleyguier, C., Ciolovan, L., Ammari, S., Canale, S., Sethom, S., Al Rouhbane, R., Vielh, P., and Dromain, C., 2013, "Breast Elastography: The Technical Process and Its Applications," Diagn. Interv. Imaging, **94**(5), pp.

503–513.

[118] Rago, T., Santini, F., Scutari, M., Pinchera, A., and Vitti, P., 2007, "Elastography: New Developments in Ultrasound for Predicting Malignancy in Thyroid Nodules," J. Clin. Endocrinol. Metab., **92**(8), pp. 2917–2922.

[119] Kwak, J. Y., and Kim, E. K., 2014, "Ultrasound Elastography for Thyroid Nodules: Recent Advances," Ultrasonography, **33**(2), p. 75.

[120] Correas, J. M., Tissier, A. M., Khairoune, A., Khoury, G., Eiss, D., and Hélénon, O., 2013, "Ultrasound Elastography of the Prostate: State of the Art," Diagn. Interv. Imaging, **94**(5), pp. 551–560.

[121] Sigrist, R. M. S., Liau, J., Kaffas, A. El, Chammas, M. C., Willmann, J. K., and Willmann, J. K., 2017, "Ultrasound Elastography: Review of Techniques and Clinical Applications," Theranostics, **7**(5), pp. 1303–1329.

[122] Tanter, M., Pernot, M., Gennisson, J. L., and Fink, M., 2013, "A Review of the Medical Applications of Shear Wave Elastography," J. Acoust. Soc. Am., **134**(5), p. 4009.

[123] Cosgrove, D. O., Berg, W. A., Doré, C. J., Skyba, D. M., Henry, J. P., Gay, J., and Cohen-Bacrie, C., 2012, "Shear Wave Elastography for Breast Masses Is Highly Reproducible," Eur. Radiol., **22**(5), pp. 1023–1032.

[124] Taljanovic, M. S., Gimber, L. H., Becker, G. W., Latt, L. D., Klauser, A. S., Melville, D. M., Gao, L., and Witte, R. S., 2017, "Shear-Wave Elastography: Basic Physics and Musculoskeletal," Radiographics, **37**(3), p. 855.

[125] Eby, S. F., Song, P., Chen, S., Chen, Q., Greenleaf, J. F., and An, K. N., 2013, "Validation of Shear Wave Elastography in Skeletal Muscle," J. Biomech., **46**(14), pp. 2381–2387.

[126] Eby, S. F., Cloud, B. A., Brandenburg, J. E., Giambini, H., Song, P., Chen, S., Lebrasseur, N. K., and An, K. N., 2015, "Shear Wave Elastography of Passive Skeletal Muscle Stiffness: Influences of Sex and Age throughout Adulthood," Clin. Biomech., **30**(1), pp. 22–27.

[127] Wu, C. H., Ho, Y. C., Hsiao, M. Y., Chen, W. S., and Wang, T. G., 2017, "Evaluation of Post-Stroke Spastic Muscle Stiffness Using Shear Wave Ultrasound Elastography," Ultrasound Med. Biol., **43**(6), pp. 1105–1111.

[128] Tsuchida, W., Yamakoshi, Y., Matsuo, S., Asakawa, M., Sugahara, K., Fukaya, T., Yamanaka, E., Asai, Y., Nitta, N., Ooie, T., and Suzuki, S., 2020,

"Application of the Novel Estimation Method by Shear Wave Elastography Using Vibrator to Human Skeletal Muscle," Sci. Reports 2020 101, **10**(1), pp. 1–10.

[129] Nakayama, R., Takaya, Y., Nakamura, K., Toh, N., and Ito, H., 2021, "Efficacy of Shear Wave Elastography for Assessment of Liver Function in Patients with Heart Failure," ESC Hear. Fail., **8**(3), pp. 1751–1758.

[130] Pykett, I. L., Newhouse, J. H., Buonanno, F. S., Brady, T. J., Goldman, M. R., Kistler, J. P., and Pohost, G. M., 1982, "Principles of Nuclear Magnetic Resonance Imaging.," Radiology, **143**(1), pp. 157–168.

[131] Liang, Z.-P., and Lauterbur, P. C., 2000, *Principles of Magnetic Resonance Imaging*.

[132] Vlaardingerbroek, M., and Boer, J., 2013, *Magnetic Resonance Imaging: Theory and Practice*.

[133] Brown, R., Cheng, Y., Haacke, E., and Thompson, M., 2014, *Magnetic Resonance Imaging: Physical Principles and Sequence Design*.

[134] Damon, B. M., Ding, Z., Anderson, A. W., Freyer, A. S., and Gore, J. C., 2002, "Validation of Diffusion Tensor MRI-Based Muscle Fiber Tracking," Magn. Reson. Med., **48**(1), pp. 97–104.

[135] Le Bihan, D., 2003, "Looking into the Functional Architecture of the Brain with Diffusion MRI," Nat. Rev. Neurosci. 2003 46, **4**(6), pp. 469–480.

[136] Pfefferbaum, A., Adalsteinsson, E., and Sullivan, E. V., 2003, "Replicability of Diffusion Tensor Imaging Measurements of Fractional Anisotropy and Trace in Brain," J. Magn. Reson. Imaging, **18**(4), pp. 427–433.

[137] Grieve, S. M., Williams, L. M., Paul, R. H., Clark, C. R., and Gordon, E., 2007, "Cognitive Aging, Executive Function, and Fractional Anisotropy: A Diffusion Tensor MR Imaging Study," Am. J. Neuroradiol., **28**(2), pp. 226–235.

[138] Kochunov, P., Williamson, D. E., Lancaster, J., Fox, P., Cornell, J., Blangero, J., and Glahn, D. C., 2012, "Fractional Anisotropy of Water Diffusion in Cerebral White Matter across the Lifespan," Neurobiol. Aging, **33**(1), pp. 9–20.

[139] Schwenzer, N. F., Steidle, G., Martirosian, P., Schraml, C., Springer, F., Claussen, C. D., and Schick, F., 2009, "Diffusion Tensor Imaging of the Human Calf Muscle: Distinct Changes in Fractional Anisotropy and Mean Diffusion Due to Passive Muscle Shortening and Stretching," NMR Biomed., **22**(10), p.

n/a-n/a.

[140] Heemskerk, A. M., Sinha, T. K., Wilson, K. J., Ding, Z., and Damon, B. M., 2009, "Quantitative Assessment of DTI-Based Muscle Fiber Tracking and Optimal Tracking Parameters," Magn. Reson. Med., **61**(2), pp. 467–472.

[141] Bolsterlee, B., D'Souza, A., Gandevia, S. C., and Herbert, R. D., 2017, "How Does Passive Lengthening Change the Architecture of the Human Medial Gastrocnemius Muscle?," J. Appl. Physiol., **122**(4), pp. 727–738.

[142] Ponrartana, S., Ramos-Platt, L., Wren, T. A. L., Hu, H. H., Perkins, T. G., Chia, J. M., and Gilsanz, V., 2015, "Effectiveness of Diffusion Tensor Imaging in Assessing Disease Severity in Duchenne Muscular Dystrophy: Preliminary Study," Pediatr. Radiol., **45**(4), pp. 582–589.

[143] Li, G. D., Liang, Y. Y., Xu, P., Ling, J., and Chen, Y. M., 2016, "Diffusion-Tensor Imaging of Thigh Muscles in Duchenne Muscular Dystrophy: Correlation of Apparent Diffusion Coefficient and Fractional Anisotropy Values With Fatty Infiltration," Am. J. Roentgenol., **206**(4), pp. 867–870.

[144] Kennedy, K. M., and Raz, N., 2009, "Aging White Matter and Cognition: Differential Effects of Regional Variations in Diffusion Properties on Memory, Executive Functions, and Speed," Neuropsychologia, **47**(3), pp. 916–927.

[145] Madden, D. J., Bennett, I. J., and Song, A. W., 2009, "Cerebral White Matter Integrity and Cognitive Aging: Contributions from Diffusion Tensor Imaging," Neuropsychol. Rev., **19**, pp. 415–435.

[146] Madden, D. J., Bennett, I. J., Burzynska, A., Potter, G. G., Chen, N. kuei, and Song, A. W., 2012, "Diffusion Tensor Imaging of Cerebral White Matter Integrity in Cognitive Aging," Biochim. Biophys. Acta - Mol. Basis Dis., **1822**(3), pp. 386–400.

[147] Gross, D. W., Concha, L., and Beaulieu, C., 2006, "Extratemporal White Matter Abnormalities in Mesial Temporal Lobe Epilepsy Demonstrated with Diffusion Tensor Imaging," Epilepsia, **47**(8), pp. 1360–1363.

[148] Concha, L., Beaulieu, C., Collins, D. L., and Gross, D. W., 2009, "White-Matter Diffusion Abnormalities in Temporal-Lobe Epilepsy with and without Mesial Temporal Sclerosis," J. Neurol. Neurosurg. Psychiatry, **80**(3), pp. 312–319.

[149] Bozzali, M., Falini, A., Franceschi, M., Cercignani, M., Zuffi, M., Scotti, G., Comi, G., and Filippi, M., 2002, "White Matter Damage in Alzheimer's

Disease Assessed in Vivo Using Diffusion Tensor Magnetic Resonance Imaging," J. Neurol. Neurosurg. Psychiatry, **72**(6), pp. 742–746.

[150] Acosta-Cabronero, J., Williams, G. B., Pengas, G., and Nestor, P. J., 2010, "Absolute Diffusivities Define the Landscape of White Matter Degeneration in Alzheimer's Disease," Brain, **133**(2), pp. 529–539.

[151] Albensi, B. C., Knoblach, S. M., Chew, B. G. M., O'Reilly, M. P., Faden, A. I., and Pekar, J. J., 2000, "Diffusion and High Resolution MRI of Traumatic Brain Injury in Rats: Time Course and Correlation with Histology," Exp. Neurol., **162**(1), pp. 61–72.

[152] Rutgers, D. R., Fillard, P., Paradot, G., Tadié, M., Lasjaunias, P., and Ducreux, D., 2008, "Diffusion Tensor Imaging Characteristics of the Corpus Callosum in Mild, Moderate, and Severe Traumatic Brain Injury," Am. J. Neuroradiol., **29**(9), pp. 1730–1735.

[153] Assaf, Y., and Pasternak, O., 2008, "Diffusion Tensor Imaging (DTI)-Based White Matter Mapping in Brain Research: A Review," J. Mol. Neurosci., **34**(1), pp. 51–61.

[154] Kruse, S. A., Smith, J. A., Lawrence, A. J., Dresner, M. A., Manduca, A., Greenleaf, J. F., and Ehman, R. L., 2000, "Tissue Characterization Using Magnetic Resonance Elastography: Preliminary Results," Phys. Med. Biol., **45**(6), pp. 1579–1590.

[155] Venkatesh, S. K., Yin, M., Glockner, J. F., Takahashi, N., Araoz, P. A., Talwalkar, J. A., and Ehman, R. L., 2008, "MR Elastography of Liver Tumors: Preliminary Results," Am. J. Roentgenol., **190**(6), pp. 1534–1540.

[156] Hiscox, L. V., Johnson, C. L., McGarry, M. D. J., Perrins, M., Littlejohn, A., van Beek, E. J. R., Roberts, N., and Starr, J. M., 2018, "High-Resolution Magnetic Resonance Elastography Reveals Differences in Subcortical Gray Matter Viscoelasticity between Young and Healthy Older Adults," Neurobiol. Aging, **65**, pp. 158–167.

[157] McIlvain, G., Clements, R. G., Magoon, E. M., Spielberg, J. M., Telzer, E. H., and Johnson, C. L., 2020, "Viscoelasticity of Reward and Control Systems in Adolescent Risk Taking," Neuroimage, **215**, p. 116850.

[158] Murphy, M. C., Huston, J., and Ehman, R. L., 2019, "MR Elastography of the Brain and Its Application in Neurological Diseases," Neuroimage, **187**(August 2017), pp. 176–183.

[159] Gnanago, J. L., Capsal, J. F., Gerges, T., Lombard, P., Semet, V., Cottinet, P. J., Cabrera, M., and Lambert, S. A., 2021, "Actuators for MRE: New Perspectives With Flexible Electroactive Materials," Front. Phys., **9**, p. 580.

[160] Delgorio, P. L., Hiscox, L. V, Daugherty, A. M., Sanjana, F., Pohlig, R. T., Ellison, J. M., Martens, C. R., Schwarb, H., McGarry, M. D. J., and Johnson, C. L., 2021, "Effect of Aging on the Viscoelastic Properties of Hippocampal Subfields Assessed with High-Resolution MR Elastography," Cereb. Cortex, pp. 1–13.

[161] Chaze, C. A., McIlvain, G., Smith, D. R., Villermaux, G. M., Delgorio, P. L., Wright, H. G., Rogers, K. J., Miller, F., Crenshaw, J. R., and Johnson, C. L., 2019, "Altered Brain Tissue Viscoelasticity in Pediatric Cerebral Palsy Measured by Magnetic Resonance Elastography," NeuroImage Clin., **22**.

[162] Venkatesh, S. K., and Ehman, R. L., 2014, "Magnetic Resonance Elastography of Liver," Magn. Reson. Imaging Clin., **22**(3), pp. 433–446.

[163] McGarry, M. D. J., Van Houten, E. E. W., Johnson, C. L., Georgiadis, J. G., Sutton, B. P., Weaver, J. B., and Paulsen, K. D., 2012, "Multiresolution MR Elastography Using Nonlinear Inversion," Med. Phys., **39**(10), pp. 6388–6396.

[164] Van Houten, E. E. W., Doyley, M. M., Kennedy, F. E., Weaver, J. B., and Paulsen, K. D., 2003, "Initial in Vivo Experience with Steady-State Subzone-Based MR Elastography of the Human Breast," J. Magn. Reson. Imaging, **17**(1), pp. 72–85.

[165] Sinkus, R., Tanter, M., Catheline, S., Lorenzen, J., Kuhl, C., Sondermann, E., and Fink, M., 2005, "Imaging Anisotropic and Viscous Properties of Breast Tissue by Magnetic Resonance-Elastography," Magn. Reson. Med., **53**(2), pp. 372–387.

[166] Green, M. A., Geng, G., Qin, E., Sinkus, R., Gandevia, S. C., and Bilston, L. E., 2013, "Measuring Anisotropic Muscle Stiffness Properties Using Elastography," NMR Biomed., **26**(11), pp. 1387–1394.

[167] Romano, A., Scheel, M., Hirsch, S., Braun, J., and Sack, I., 2012, "In Vivo Waveguide Elastography of White Matter Tracts in the Human Brain," Magn. Reson. Med., **68**(5), pp. 1410–1422.

[168] Tweten, D. J. D. J., Okamoto, R. J., Schmidt, J. L., Garbow, J. R., and Bayly, P. V., 2015, "Estimation of Material Parameters from Slow and Fast Shear Waves in an Incompressible, Transversely Isotropic Material," J. Biomech., **48**(15), pp. 4002–4009.

[169] Guo, J., Hirsch, S., Scheel, M., Braun, J., and Sack, I., 2016, "Three-Parameter Shear Wave Inversion in MR Elastography of Incompressible Transverse Isotropic Media: Application to in Vivo Lower Leg Muscles," Magn. Reson. Med., **75**(4), pp. 1537–1545.

[170] Braun, J., Guo, J., Lützkendorf, R., Stadler, J., Papazoglou, S., Hirsch, S., Sack, I., and Bernarding, J., 2014, "High-Resolution Mechanical Imaging of the Human Brain by Three-Dimensional Multifrequency Magnetic Resonance Elastography at 7T," Neuroimage, **90**, pp. 308–314.

[171] Reiss-Zimmermann, M., Streitberger, K. J., Sack, I., Braun, J., Arlt, F., Fritzsch, D., and Hoffmann, K. T., 2015, "High Resolution Imaging of Viscoelastic Properties of Intracranial Tumours by Multi-Frequency Magnetic Resonance Elastography," Clin. Neuroradiol., **25**(4), pp. 371–378.

[172] Barnhill, E., Hollis, L., Sack, I., Braun, J., Hoskins, P. R., Pankaj, P., Brown, C., van Beek, E. J. R., and Roberts, N., 2017, "Nonlinear Multiscale Regularisation in MR Elastography: Towards Fine Feature Mapping," Med. Image Anal., **35**, pp. 133–145.

[173] Anderson, A. T., Van Houten, E. E. W., McGarry, M. D. J., Paulsen, K. D., Holtrop, J. L., Sutton, B. P., Georgiadis, J. G., and Johnson, C. L., 2016, "Observation of Direction-Dependent Mechanical Properties in the Human Brain with Multi-Excitation MR Elastography," J. Mech. Behav. Biomed. Mater., **59**, pp. 538–546.

[174] Aoki, Y., Inokuchi, R., Gunshin, M., Yahagi, N., and Suwa, H., 2012, "Diffusion Tensor Imaging Studies of Mild Traumatic Brain Injury: A Meta-Analysis," J. Neurol. Neurosurg. Psychiatry, **83**(9), pp. 870–876.

[175] Wozniak, J. R., Krach, L., Ward, E., Mueller, B. A., Muetzel, R., Schnoebelen, S., Kiragu, A., and Lim, K. O., 2007, "Neurocognitive and Neuroimaging Correlates of Pediatric Traumatic Brain Injury: A Diffusion Tensor Imaging (DTI) Study," Arch. Clin. Neuropsychol., **22**(5), pp. 555–568.

[176] Niogi, S. N., Mukherjee, P., Ghajar, J., Johnson, C., Kolster, R. A., Sarkar, R., Lee, H., Meeker, M., Zimmerman, R. D., Manley, G. T., and McCandliss, B. D., 2008, "Extent of Microstructural White Matter Injury in Postconcussive Syndrome Correlates with Impaired Cognitive Reaction Time: A 3T Diffusion Tensor Imaging Study of Mild Traumatic Brain Injury," Am. J. Neuroradiol., **29**(5), pp. 967–973.

[177] Muthupillai, R., Lomas, D. J., Rossman, P. J., Greenleaf, J. F., Manduca, A., and Ehman, R. L., 1995, "Magnetic Resonance Elastography by Direct

Visualization of Propagating Acoustic Strain Waves.," Science, **269**(5232), pp. 1854–7.

[178] Manduca, A., Oliphant, T. E. E., Dresner, M. A. A., Mahowald, J. L. L., Kruse, S. A. A., Amromin, E., Felmlee, J. P. P., Greenleaf, J. F. F., and Ehman, R. L. L., 2001, "Magnetic Resonance Elastography: Non-Invasive Mapping of Tissue Elasticity," Med. Image Anal., **5**(4), pp. 237–254.

[179] Sack, I., Beierbach, B., Hamhaber, U., Klatt, D., and Braun, J., 2008, "Non-Invasive Measurement of Brain Viscoelasticity Using Magnetic Resonance Elastography," NMR Biomed., **21**(3), pp. 265–271.

[180] Sandroff, B. M., Johnson, C. L., and Motl, R. W., 2017, "Exercise Training Effects on Memory and Hippocampal Viscoelasticity in Multiple Sclerosis: A Novel Application of Magnetic Resonance Elastography," Neuroradiology, **59**(1), pp. 61–67.

[181] Streitberger, K.-J., Sack, I., Krefting, D., Pfüller, C., Braun, J., Paul, F., and Wuerfel, J., 2012, "Brain Viscoelasticity Alteration in Chronic-Progressive Multiple Sclerosis," PLoS One, **7**(1), p. e29888.

[182] Wuerfel, J., Paul, F., Beierbach, B., Hamhaber, U., Klatt, D., Papazoglou, S., Zipp, F., Martus, P., Braun, J., and Sack, I., 2010, "MR-Elastography Reveals Degradation of Tissue Integrity in Multiple Sclerosis," Neuroimage, **49**(3), pp. 2520–2525.

[183] Murphy, M. C., Curran, G. L., Glaser, K. J., Rossman, P. J., Huston, J., Poduslo, J. F., Jack, C. R., Felmlee, J. P., and Ehman, R. L., 2012, "Magnetic Resonance Elastography of the Brain in a Mouse Model of Alzheimer's Disease: Initial Results," Magn. Reson. Imaging, **30**(4), pp. 535–539.

[184] Murphy, M. C., Huston, J., Jack, C. R., Glaser, K. J., Manduca, A., Felmlee, J. P., and Ehman, R. L., 2011, "Decreased Brain Stiffness in Alzheimer's Disease Determined by Magnetic Resonance Elastography," J. Magn. Reson. Imaging, **34**(3), pp. 494–498.

[185] Lipp, A., Trbojevic, R., Paul, F., Fehlner, A., Hirsch, S., Scheel, M., Noack, C., Braun, J., and Sack, I., 2013, "Cerebral Magnetic Resonance Elastography in Supranuclear Palsy and Idiopathic Parkinson's Disease," NeuroImage Clin., **3**, pp. 381–387.

[186] Schregel, K., Wuerfel, E., Garteiser, P., Gemeinhardt, I., Prozorovski, T., Aktas, O., Merz, H., Petersen, D., Wuerfel, J., and Sinkus, R., 2012, "Demyelination Reduces Brain Parenchymal Stiffness Quantified in Vivo by

Magnetic Resonance Elastography.," Proc. Natl. Acad. Sci. U. S. A., **109**(17), pp. 6650–5.

[187] Weickenmeier, J., de Rooij, R., Budday, S., Steinmann, P., Ovaert, T. C., and Kuhl, E., 2016, "Brain Stiffness Increases with Myelin Content," Acta Biomater., **42**, pp. 265–272.

[188] Feng, Y., Okamoto, R. J., Namani, R., Genin, G. M., and Bayly, P. V., 2013, "Measurements of Mechanical Anisotropy in Brain Tissue and Implications for Transversely Isotropic Material Models of White Matter," J. Mech. Behav. Biomed. Mater., **23**, pp. 117–132.

[189] Feng, Y., Okamoto, R. J., Genin, G. M., and Bayly, P. V, 2016, "On the Accuracy and Fitting of Transversely Isotropic Material Models," J. Mech. Behav. Biomed. Mater., **61**, pp. 554–566.

[190] Feng, Y., Lee, C.-H., Sun, L., Ji, S., and Zhao, X., 2017, "Characterizing White Matter Tissue in Large Strain via Asymmetric Indentation and Inverse Finite Element Modeling," J. Mech. Behav. Biomed. Mater., **65**, pp. 490–501.

[191] Feng, Y., Qiu, S., Xia, X., Ji, S., and Lee, C.-H., 2017, "A Computational Study of Invariant I5 in a Nearly Incompressible Transversely Isotropic Model for White Matter," J. Biomech., **57**, pp. 146–151.

[192] Schmidt, J. L., Tweten, D. J., Badachhape, A. A., Reiter, A. J., Okamoto, R. J., Garbow, J. R., and Bayly, P. V., 2018, "Measurement of Anisotropic Mechanical Properties in Porcine Brain White Matter Ex Vivo Using Magnetic Resonance Elastography," J. Mech. Behav. Biomed. Mater., **79**, pp. 30–37.

[193] Feng, Y., Clayton, E. H., Chang, Y., Okamoto, R. J., and Bayly, P. V., 2013, "Viscoelastic Properties of the Ferret Brain Measured in Vivo at Multiple Frequencies by Magnetic Resonance Elastography," J. Biomech., **46**(5), pp. 863–870.

[194] Schmidt, J. L., Tweten, D. J., Benegal, A. N., Walker, C. H., Portnoi, T. E., Okamoto, R. J., Garbow, J. R., and Bayly, P. V., 2016, "Magnetic Resonance Elastography of Slow and Fast Shear Waves Illuminates Differences in Shear and Tensile Moduli in Anisotropic Tissue," J. Biomech., **49**(7), pp. 1042–1049.

[195] Romano, A., Guo, J., Prokscha, T., Meyer, T., Hirsch, S., Braun, J., Sack, I., and Scheel, M., 2014, "In Vivo Waveguide Elastography: Effects of Neurodegeneration in Patients with Amyotrophic Lateral Sclerosis," Magn. Reson. Med., **72**(6), pp. 1755–1761.

[196] Tweten, D. J., Okamoto, R. J., and Bayly, P. V., 2017, "Requirements for Accurate Estimation of Anisotropic Material Parameters by Magnetic Resonance Elastography: A Computational Study," Magn. Reson. Med., **78**(6), pp. 2360–2372.

[197] Manduca, A., Lake, D. S., Kruse, S. A., and Ehman, R. L., 2003, "Spatio-Temporal Directional Filtering for Improved Inversion of MR Elastography Images," Med. Image Anal., **7**(4), pp. 465–473.

[198] Clayton, E. H., Genin, G. M., and Bayly, P. V, 2012, "Transmission, Attenuation and Reflection of Shear Waves in the Human Brain.," J. R. Soc. Interface, **9**(76), pp. 2899–910.

[199] Okamoto, R. J., Romano, A. J., Johnson, C. L., and Bayly, P. V, 2019, "Insights Into Traumatic Brain Injury From MRI of Harmonic Brain Motion," J. Exp. Neurosci., **13**, p. 117906951984044.

[200] Okamoto, R. J., Clayton, E. H., and Bayly, P. V, 2011, "Viscoelastic Properties of Soft Gels: Comparison of Magnetic Resonance Elastography and Dynamic Shear Testing in the Shear Wave Regime," Phys. Med. Biol., **56**(19), pp. 6379–6400.

[201] Smith, S. M., Jenkinson, M., Woolrich, M. W., Beckmann, C. F., Behrens, T. E. J., Johansen-Berg, H., Bannister, P. R., De Luca, M., Drobnjak, I., Flitney, D. E., Niazy, R. K., Saunders, J., Vickers, J., Zhang, Y., De Stefano, N., Brady, J. M., and Matthews, P. M., 2004, "Advances in Functional and Structural MR Image Analysis and Implementation as FSL," Neuroimage, **23 Suppl 1**(SUPPL. 1).

[202] Jenkinson, M., Beckmann, C. F., Behrens, T. E. J. J., Woolrich, M. W., and Smith, S. M., 2012, "Fsl.," Neuroimage, **62**(2), pp. 782–90.

[203] Mori, S., Oishi, K., Jiang, H., Jiang, L., Li, X., Akhter, K., Hua, K., Faria, A. V., Mahmood, A., Woods, R., Toga, A. W., Pike, G. B., Neto, P. R., Evans, A., Zhang, J., Huang, H., Miller, M. I., van Zijl, P., and Mazziotta, J., 2008, "Stereotaxic White Matter Atlas Based on Diffusion Tensor Imaging in an ICBM Template," Neuroimage, **40**(2), pp. 570–582.

[204] Hua, K., Zhang, J., Wakana, S., Jiang, H., Li, X., Reich, D. S., Calabresi, P. A., Pekar, J. J., van Zijl, P. C. M., and Mori, S., 2008, "Tract Probability Maps in Stereotaxic Spaces: Analyses of White Matter Anatomy and Tract-Specific Quantification," Neuroimage, **39**(1), p. 336.

[205] Jenkinson, M., Bannister, P., Brady, M., and Smith, S., 2002, "Improved

Optimization for the Robust and Accurate Linear Registration and Motion Correction of Brain Images.," Neuroimage, **17**(2), pp. 825–41.

[206] Ji, S., and Margulies, S. S., 2007, "In Vivo Pons Motion within the Skull," J. Biomech., **40**(1), pp. 92–99.

[207] Klatt, D., Johnson, C. L., and Magin, R. L., 2015, "Simultaneous, Multidirectional Acquisition of Displacement Fields in Magnetic Resonance Elastography of the in Vivo Human Brain," J. Magn. Reson. Imaging, **42**(2), pp. 297–304.

[208] Nir, G., Sahebjavaher, R. S., Sinkus, R., and Salcudean, S. E., 2015, "A Framework for Optimization-Based Design of Motion Encoding in Magnetic Resonance Elastography," Magn. Reson. Med., **73**(4), pp. 1514–1525.

[209] Guenthner, C., Runge, J. H., Sinkus, R., and Kozerke, S., 2018, "Analysis and Improvement of Motion Encoding in Magnetic Resonance Elastography," NMR Biomed., **31**(5), p. e3908.

[210] Johnson, C. L., McGarry, M. D. J., Gharibans, A. A., Weaver, J. B., Paulsen, K. D., Wang, H., Olivero, W. C., Sutton, B. P., and Georgiadis, J. G., 2013, "Local Mechanical Properties of White Matter Structures in the Human Brain," Neuroimage, **79**, pp. 145–152.

[211] Guo, J., Hirsch, S., Fehlner, A., Papazoglou, S., Scheel, M., Braun, J., and Sack, I., 2013, "Towards an Elastographic Atlas of Brain Anatomy," PLoS One, **8**(8), p. e71807.

[212] Johnson, C. L., McGarry, M. D. J., Van Houten, E. E. W., Weaver, J. B., Paulsen, K. D., Sutton, B. P., and Georgiadis, J. G., 2013, "Magnetic Resonance Elastography of the Brain Using Multishot Spiral Readouts with Self-Navigated Motion Correction," Magn. Reson. Med., **70**(2), pp. 404–412.

[213] Solamen, L. M., McGarry, M. D., Tan, L., Weaver, J. B., and Paulsen, K. D., 2018, "Phantom Evaluations of Nonlinear Inversion MR Elastography," Phys. Med. Biol., **63**(14), p. 145021.

[214] Testu, J., McGarry, M. D. J., Dittmann, F., Weaver, J. B., Paulsen, K. D., Sack, I., and Van Houten, E. E. W., 2017, "Viscoelastic Power Law Parameters of in Vivo Human Brain Estimated by MR Elastography," J. Mech. Behav. Biomed. Mater., **74**, pp. 333–341.

[215] Yin, Z., Sui, Y., Trzasko, J. D., Rossman, P. J., Manduca, A., Ehman, R. L., and III, J. H., 2018, "In Vivo Characterization of 3D Skull and Brain Motion Using

{MR} Elastography with Multi-Excitation Head Driver," *Proc. Joint Annual Meeting ISMRM-ESMRMB, Paris, France*, 2018 Joint Annual Meeting ISMRM-ESMRMB, Paris, France, p. 1072.

[216] Hiscox, L. V., Schwarb, H., McGarry, M. D. J., and Johnson, C. L., 2021, "Aging Brain Mechanics: Progress and Promise of Magnetic Resonance Elastography," Neuroimage, **232**.

[217] Sack, I., Streitberger, K. J., Krefting, D., Paul, F., and Braun, J., 2011, "The Influence of Physiological Aging and Atrophy on Brain Viscoelastic Properties in Humans," PLoS One, **6**(9), p. e23451.

[218] Babaei, B., Fovargue, D., Lloyd, R. A., Miller, R., Jugé, L., Kaplan, M., Sinkus, R., Nordsletten, D. A., and Bilston, L. E., 2021, "Magnetic Resonance Elastography Reconstruction for Anisotropic Tissues," Med. Image Anal., **74**.

[219] Miller, R., Kolipaka, A., Nash, M. P., and Young, A. A., 2018, "Estimation of Transversely Isotropic Material Properties from Magnetic Resonance Elastography Using the Optimised Virtual Fields Method," Int. j. numer. method. biomed. eng., **34**(6), p. e2979.

[220] Qin, E. C., Sinkus, R., Geng, G., Cheng, S., Green, M., Rae, C. D., and Bilston, L. E., 2013, "Combining MR Elastography and Diffusion Tensor Imaging for the Assessment of Anisotropic Mechanical Properties: A Phantom Study," J. Magn. Reson. Imaging, **37**(1), pp. 217–226.

[221] Smith, D. R., Guertler, C. A., Okamoto, R. J., Romano, A. J., Bayly, P. V., and Johnson, C. L., 2020, "Multi-Excitation Magnetic Resonance Elastography of the Brain: Wave Propagation in Anisotropic White Matter," J. Biomech. Eng., **142**(7), pp. 51–59.

[222] McGarry, M., Houten, E. Van, Guertler, C., Okamoto, R., Smith, D., Sowinski, D., Johnson, C., Bayly, P., Weaver, J., and Paulsen, K., 2021, "A Heterogenous, Time Harmonic, Nearly Incompressible Transverse Isotropic Finite Element Brain Simulation Platform for MR Elastography," Phys. Med. Biol., **66**(5), p. 055029.

[223] McGarry, M. D. J., Van Houten, E. E. W., Sowinski, D., Jyoti, D., Smith, D., Caban-Rivera, D. A., McIlvain, G., Bayly, P., Johnson, C. L., Weaver, J. B., and Paulsen, K., 2021, "Mapping Heterogenous Anisotropic Tissue Mechanical Properties with Transverse Isotropic Nonlinear Inversion MR Elastography.," "In Rev.

[224] Arani, A., Murphy, M. C., Glaser, K. J., Manduca, A., Lake, D. S., Kruse, S.

A., Jack, C. R., Ehman, R. L., and Huston, J., 2015, "Measuring the Effects of Aging and Sex on Regional Brain Stiffness with MR Elastography in Healthy Older Adults," Neuroimage, **111**, pp. 59–64.

[225] Murphy, M. C., Jones, D. T., Jack, C. R., Glaser, K. J., Senjem, M. L., Manduca, A., Felmlee, J. P., Carter, R. E., Ehman, R. L., and Huston, J., 2015, "Regional Brain Stiffness Changes across the Alzheimer's Disease Spectrum," NeuroImage. Clin., **10**, pp. 283–290.

[226] Gerischer, L. M., Fehlner, A., Köbe, T., Prehn, K., Antonenko, D., Grittner, U., Braun, J., Sack, I., and Flöel, A., 2018, "Combining Viscoelasticity, Diffusivity and Volume of the Hippocampus for the Diagnosis of Alzheimer's Disease Based on Magnetic Resonance Imaging," Neuroimage (Amst)., **18**, p. 485.

[227] Huesmann, G. R., Schwarb, H., Smith, D. R., Pohlig, R. T., Anderson, A. T., McGarry, M. D. J., Paulsen, K. D., Wszalek, T. M., Sutton, B. P., and Johnson, C. L., 2020, "Hippocampal Stiffness in Mesial Temporal Lobe Epilepsy Measured with MR Elastography: Preliminary Comparison with Healthy Participants," NeuroImage. Clin., **27**.

[228] Schwarb, H., Johnson, C. L., McGarry, M. D. J., and Cohen, N. J., 2016, "Medial Temporal Lobe Viscoelasticity and Relational Memory Performance," Neuroimage, **132**, pp. 534–541.

[229] Hiscox, L. V., Johnson, C. L., McGarry, M. D. J., Schwarb, H., van Beek, E. J. R., Roberts, N., and Starr, J. M., 2020, "Hippocampal Viscoelasticity and Episodic Memory Performance in Healthy Older Adults Examined with Magnetic Resonance Elastography," Brain Imaging Behav., **14**(1), pp. 175–185.

[230] Caban-Rivera, D. A., Smith, D. R., Okamoto, R. J., McGarry, M. D. J., Williams, L. T., Guertler, C. A., McIlvain, G., Sowinski, D., Van Houten, E. E. W., Paulsen, K. D., Bayly, P. V., and Johnson, C. L., 2021, "Multi-Excitation Actuator Design for Anisotropic Brain MRE," *Internation Society of Magnetic Resonance in Medicine*.

[231] Kailash, K., Rifkin, J., Ireland, J., Okamoto, R., and Bayly, P., 2019, "Design And Evaluation Of A Lateral Head Excitation Device For MR Elastography Of The Brain," *Biomedical Engineering Society Annual Meeting*.

[232] Johnson, C. L., Holtrop, J. L., Anderson, A. T., and Sutton, B. P., 2016, "Brain MR Elastography with Multiband Excitation and Nonlinear Motion-Induced Phase Error Correction," 24th Annu. Meet. Interational Soc. Magn. Reson. Med. Singapore, p. p 1951.

[233] Andersson, J. L. R., Skare, S., and Ashburner, J., 2003, "How to Correct Susceptibility Distortions in Spin-Echo Echo-Planar Images: Application to Diffusion Tensor Imaging," Neuroimage, **20**(2), pp. 870–888.

[234] Leemans, A., and Jones, D. K., 2009, "The B-Matrix Must Be Rotated When Correcting for Subject Motion in DTI Data," Magn. Reson. Med., **61**(6), pp. 1336–1349.

[235] Rouze, N. C., Wang, M. H., Palmeri, M. L., and Nightingale, K. R., 2013, "Finite Element Modeling of Impulsive Excitation and Shear Wave Propagation in an Incompressible, Transversely Isotropic Medium," J. Biomech., **46**(16), pp. 2761–2768.

[236] Brown, C. E., 1998, "Coefficient of Variation," Appl. Multivar. Stat. Geohydrology Relat. Sci., pp. 155–157.

[237] McGarry, M., Van Houten, E., Sowinski, D., Jyoti, D., Smith, D. R., Caban-Rivera, D. A., McIlvain, G., Bayly, P., Johnson, C. L., Weaver, J., and Paulsen, K., 2022, "Mapping Heterogenous Anisotropic Tissue Mechanical Properties with Transverse Isotropic Nonlinear Inversion MR Elastography," Med. Image Anal., **78**, p. 102432.

[238] Budday, S., Sommer, G., Birkl, C., Langkammer, C., Haybaeck, J., Kohnert, J., Bauer, M., Paulsen, F., Steinmann, P., Kuhl, E., and Holzapfel, G. A., 2017, "Mechanical Characterization of Human Brain Tissue," Acta Biomater., **48**, pp. 319–340.

[239] Velardi, F., Fraternali, F., and Angelillo, M., 2006, "Anisotropic Constitutive Equations and Experimental Tensile Behavior of Brain Tissue," Biomech. Model. Mechanobiol., **5**(1), pp. 53–61.

[240] Bayly, P. V., and Garbow, J. R., 2018, "Pre-Clinical MR Elastography: Principles, Techniques, and Applications," J. Magn. Reson., **291**, pp. 73–83.

[241] Aboitiz, F., Scheibel, A. B., Fisher, R. S., and Zaidel, E., 1992, "Individual Differences in Brain Asymmetries and Fiber Composition in the Human Corpus Callosum," Brain Res., **598**(1–2), pp. 154–161.

[242] Aboitiz, F., Rodríguez, E., Olivares, R., and Zaidel, E., 1996, "Age-Related Changes in Fibre Composition of the Human Corpus Callosum: Sex Differences.," Neuroreport, **7**(11), pp. 1761–1764.

[243] Aboitiz, F., and Montiel, J., 2003, "One Hundred Million Years of Interhemispheric Communication: The History of the Corpus Callosum,"

Brazilian J. Med. Biol. Res., **36**(4), pp. 409–420.

[244] Lynn, J. D., Anand, C., Arshad, M., Homayouni, R., Rosenberg, D. R., Ofen, N., Raz, N., and Stanley, J. A., 2021, "Microstructure of Human Corpus Callosum across the Lifespan: Regional Variations in Axon Caliber, Density, and Myelin Content," Cereb. Cortex, **31**(2), pp. 1032–1045.

[245] Paus, T., and Toro, R., 2009, "Could Sex Differences in White Matter Be Explained by g Ratio?," Front. Neuroanat., **3**(SEP), p. 14.

[246] Björnholm, L., Nikkinen, J., Kiviniemi, V., Nordström, T., Niemelä, S., Drakesmith, M., Evans, J. C., Pike, G. B., Veijola, J., and Paus, T., 2017, "Structural Properties of the Human Corpus Callosum: Multimodal Assessment and Sex Differences," Neuroimage, **152**, pp. 108–118.

[247] Flanagan, J. R., Bowman, M. C., and Johansson, R. S., 2006, "Control Strategies in Object Manipulation Tasks," Curr. Opin. Neurobiol., **16**(6), pp. 650–659.

[248] Johansson, R. S., Westling, G., Bäckström, A., and Randall Flanagan, J., 2001, "Eye–Hand Coordination in Object Manipulation," J. Neurosci., **21**(17), pp. 6917–6932.

[249] Hassan H., A., 1989, "Monitoring of Neuromuscular Function," pp. 261–78.

[250] Lake, D. A., 2012, "Neuromuscular Electrical Stimulation," Sport. Med. 1992 135, **13**(5), pp. 320–336.

[251] Roberts, T. J., and Gabaldón, A. M., 2008, "Interpreting Muscle Function from EMG: Lessons Learned from Direct Measurements of Muscle Force.," Integr. Comp. Biol., **48**(2), pp. 312–20.

[252] Nazmi, N., Rahman, M. A. A., Yamamoto, S. I., Ahmad, S. A., Zamzuri, H., and Mazlan, S. A., 2016, "A Review of Classification Techniques of EMG Signals during Isotonic and Isometric Contractions," Sensors (Basel)., **16**(8).

[253] Buchanan, T. S., Lloyd, D. G., Manal, K., and Besier, T. F., 2004, "Neuromusculoskeletal Modeling: Estimation of Muscle Forces and Joint Moments and Movements from Measurements of Neural Command.," J. Appl. Biomech., **20**(4), pp. 367–95.

[254] Rouffet, D. M., and Hautier, C. A., 2008, "EMG Normalization to Study Muscle Activation in Cycling," J. Electromyogr. Kinesiol., **18**(5), pp. 866–878.

[255] Geiger, D. E., Behrendt, F., and Schuster-Amft, C., 2019, "EMG Muscle Activation Pattern of Four Lower Extremity Muscles during Stair Climbing, Motor Imagery, and Robot-Assisted Stepping: A Cross-Sectional Study in Healthy Individuals," Biomed Res. Int., **2019**, pp. 1–8.

[256] Dieterich, A. V., Botter, A., Vieira, T. M., Peolsson, A., Petzke, F., Davey, P., and Falla, D., 2017, "Spatial Variation and Inconsistency between Estimates of Onset of Muscle Activation from EMG and Ultrasound," Sci. Rep., **7**(1), p. 42011.

[257] Ngeo, J. G., Tamei, T., and Shibata, T., 2014, "Continuous and Simultaneous Estimation of Finger Kinematics Using Inputs from an EMG-to-Muscle Activation Model," J. Neuroeng. Rehabil., **11**(1), p. 122.

[258] Vieira, T. M., Baudry, S., and Botter, A., 2016, "Young, Healthy Subjects Can Reduce the Activity of Calf Muscles When Provided with EMG Biofeedback in Upright Stance," Front. Physiol., **7**(APR), p. 158.

[259] Vieira, T. M., Botter, A., Muceli, S., and Farina, D., 2017, "Specificity of Surface EMG Recordings for Gastrocnemius during Upright Standing," Sci. Reports 2017 71, **7**(1), pp. 1–11.

[260] Eby, S., Zhao, H., Song, P., Vareberg, B. J., Kinnick, R., Greenleaf, J. F., An, K. N., Chen, S., and Brown, A. W., 2016, "Quantitative Evaluation of Passive Muscle Stiffness in Chronic Stroke," Am. J. Phys. Med. Rehabil., **95**(12), p. 899.

[261] Brandenburg, J. E., Eby, S. F., Song, P., Kingsley-Berg, S., Bamlet, W., Sieck, G. C., and An, K. N., 2016, "Quantifying Passive Muscle Stiffness in Children with and without Cerebral Palsy Using Ultrasound Shear Wave Elastography," Dev. Med. Child Neurol., **58**(12), pp. 1288–1294.

[262] Guertler, C. A., Okamoto, R. J., Schmidt, J. L., Badachhape, A. A., Johnson, C. L., and Bayly, P. V, 2018, "Mechanical Properties of Porcine Brain Tissue in Vivo and Ex Vivo Estimated by MR Elastography," J. Biomech., **69**, pp. 10–18.

[263] Schrank, F., Warmuth, C., Görner, S., Meyer, T., Tzschätzsch, H., Guo, J., Uca, Y. O., Elgeti, T., Braun, J., and Sack, I., 2020, "Real-Time MR Elastography for Viscoelasticity Quantification in Skeletal Muscle during Dynamic Exercises," Magn. Reson. Med., **84**(1), pp. 103–114.

[264] Debernard, L., Robert, L., Charleux, F., and Bensamoun, S. F., 2011, "Characterization of Muscle Architecture in Children and Adults Using Magnetic Resonance Elastography and Ultrasound Techniques," J. Biomech.,

44(3), pp. 397–401.

[265] Zonnino, A., Smith, D. R., Delgorio, P. L., Johnson, C. L., and Sergi, F., 2019, "MM-MRE: A New Technique to Quantify Individual Muscle Forces during Isometric Tasks of the Wrist Using MR Elastography," IEEE Int. Conf. Rehabil. Robot., **2019-June**, pp. 270–275.

[266] Bernabei, M., lee, S. S. M., Perreault, E. J., and Sandercock, T. G., 2019, "Shear Wave Velocity Is Sensitive to Changes in Muscle Stiffness That Occur Independently from Changes in Force," J. Appl. Physiol.

[267] Raiteri, B. J., Hug, F., Cresswell, A. G., and Lichtwark, G. A., 2016, "Quantification of Muscle Co-Contraction Using Supersonic Shear Wave Imaging," J. Biomech., **49**(3), pp. 493–495.

[268] Huxley, A. F., and Simmons, R. M., 1971, "Proposed Mechanism of Force Generation in Striated Muscle," Nat. 1971 2335321, **233**(5321), pp. 533–538.

[269] Hirokawa, S., Solomonow, M., Luo, Z., Lu, Y., and D'Ambrosia, R., 1991, "Muscular Co-Contraction and Control of Knee Stability," J. Electromyogr. Kinesiol., **1**(3), pp. 199–208.

[270] Viitasalo, J. T., 1982, "Effects of Pretension on Isometric Force Production," Int. J. Sports Med., **3**(3), pp. 149–152.

[271] McGarry, M. D. J., Van Houten, E. E. W., Perriñez, P. R., Pattison, A. J., Weaver, J. B., and Paulsen, K. D., 2011, "An Octahedral Shear Strain-Based Measure of SNR for 3D MR Elastography.," Phys. Med. Biol., **56**(13), pp. N153-64.

[272] Johnson, C. L., Holtrop, J. L., McGarry, M. D. J., Weaver, J. B., Paulsen, K. D., Georgiadis, J. G., and Sutton, B. P., 2014, "3D Multislab, Multishot Acquisition for Fast, Whole-Brain MR Elastography with High Signal-to-Noise Efficiency," Magn. Reson. Med., **71**(2), pp. 477–485.

[273] Ranatunga, K. W., 2011, "Skeletal Muscle Stiffness and Contracture in Children with Spastic Cerebral Palsy," J. Physiol., **589**(Pt 11), p. 2665.

[274] Mathewson, M. A., and Lieber, R. L., 2015, "Pathophysiology of Muscle Contractures in Cerebral Palsy," Phys. Med. Rehabil. Clin. N. Am., **26**(1), pp. 57–67.

[275] Mills, K. R., 2005, "The Basics of Electromyography.," J. Neurol. Neurosurg. Psychiatry, **76 Suppl 2**(suppl 2), pp. ii32-5.

[276] Taljanovic, M. S., Gimber, L. H., Becker, G. W., Latt, L. D., Klauser, A. S., Melville, D. M., Gao, L., and Witte, R. S., 2017, "Shear-Wave Elastography: Basic Physics and Musculoskeletal Applications," Radiographics, **37**(3), pp. 855–870.

[277] Barnhill, E., Kennedy, P., Hammer, S., Van Beek, E. J. R., Brown, C., and Roberts, N., 2013, "Statistical Mapping of the Effect of Knee Extension on Thigh Muscle Viscoelastic Properties Using Magnetic Resonance Elastography," Physiol. Meas., **34**(12), pp. 1675–1698.

[278] Kennedy, P., Barnhill, E., Gray, C., Brown, C., van Beek, E. J. R., Roberts, N., and Greig, C. A., 2020, "Magnetic Resonance Elastography (MRE) Shows Significant Reduction of Thigh Muscle Stiffness in Healthy Older Adults," GeroScience, **42**(1), pp. 311–321.

[279] Green, M. A., Sinkus, R., Gandevia, S. C., Herbert, R. D., and Bilston, L. E., 2012, "Measuring Changes in Muscle Stiffness after Eccentric Exercise Using Elastography," NMR Biomed., **25**(6), pp. 852–858.

[280] Kennedy, P., Macgregor, L. J., Barnhill, E., Johnson, C. L., Perrins, M., Hunter, A., Brown, C., van Beek, E. J. R., and Roberts, N., 2017, "MR Elastography Measurement of the Effect of Passive Warmup Prior to Eccentric Exercise on Thigh Muscle Mechanical Properties," J. Magn. Reson. Imaging, **46**(4), pp. 1115–1127.

[281] Basford, J. R., Jenkyn, T. R., An, K.-N. N., Ehman, R. L., Heers, G., and Kaufman, K. R., 2002, "Evaluation of Healthy and Diseased Muscle with Magnetic Resonance Elastography," Arch. Phys. Med. Rehabil., **83**(11), pp. 1530–1536.

[282] Ringleb, S. I., Bensamoun, S. F., Chen, Q., Manduca, A., An, K.-N., and Ehman, R. L., 2007, "Applications of Magnetic Resonance Elastography to Healthy and Pathologic Skeletal Muscle.," J. Magn. Reson. Imaging, **25**(2), pp. 301–9.

[283] Jenkinson, M., 2003, "Fast, Automated, N-Dimensional Phase-Unwrapping Algorithm," Magn. Reson. Med., **49**(1), pp. 193–197.

[284] Abiza, Z., Destrade, M., and Ogden, R. W., 2012, "Large Acoustoelastic Effect," Wave Motion, **49**(2), pp. 364–374.

[285] Maganaris, C. N., 2003, "Force-Length Characteristics of the in Vivo Human Gastrocnemius Muscle," Clin. Anat., **16**(3), pp. 215–223.

[286] Riemann, B. L., DeMont, R. G., Ryu, K., and Lephart, S. M., 2001, "The Effects of Sex, Joint Angle, and the Gastrocnemius Muscle on Passive Ankle Joint Complex Stiffness," J. Athl. Train., **36**(4), p. 369.

[287] Stecco, C., Pirri, C., Fede, C., Yucesoy, C. A., De Caro, R., and Stecco, A., 2021, "Fascial or Muscle Stretching? A Narrative Review," Appl. Sci., **11**(1), pp. 1–11.

[288] Takaza, M., Moerman, K. M., Gindre, J., Lyons, G., and Simms, C. K., 2013, "The Anisotropic Mechanical Behaviour of Passive Skeletal Muscle Tissue Subjected to Large Tensile Strain," J. Mech. Behav. Biomed. Mater., **17**, pp. 209–220.

[289] Pietsch, R., Wheatley, B. B., Donahue, T. L. H., Gilbrech, R., Prabhu, R., Liao, J., and Williams, L. N., 2014, "Anisotropic Compressive Properties of Passive Porcine Muscle Tissue," J. Biomech. Eng., **136**(11).

[290] Fitts, R. H., 2008, "The Cross-Bridge Cycle and Skeletal Muscle Fatigue," J. Appl. Physiol., **104**(2), pp. 551–558.

[291] McLester, J. R., 2012, "Muscle Contraction and Fatigue," Sport. Med., **23**(5), pp. 287–305.

Appendix A

IRB/HUMAN SUBJECTS APPROVAL

Institutional Review Board
210H Hullihen Hall
Newark, DE 19716
Phone: 302-831-2137
Fax: 302-831-2828

DATE:	June 28, 2021
TO:	Curtis Johnson, PhD
FROM:	University of Delaware IRB
STUDY TITLE:	[932679-10] High-resolution, anisotropic MR elastography of the brain
SUBMISSION TYPE:	Continuing Review/Progress Report
ACTION:	APPROVED
APPROVAL DATE:	June 28, 2021
EXPIRATION DATE:	July 20, 2022
REVIEW TYPE:	Expedited Review
REVIEW CATEGORY:	Expedited review category # *(9)*

Thank you for your Continuing Review/Progress Report submission to the University of Delaware Institutional Review Board (UD IRB). The UD IRB has reviewed and APPROVED the proposed research and submitted documents via Expedited Review in compliance with the pertinent federal regulations.

As the Principal Investigator for this study, you are responsible for and agree that:

- All research must be conducted in accordance with the protocol and all other study forms as approved in this submission. Any revisions to the approved study procedures or documents must be reviewed and approved by the IRB prior to their implementation. Please use the UD amendment form to request the review of any changes to approved study procedures or documents.
- Informed consent is a process that must allow prospective participants sufficient opportunity to discuss and consider whether to participate. IRB-approved and stamped consent documents must be used when enrolling participants and a written copy shall be given to the person signing the informed consent form.
- Unanticipated problems, serious adverse events involving risk to participants, and all non-compliance issues must be reported to this office in a timely fashion according with the UD requirements for reportable events. All sponsor reporting requirements must also be followed.

Oversight of this study by the UD IRB REQUIRES the submission of a CONTINUING REVIEW seeking the renewal of this IRB approval, which will expire on July 20, 2022. A continuing review/progress report form and up-to-date copies of the protocol form and all other approved study materials must be submitted to the UD IRB at least 45 days prior to the expiration date to allow for the required IRB review of that report.

If you have any questions, please contact the UD IRB Office at (302) 831-2137 or via email at hsrb-research@udel.edu. Please include the study title and reference number in all correspondence with this office.

Institutional Review Board
210H Hullihen Hall
Newark, DE 19716
Phone: 302-831-2137
Fax: 302-831-2828

DATE:	June 21, 2021
TO:	Curtis Johnson, PhD
FROM:	University of Delaware IRB
STUDY TITLE:	[1465242-5] Multi-Muscle Magnetic Resonance Elastography (MM-MRE): a new technique to measure non-invasively individual force of forearm muscles during fine motor tasks
SUBMISSION TYPE:	Continuing Review/Progress Report
ACTION:	APPROVED
APPROVAL DATE:	June 21, 2021
EXPIRATION DATE:	July 16, 2022
REVIEW TYPE:	Expedited Review
REVIEW CATEGORY:	Expedited review category # *(9)*

Thank you for your Continuing Review/Progress Report submission to the University of Delaware Institutional Review Board (UD IRB). The UD IRB has reviewed and APPROVED the proposed research and submitted documents via Expedited Review in compliance with the pertinent federal regulations.

As the Principal Investigator for this study, you are responsible for and agree that:

- All research must be conducted in accordance with the protocol and all other study forms as approved in this submission. Any revisions to the approved study procedures or documents must be reviewed and approved by the IRB prior to their implementation. Please use the UD amendment form to request the review of any changes to approved study procedures or documents.
- Informed consent is a process that must allow prospective participants sufficient opportunity to discuss and consider whether to participate. IRB-approved and stamped consent documents must be used when enrolling participants and a written copy shall be given to the person signing the informed consent form.
- Unanticipated problems, serious adverse events involving risk to participants, and all non-compliance issues must be reported to this office in a timely fashion according with the UD requirements for reportable events. All sponsor reporting requirements must also be followed.

Oversight of this study by the UD IRB REQUIRES the submission of a CONTINUING REVIEW seeking the renewal of this IRB approval, which will expire on July 16, 2022. A continuing review/progress report form and up-to-date copies of the protocol form and all other approved study materials must be submitted to the UD IRB at least 45 days prior to the expiration date to allow for the required IRB review of that report.

If you have any questions, please contact the UD IRB Office at (302) 831-2137 or via email at hsrb-research@udel.edu. Please include the study title and reference number in all correspondence with this office.

Institutional Review Board
210H Hullihen Hall
Newark, DE 19716
Phone: 302-831-2137
Fax: 302-831-2828

DATE:	April 26, 2021
TO:	Curtis Johnson, PhD
FROM:	University of Delaware IRB
STUDY TITLE:	[1730839-1] Contractile Anisotropy of Leg Function
SUBMISSION TYPE:	New Project
ACTION:	APPROVED
APPROVAL DATE:	April 26, 2021
EXPIRATION DATE:	April 25, 2022
REVIEW TYPE:	Full Committee Review

Thank you for your New Project submission to the University of Delaware Institutional Review Board (UD IRB). The UD IRB has reviewed and APPROVED the proposed research and submitted documents via Full Committee Review in compliance with the pertinent federal regulations.

As the Principal Investigator for this study, you are responsible for and agree that:

- All research must be conducted in accordance with the protocol and all other study forms as approved in this submission. Any revisions to the approved study procedures or documents must be reviewed and approved by the IRB prior to their implementation. Please use the UD amendment form to request the review of any changes to approved study procedures or documents.
- Informed consent is a process that must allow prospective participants sufficient opportunity to discuss and consider whether to participate. IRB-approved and stamped consent documents must be used when enrolling participants and a written copy shall be given to the person signing the informed consent form.
- Unanticipated problems, serious adverse events involving risk to participants, and all non-compliance issues must be reported to this office in a timely fashion according with the UD requirements for reportable events. All sponsor reporting requirements must also be followed.

Oversight of this study by the UD IRB REQUIRES the submission of a CONTINUING REVIEW seeking the renewal of this IRB approval, which will expire on April 25, 2022. A continuing review/progress report form and up-to-date copies of the protocol form and all other approved study materials must be submitted to the UD IRB at least 45 days prior to the expiration date to allow for the required IRB review of that report.

If you have any questions, please contact the UD IRB Office at (302) 831-2137 or via email at hsrb-research@udel.edu. Please include the study title and reference number in all correspondence with this office.

Appendix B

PERMISSIONS

https://www.asme.org/publications-submissions/journals/information-for-authors/journal-guidelines/copyright-transfer